

**Czech Technical University in Prague  
České vysoké učení technické v Praze**

Faculty of Civil Engineering  
Department of Hydraulics and Hydrology



**Mathematical Modelling of Solid-Liquid Flow in Open Channel**

by

Joaquín Rodrigo Llanos Espinoza

A thesis submitted to  
The Faculty of Civil Engineering,  
Czech Technical University in Prague

Master's degree study programme: Water and Environmental Engineering

Specialization: Environmental Engineering and Science

Thesis Supervisor: Dr. Ing. Václav Matoušek

Prague, May 2024



# MASTER'S THESIS ASSIGNMENT

## I. Personal and study details

Student's name: **Llanos Espinoza Joaquin** Personal ID number: **518102**  
Faculty / Institute: **Faculty of Civil Engineering**  
Department / Institute: **Department of Hydraulics and Hydrology**  
Study program: **Water and Environmental Engineering**  
Specialisation: **Environmental Engineering and Science**

## II. Master's thesis details

Master's thesis title in English:

Master's thesis title in Czech:

**Mathematical Modelling of Solid-Liquid Flow in Open Channel**

Guidelines:

The work evaluates suitable approaches to mathematical modeling of solid-liquid flow in an open channel. The considered flow is turbulent, steady-state, and uniform. Unimodal and bimodal solids fractions are considered, and they are transported at relatively high concentrations. Two options are considered for the channel bottom – the fixed bottom and the mobile bed composed of the same solid particles as those transported above the bed.

The main aim is to find an optimum approach to modeling the internal structure of the solid-liquid flow (the distributions of solids concentration and velocities of solids and liquid) and to predict mutual relationships among the solids discharge, liquid discharge, flow depth, and bottom longitudinal slope.

Bibliography / sources:

DEY, S.: Fluvial Hydrodynamics. Hydrodynamic and Sediment Transport Phenomena. Springer. 2014. ISBN 978-3-642-19061-2

GARCIA, M. H. (ed.): Sedimentation Engineering. Processes, Measurements, Modeling, and Practice. ASCE Manuals and Reports on Engineering Practice No. 110. 2009. ISBN 978-0-7844-0814-8

Software manuals and documentation: Matlab, Ansys

Name and workplace of master's thesis supervisor:

**prof. Dr. Ing. Václav Matoušek Department of Hydraulics and Hydrology FCE**

Name and workplace of second master's thesis supervisor or consultant:

Date of master's thesis assignment: **20.02.2024** Deadline for master's thesis submission: **20.05.2024**

Assignment valid until: \_\_\_\_\_

prof. Dr. Ing. Václav Matoušek  
Supervisor's signature

prof. Ing. Tomáš Vogel, CSc.  
Head of department's signature

prof. Ing. Jiří Máca, CSc.  
Dean's signature

## III. Assignment receipt

The student acknowledges that the master's thesis is an individual work. The student must produce his thesis without the assistance of others, with the exception of provided consultations. Within the master's thesis, the author must state the names of consultants and include a list of references.

\_\_\_\_\_  
Date of assignment receipt

\_\_\_\_\_  
Student's signature

**CZECH TECHNICAL UNIVERSITY IN PRAGUE**  
Faculty of Civil Engineering  
Thákurova 2077/7, 166 29 Praha 6

## **DECLARATION**

I, the undersigned

Surname and name of the student: Llanos Espinoza, Joaquín Rodrigo

Personal no.: 518102

Study programme: N0732A260028 - Water and Environmental Engineering

hereby declare that the Master's Thesis titled

### **Mathematical Modelling of Solid-Liquid Flow in Open Channel**

is my own independent work and that I have declared all sources of information used in accordance with the Methodological Guideline for adhering to ethical principles when elaborating an academic final thesis and the Framework Rules for the use of artificial intelligence at CTU for study and pedagogical purposes in Bachelor and continuing Masters studies.

In Prague on 20<sup>th</sup> of May of 2024

  
.....  
Signature

## I. Acknowledgments

---

The research presented in this thesis was supported by the Czech Science Foundation, grant project number 23-07772S.

I would like to express my gratitude to Dr. Ing. Václav Matoušek, not only for being one of the best teachers I have ever had, but also for his kindness and support during my time as an international student.

I am profoundly grateful to my mother, whose support from afar has been the foundation of my academic journey. This achievement would not have been possible without her encouragement and belief in me.

Lastly, I wish to thank my husband for standing by my side throughout this process. No academic accomplishment could ever compare to the joy and fulfilment of having found him in the Czech Republic.

## II. Abstract

---

### A. English

This thesis investigates the complex multiphase flow of mixture of liquid and granular solids in open channels using advanced numerical modelling techniques within Ansys Fluent. By employing a Eulerian-Eulerian approach, the study provides a detailed exploration of flow behaviours across various conditions, focusing on unimodal and bimodal distributions of particle sizes. The simulation work evaluates the dynamics of solids transport under different flow scenarios, highlighting the effects of particle size variation and the interaction between solid particles and the carrying fluid. The simulations demonstrate a clear stratification process, especially in bimodal particle distributions. Coarser particles predominantly settle closer to the channel bed, whereas finer particles are more suspended within the flow. This stratification is more pronounced under certain flow conditions and adjusts with changes in particle size distribution, flow velocity, and channel slope. Increased discharge generally results in higher flow velocities and greater flow depths. This condition also affects stratification by promoting more vigorous mixing of particles and reducing the distinct layers of particle sizes. Higher discharges lead to increased turbulence within the flow, which can disrupt the settling of particles and lead to a more homogeneous mixture throughout the flow depth. The findings from this research contribute significantly to environmental engineering by offering enhanced predictive capabilities for particle transport in water bodies. Such insights are crucial for effective sediment management, erosion control, and the maintenance of hydraulic infrastructure. Furthermore, the validated models extend their utility to the optimization of channel design, supporting sustainable water resource management practices.

### B. Czech

Tato práce se zabývá numerickým modelováním proudění směsi vody a pevných částic s volnou hladinou pomocí softwaru ANSYS Fluent. Za použití přístupu Euler-Euler je simulováno chování proudění za různých podmínek včetně vlivu zrnitosti částic v podobě stejnozrného a bimodálního charakteru transportovaných částic. Práce se soustřeďuje na vyhodnocení dynamiky transportu částic v závislosti na podmínkách proudění a procesu stratifikace fází, ke kterému při proudění dochází. V případě proudění bimodální směsi simulace ukazují, že hrubozrnější frakce vykazuje větší míru stratifikace a akumulace částic u dna koryta než jemnozrnější frakce, jejíž částice jsou více suspendovány v proudící nosné kapalině. Je ukázáno, že míra stratifikace se mění nejen se zrností, ale také s rychlostí proudění a sklonem koryta. Simulace ukazují jak se se zvyšujícím se průtokem zvyšuje hloubka a rychlost proudění směsi, přičemž se mění i míra stratifikace proudění. Vyšší intenzita turbulence rychleji proudící vody omezuje schopnost částic se usazovat a vede k homogenějšímu rozložení nesených částic v proudu. Získané výsledky simulací pomáhají lépe pochopit zákonitosti transportu částic v proudící vodě s přímými dopady na vodohospodářskou a environmentální praxi například v podobě efektivnějšího managementu říčních sedimentů a provozu vodohospodářské infrastruktury. Validované simulační modely mohou být také využity při optimalizaci návrhu kanálů a koryt a přispět tím k udržitelnému provozu a rozvoji prvků vodního hospodářství.

Keywords: Multiphase flow, Particle transport, Computational fluid dynamics, Open channel flow

### III. Contents

---

|       |   |     |
|-------|---|-----|
| I.    | Acknowledgments .....                             | 3   |
| II.   | Abstract .....                                    | 4   |
| III.  | Contents .....                                    | 5   |
| 1.    | Introduction .....                                | 6   |
| 1.1   | Objectives .....                                  | 7   |
| 1.1.1 | Primary Objectives .....                          | 7   |
| 1.1.2 | Secondary Objectives .....                        | 7   |
| 2.    | Theoretical Framework.....                        | 8   |
| 2.1   | State of the Art .....                            | 8   |
| 2.2   | Multiphase Flows .....                            | 8   |
| 2.2.2 | The Eulerian Model.....                           | 11  |
| 2.3   | Turbulence Modelling .....                        | 21  |
| 2.4   | Numerical Solver Aspects.....                     | 27  |
| 2.5   | Meshing Considerations .....                      | 29  |
| 2.6   | Other Equations Used .....                        | 29  |
| 3.    | Methodology .....                                 | 31  |
| 3.1   | Conditions and Assumptions for Modelled Flow..... | 31  |
| 3.2   | Introduction to Ansys Software .....              | 32  |
| 3.3   | Platform Software: Ansys Workbench.....           | 33  |
| 3.4   | Pre-Processing Software.....                      | 36  |
| 3.4.1 | Ansys SpaceClaim Geometry.....                    | 36  |
| 3.4.2 | Ansys Meshing .....                               | 39  |
| 3.5   | Calculation Software: Ansys Fluent .....          | 43  |
| 3.5.1 | Fluent Launcher and Initial Interface .....       | 43  |
| 3.5.2 | General Configuration .....                       | 45  |
| 3.5.3 | Materials Configuration .....                     | 45  |
| 3.5.4 | Model Configuration.....                          | 46  |
| 3.5.5 | Boundary Conditions Configuration .....           | 49  |
| 3.5.6 | Numerical Solver Configuration .....              | 52  |
| 3.6   | Post-processing Software: Ansys CFD-Post .....    | 58  |
| 4.    | Results and Discussion .....                      | 62  |
| 4.1   | Water-only Flow .....                             | 63  |
| 4.2   | Unimodal Flow.....                                | 66  |
| 4.3   | Bimodal Flow .....                                | 72  |
| 5.    | Conclusions .....                                 | 98  |
| 6.    | Bibliography .....                                | 100 |
| 7.    | Appendix A .....                                  | 103 |

# 1. Introduction

---

The transport of particles within open channel flows presents a complex multiphase phenomenon with significant implications across various engineering applications. This thesis investigates this phenomenon through numerical modelling using Ansys, a computational fluid dynamics (CFD) software suite. The Eulerian-Eulerian multiphase modelling approach is employed to simulate the interaction between three or four distinct phases: air, water, and solid particles.

The main motivation for this study stems from the research work being conducted at the hydraulics laboratory of the Czech Technical University in Prague. There, experiments have explored stereoscopic methods for measuring particle velocities in laboratory flumes. While promising, these methods often rely on identifying particles based on a single characteristic, like colour. However, real-world scenarios may involve particles with similar colours or complex shapes, limiting the applicability of such techniques [1].

This research focuses on two primary categories of open channel flows with particle transport, aiming to replicate realistic flow conditions: unimodal and bimodal flows. Unimodal flows represent scenarios where only one type of solid particle, all with the same diameter, is present in the flow. Bimodal flows, on the other hand, involve the interaction of two distinct solid phases, each characterized by a different particle diameter. The simulations will model the flow as a system of solid particles and liquid (water) with a free surface in contact with a gaseous phase, mimicking the air-water interface present in real-world open channels. The geometry of the channel will be designed to replicate the specific conditions found in the laboratory flume experiments, ensuring that a steady flow is achieved within a prismatic channel.

Furthermore, the model will account for the complex interactions between particle collisions and the influence of turbulence on particle movement, which will allow us to capture how these factors combine to influence particle behaviour within the flow. Additionally, the flow will be modelled as turbulent making use of the SST  $k - \omega$  model, accounting for the eddies and fluctuations that are usually key factors influencing the particle transport mechanisms [1].

The simulations will also consider the potential for particle layering within the flow, mainly due to the solid phase particle size distinctness, but also considering a small density difference. This will involve investigating the possibility of stratified flow, where particles of different sizes and/or densities separate and form distinct layers within the flow. By incorporating these various flow characteristics, the research aims to achieve a more comprehensive understanding of particle transport in open channels compared to experimental techniques with limitations in identifying complex particle properties. This numerical modelling approach offers a complementary method for investigating particle behaviour, particularly in scenarios where the use of traditional measurement methods might be challenging.

## 1.1 Objectives

### 1.1.1 Primary Objectives

- To evaluate the effectiveness of the Eulerian-Eulerian multiphase model in Ansys Fluent for simulating open channel flows with particle transport.
- To investigate the influence of particle characteristics, specifically size distribution (unimodal vs. bimodal), on flow dynamics within open channels.

### 1.1.2 Secondary Objectives

- To assess the computational efficiency of the Eulerian-Eulerian model for different flow scenarios (unimodal vs. bimodal).
- To provide valuable data and insights for the development and validation of improved multiphase flow models for open channel simulations.
- To contribute to a deeper understanding of three-phase flow with a solid granular phase, facilitating the development of more accurate and efficient simulation for engineering applications.



## 2. Theoretical Framework

---

### 2.1 State of the Art

Particle segregation within open channel flows has attracted some research attention due to its impact on sediment transport, debris movement, and slurry flow behaviour. Studies exploring this phenomenon often employ various modelling approaches to capture the interactions between particles and the surrounding fluid.

One such study by M. Larcher and J.T. Jenkins [2] investigated the segregation of spheres with different sizes or densities in open channel flows. Their work, based on kinetic theory formulations alongside fundamental conservation equations observed significant deviations in flow features (velocity, granular temperature, and solid concentration profiles) compared to flows with a single, average-sized particle.

While open channel flows present unique challenges, research on slurry transport in pressurized pipes using Computational Fluid Dynamics (CFD) software like Ansys Fluent has also been studied. Li et al [3] employed Ansys Fluent to explore the impact of adding large particles on slurry flow characteristics in horizontal pipes, which led to simulations that compared slurries with a uniform particle size to those with a mixture of different sized particles. The addition of large particles was found to influence the flow in several ways, including increased granular pressure, decreased turbulent kinetic energy of small particles, and reduced wall shear force and total pipe resistance under specific flow conditions. These findings suggest that the strategic use of particle size distribution can potentially improve flow efficiency and reduce energy consumption in pressurized pipe systems.

Further advancements in modelling multi-sized slurry flows were also achieved by Li et al [4]. Their work developed a 3D multiphase model within Ansys Fluent to investigate the behaviour of slurries containing two distinct particle sizes flowing within pipelines. The model successfully captured the distinct behaviour of coarse and fine particles under different flow velocities and solid concentrations; thus, the authors emphasize the importance of considering particle size disparities when modelling multi-sized slurry flows using CFD software.

### 2.2 Multiphase Flows

#### A. General Concepts

Open-channel granular flows are multiphase flows where air, water and sediment particles interact within a gravitational field. These complex flows involve the dynamic interplay between all three phases, with each influencing the behaviour of the others. These flows play a crucial role in shaping landscapes, transporting pollutants, and influencing ecological systems, becoming increasingly interesting for scientists and engineers. Accurately modelling such multiphase flows is essential for understanding their behaviour and predicting their impact, thus, the focus lies on capturing the interactions and complexities that arise from the coexistence of these phases within the flow. This kind of flows consist of three distinct phases: atmospheric air (gaseous), water (liquid), and solid spherical particles of varying sizes and compositions (solid).

To achieve an accurate and computationally efficient model, a key initial step involves identifying the flow's characteristics. Classifying the multiphase nature of the flow helps us determine appropriate simplifications while maintaining model fidelity by selecting appropriate sub-models, all in order to calculate or estimate the different variables involved in the mathematical description of the flow.

## **B. Gas-Solid Flows**

Imagine solid particles suspended within a flowing gas. In dilute flows, with a low number of solid particles, the gas phase commands the flow, and particle interactions are negligible. Very dilute flows push this further, with particles acting like mere tracers within the gas. However, when the particle presence increases significantly, particle-to-particle interactions become relevant forces, dictating their movement, and affecting the gaseous phase behaviour. This dense flow regime is known as gaseous granular flow. Additionally, the way particles interact with walls differs from their free flight behaviour due to the influence of surface characteristics and material properties. In gas-solid flows, the solid particles represent the dispersed or secondary phase, while the gas acts as the continuous or primary phase.

## **C. Liquid-Solid Flows (Slurry Flows)**

In liquid-solid or slurry flows, we encounter the transport of solid particles within a liquid medium, where pressure gradients play a crucial role in driving the flow, as the density difference between the phases can be considered small (they differ in less than one order of magnitude). Solid particles, once again, constitute the dispersed phase, while the liquid acts as the continuous phase. On the other hand, drag between the solid particles and the liquid is a crucial force that usually dictates, or at least influences, the behaviour of the flow [5], thus, it must be carefully included in the model. Modelling these flows gets even more interesting when dealing with solid particles of varying sizes, because even though the particles are made of the same material, their size difference necessitates treating them as separate phases. This is because each size class exhibits distinct dynamic responses within the flow environment.

## **D. Gas-Liquid Flows**

Gas-liquid flows present a diverse spectrum of scenarios, and their existence is quite common in natural environments. A usual situation would be gas bubbles dispersed within a liquid phase, or conversely, liquid droplets suspended in a gas stream. Depending on the dominant phase, the categorization changes, and subsequently does the modelling approach and simplifications. When gas bubbles reside in a liquid, the liquid becomes the continuous phase, and the gas bubbles take on the role of the dispersed phase. An example of this would be a highly aerated water flow, like the one occurring in natural river rapids. Similarly, for liquid droplets in a gas stream, the gas acts as the continuous phase, and the liquid droplets become the dispersed phase. Interestingly, gas bubbles and liquid droplets can deform within the continuous phase, assuming various shapes ranging from spherical to complex configurations. Gas-liquid flows exhibit transitions between different flow regimes due to interactions between bubbles (coalescence and breakup) and phase changes between gas and liquid [6]. In a special case of separated flows, such as a liquid film within a gas phase, distinct interfaces exist between the phases. These are classified as immiscible flows, and each phase is treated as a continuous fluid flowing concurrently with the other [5].

## **E. Three-Phase Flow**

Engineering applications often encounter complex flows where gas bubbles and solid particles coexist within a liquid (three-phase flows). Modelling these flows computationally becomes significantly more challenging and demanding. The primary reason lies in the need to account for a multitude of interactions between the different phases. These interactions include particle-particle collisions, bubble-bubble collisions, particle-bubble interactions, as well as the influence of both particles and bubbles on the surrounding liquid. All these interactions collectively influence the overall behaviour of the multiphase flow, making it a complex task to accurately capture in computer simulations. Nevertheless, it is possible to generate a model

that can be executed on user-level modern computers using industry-oriented software, like Ansys o StarCCM+, at least in a two-dimensional simplified, yet representative domain.

## **F. Approaches to Multiphase Modelling**

To study the dynamics of multiphase flows, specifically the ones carrying solid particles, two approaches for numerically calculated outcomes exist: The Euler-Euler approach, and the Euler-Lagrange approach.

### *Euler-Euler Approach*

The Euler-Euler approach treats multiphase flows by representing each phase as a continuum characterized by its average density, velocity, and other relevant properties within a small control volume. This can be visualized by discretizing the flow domain into a mesh of infinitesimal cells, typically cubes or squares depending on the dimensionality of the model. The Euler-Euler methodology then solves for the ensemble-averaged properties of each phase within each control volume. To initiate the solution process, appropriate boundary conditions are required for the elements intersecting the system's boundaries. These conditions can involve specifying the volume fraction of each phase at the boundaries [7].

Three different models exist within the Euler-Euler approach framework in Ansys Fluent, which is the software used in this project: The Volume of Fluid (VOF), the Mixture Model and the Eulerian Model.

The Volume of Fluid (VOF) model is capable of representing two or more immiscible fluids within a single framework by solving a unified set of momentum equations while monitoring the volume fraction of each fluid across the entire computational domain. Its common applications include predicting phenomena like jet fragmentation, post-dam break liquid dynamics, as well as the continuous monitoring, either steady or transient, of any interface between liquid and gas phases [8]. The method is primarily designed to handle multiphase flows involving distinct fluid phases with clear interfaces, such as liquid-liquid or gas-liquid systems [9]. While it is highly effective for simulating free-surface flows, interface dynamics, and phase separation, it is not well-suited for flows carrying granular materials since it is not compatible with variables related to particle-particle interactions.

The Mixture model offers a simplified approach to multiphase modelling, adaptable to various scenarios since it solves multiphase flows where phases exhibit different velocities yet maintain local equilibrium across short spatial scales [9]. Alternatively, it can simulate homogeneous multiphase flows with high degree of coupling, where phases move at identical speeds, and additionally, mixture models are adept at handling non-Newtonian viscosity calculations [9]. The phases involved when using this model, whether fluid or particulate, are represented by solving momentum, continuity, and energy equations for the mixture, alongside volume fraction equations for secondary phases and algebraic expressions for relative velocities. Its utility spans applications such as sedimentation, cyclone separators, particle-laden flows with low loading, and bubbly flows featuring low gas volume fractions [9].

The Eulerian model represents the most complex multiphase modelling approach within Ansys Fluent. Its procedure is based in solving a set of momentum and continuity equations for each phase, with coupling facilitated through pressure and interphase exchange coefficients. The approach to coupling varies based on the nature of the phases involved; granular (fluid-solid) flows are treated differently from nongranular (fluid-fluid) flows. In granular flows, properties are derived from the application of kinetic theory, and the momentum exchange between phases is influenced by the specific mixture under consideration. This model finds diverse applications across various scenarios, since it considers a higher amount of input information,

thus, less simplified mathematical formulations. These applications include bubble columns, risers, dense granular flows, and fluidized beds [9].

### Euler-Lagrange Approach

The Euler-Lagrange approach provides another framework for simulating multiphase flows, where distinct phases coexist and interact, yet they are described differently from a mathematical point of view [7]. The Euler-Euler approach is used to treat one or more phases (often the dominant ones) as a continuous fluid, and their properties are calculated numerically as described in the Euler-Euler Approach section, using any of the available models and their combinations. Alongside, tracking of the remaining phases occur, capturing the motion of individual particles, like gas bubbles or solid particles (usually the less prevalent ones) using a Lagrangian description. This type of description is applied to every single particle belonging to the selected dispersed phases, which usually leads to a computationally challenging calculation for dense granular or heavily aerated bubbly flows.

## **2.2.2 The Eulerian Model**

The Eulerian model available in Ansys Fluent is a powerful tool for simulating complex flows involving multiple interacting phases, including liquids, gases, and granular solid particles. It offers a versatile behaviour when it comes to the modelling of different combinations of phases, being able to handle a wide range of three-phase flow scenarios, with limitations primarily set only by computational resources. It also demonstrates the capability to produce highly detailed results due to the phase-by-phase momentum and continuity equation solving technique and the inclusion of the effect of solid-phase related parameters like granular temperature, as well as shear and bulk viscosities both derived from the principles of the kinetic theory. Interactions may also be characterized utilizing different models for drag, lift and restitution coefficients, surface tension, among other available parameters that can be calculated or set. Turbulence models including  $k - \epsilon$  and  $k - \omega$  are also compatible with the Eulerian model, and they may be applied by phase or to the whole mixture [9].

### **A. The Volume Fraction Concept**

Imagine a small control volume within a multiphase flow. The volume fraction of a specific phase (say, water in an air-water mixture) represents the portion of that control volume occupied by that particular phase. It's essentially a way to quantify how much space each phase takes up within the overall mixture. Equation 2-1 [5] represents the mathematical expression for volume fraction  $\alpha_p$  of the  $p$  phase, where  $\delta V_p$  is the volume of the  $p$  phase in the volume of  $\delta V$ , and  $\delta V^0$  is the limiting volume whereby a stationary averaging is performed.

$$\alpha_p = \lim_{\delta V \rightarrow \delta V^0} \frac{\delta V_p}{\delta V} \quad (2-1)$$

When the volume fraction of the dispersed phase is calculated, is usually referred to as void fraction and the subscript it's usually written as "d" [5]. An important characteristic of this property is that the sum of the volume fractions of the phases involved in the system must be equal to unity, as the Equation 2-2 [5] states.

$$\sum_n \alpha_n = 1 \quad (2-2)$$

Volume fractions can be used to calculate some other properties of the flowing phases, like the mixture density (Equation 2-3 [5]), where  $\alpha_n$  is the volume fraction of the  $n$ -phase and  $\rho_n$  its corresponding density; and the bulk densities of the continuous and dispersed phases (Equations 2-4 [5]), where  $\rho_p$  is the density of the  $p$ -phase,  $\alpha_p$  its volume fraction and  $\delta M_p$  its mass when represented as a limit.

$$\rho = \sum_n \alpha_n \rho_n \quad (2-3)$$

$$\bar{\rho}_p = \alpha_p \rho_p = \lim_{\delta V \rightarrow \delta V^0} \frac{\delta M_p}{\delta V} \quad (2-4)$$

Some other properties such as mixture viscosity or thermal conductivity may not be obtained through this kind of weighted averaging, thus, some other means of evaluations are required [10]. It is noticeable that the volume of a  $p$ -phase can also be described as it's shown in the equation 2-5 [9].

$$V_p = \int_V \alpha_p dV \quad (2-5)$$

A remarkable characteristic of the volume fraction property lies in its ability to serve as a boundary condition, since it inherently captures the relative amounts of each component in a multiphase mixture, it is possible to directly control the composition of the flow entering or exiting a domain in simulations and experiments.

## B. Conservation Equations

Ansys Fluent utilizes the classic conservation equations in their general form and applied to the different phases of the multiphase flow in study.

### Conservation of Mass

The continuity equation is expressed by the Equation 2-6 [9]. Here;  $\vec{v}_q$ ,  $\rho_q$  and  $\alpha_q$  are the velocity, the density, and the volume fraction of the phase  $q$ ;  $\dot{m}_{pq}$  characterizes the mass transfer from the phase  $p$  to the phase  $q$ ;  $\dot{m}_{qp}$  characterizes the mass transfer from the phase  $q$  to the phase  $p$ ; and  $S_q$  represents the source term. The terms on the right side of the equation are often related to complex mechanisms of mass transfer, usually related to phase change and chemical reactions.

$$\frac{\partial}{\partial t} (\alpha_q \rho_q) + \nabla \cdot (\alpha_q \rho_q \vec{v}_q) = \sum_{p=1}^n (\dot{m}_{pq} - \dot{m}_{qp}) + S_q \quad (2-6)$$

### Conservation of Momentum (Fluid-Fluid)

The momentum balance is expressed by the Equation 2-7 [9]. Here,  $\bar{\tau}_q$  is known as the stress-strain tensor and it's represented by the Equation 2-8, where  $\mu_q$  and  $\lambda_q$  are the shear and bulk

viscosity of the phase  $q$  [9].  $F_t$  is a term introduced to summarize all the forces involved in the momentum balance, including the external body force, the lift force, the wall lubrication force, the virtual mass force, and the turbulent dispersion force. All of these can be included in the calculations performed by Ansys Fluent, either calculated from a pre-set model or defined by expressions provided by the user. Then;  $\vec{v}_{pq}$  and  $\vec{v}_{qp}$  are the interphase velocities, related again to mass transfer between the phases;  $\vec{R}_{pq}$  is the interaction force between phases described by the Equation 2-9 [9] where  $K_{pq}$  is the interphase momentum exchange coefficient; and  $p$  is the pressure shared by all the phases involved.

$$\begin{aligned} \frac{\partial}{\partial t}(\alpha_q \rho_q \vec{v}_q) + \nabla \cdot (\alpha_q \rho_q \vec{v}_q \vec{v}_q) \\ = -\alpha_q \nabla p + \nabla \cdot \bar{\tau}_q + \alpha_q \rho_q \vec{g} + \sum_{p=1}^n (\vec{R}_{pq} + \dot{m}_{pq} \vec{v}_{pq} - \dot{m}_{qp} \vec{v}_{qp}) + F_t \end{aligned} \quad (2-7)$$

$$\bar{\tau}_q = \alpha_q \mu_q (\nabla \vec{v}_q + \nabla \vec{v}_q^T) + \alpha_q (\lambda_q - \frac{2}{3} \mu_q) \nabla \cdot \vec{v}_q \bar{I} \quad (2-8)$$

$$\sum_{p=1}^n \vec{R}_{pq} = \sum_{p=1}^n K_{pq} (\vec{v}_p - \vec{v}_q) \quad (2-9)$$

### C. Surface Tension

Surface tension arises from intermolecular forces within a fluid. Consider a spherical air bubble submerged in water. Molecules within the bulk of the bubble experience a net force of zero due to the symmetrical arrangement of neighbouring molecules. However, at the air-water interface, this symmetry is broken. Water molecules at the surface experience a net attractive force directed inwards, primarily due to unbalanced hydrogen bonding [11]. Surface tension can be also conceptualized as a tangential force acting at the interface between two immiscible fluids. Whenever two immiscible fluids come into contact, surface tension minimizes the interfacial area [12].

The effect of surface tension it's used in the modelled scenarios, as Ansys Fluent offers two different approaches for its inclusion: The Continuum Surface Force (CSF) and the Continuum Surface Stress (CSS). The CSS model provides a newer approach to the surface tension modelling, nevertheless, it doesn't provide very different results [9].

#### The Continuum Surface Force (CSF)

In the CSF model, instead of treating fluid interfaces as discontinuities, as in traditional approaches, a continuous force field is introduced within a finite transition region near the interface. This force field arises from the effects of surface tension acting on fluid elements within this region. By representing surface tension as a volume force rather than a discontinuity, the CSF model ensures a smoother transition between different fluid phases, leading to more accurate and stable numerical simulations. The mathematical formulation used by Ansys Fluent is described by the Equations 2-10, 2-11 and 2-12 [9]. Here,  $\delta\rho$  represents Kronecker delta function,  $F_{st}$  is the surface tension body force,  $C$  is the filtered colour function,  $\rho_1$  and  $\rho_2$  are the densities of phase  $q$  and phase  $p$  respectively,  $\rho$  is the mixture density,  $\kappa$  is the mean curvature of the free surface, and  $\sigma$  is the fluid surface tension coefficient.

$$F_{st} = \sigma \kappa \frac{\nabla C}{|C|} \frac{\rho}{\left(\frac{\rho_1 + \rho_2}{2}\right)} \delta \quad (2-10)$$

$$\kappa = \frac{1}{|\vec{n}|} \left[ \left( \frac{\vec{n}}{|\vec{n}|} \cdot \nabla \right) |\vec{n}| - (\nabla \cdot \vec{n}) \right] \quad (2-11)$$

$$\vec{n} = \nabla C \quad (2-12)$$

If the model is 3D, then  $F_{st}$  can be expressed as a three-component vector, and each component of  $F_{st}$  serves as a source term for the corresponding velocities in the fluid flow momentum conservation equations.

#### D. Interphase Exchange Coefficients

At this point, it's necessary to deeply define the concept of primary or wetting phase, and secondary or dispersed phases. In multiphase flow, the primary phase, also known as the wetting or continuous phase, is the phase that wets the solid surfaces it encounters. This phase tends to form continuous films or layers on the solid surfaces. The secondary phase, on the other hand, is the phase that doesn't wet the solid surfaces and typically exists as discrete droplets or bubbles dispersed within the primary phase [5].

The interphase exchange coefficient was introduced already in Equation 2-9, and it characterizes the momentum exchange between the phases in a multiphase flow. These coefficients are estimated differently depending on the phases involved, i.e. if the interactions occur between two liquid phases, or between one liquid and one solid phase. All the models available in Ansys Fluent are empirical formulations [9].

##### Fluid-Fluid Interaction

In fluid-fluid flows, it is assumed that each secondary phase forms either droplets or bubbles, which affects the assignment of each fluid to a specific phase. In cases where there is an imbalance in the quantities of the two fluids, the more abundant fluid is typically designated as the primary fluid, as the less abundant one is more prone to forming droplets or bubbles. In this case, we can define the interphase exchange coefficient as it is expressed in Equation 2-13 [5], where  $A_i$  is the interfacial area and  $f$  the drag function.  $\tau_p$  is the particulate relaxation time defined in Equation 2-14 [5], where  $d_p$  is the diameter of the bubbles or droplets of the phase  $p$  present in the phase  $q$ .

$$K_{pq} = \frac{\rho_p f}{6\tau_p} d_p A_i \quad (2-13)$$

$$\tau_p = \frac{\rho_p d_p^2}{18\mu_q} \quad (2-14)$$

It can be noted that the  $f$  function is not defined yet, since it depends on the drag coefficient  $C_D$ , which in turn depends on the relative Reynolds number  $Re$ . Different models to express these functions exist in Ansys Fluent, with the Schiller and Naumann Model being the one

selected for the scenarios considered in this thesis. This model includes the definition of the  $f$  function as it is expressed in the Equation 2-15 [9], which in turn depends on the drag coefficient calculation expressed in the Equation 2-16 [9].

$$f = \frac{C_D Re}{24} \quad (2-15)$$

$$C_D = \begin{cases} \frac{24(1 + 0.15Re^{0.687})}{Re} & \text{if } Re \leq 1000 \\ 0.44 & \text{if } Re > 1000 \end{cases} \quad (2-16)$$

The relative Reynolds number ( $Re$  in the previous expressions) refers to the Reynolds number based on the relative velocity between the phase  $q$  (primary phase) and the phase experiencing drag, in this case, the bubbles or droplets of the phase  $p$  (secondary phase). It is calculated as shown in the Equation 2-17 [9] using the relative velocity  $\vec{v}_p - \vec{v}_q$ ; characteristic length,  $d_p$ , which corresponds to the diameter of the bubbles or droplets; and fluid properties, included as the viscosity  $\mu_q$ .

$$Re_p = \frac{\rho_q |\vec{v}_p - \vec{v}_q| d_p}{\mu_q} \quad (2-17)$$

The relative Reynolds number can also be calculated for the interaction between secondary phases as it's shown in the Equation 2-18 [9], where the fluid properties are expressed as the viscosity of the mixture  $\mu_{rp} = \alpha_p \mu_p + \alpha_r \mu_r$ , and the characteristic length corresponds to the diameter of the bubbles or droplets of the secondary phase  $r$  formed within the secondary phase  $p$ .

$$Re_{rp} = \frac{\rho_q |\vec{v}_p - \vec{v}_q| d_{rp}}{\mu_{rp}} \quad (2-18)$$

### Fluid-Solid Interaction<sup>1</sup>

The characterization of the momentum exchange between a solid and a liquid phase can also be performed through an interphase exchange coefficient  $K_{sl}$ , expressed by the Equation 2-19 [5].  $\tau_s$  is the particulate relaxation time and it's expressed by the Equation 2-20 [5].

$$K_{sl} = \frac{\alpha_s \rho_s f}{\tau_s} \quad (2-19)$$

$$\tau_s = \frac{\rho_s d_s^2}{18\mu_l} \quad (2-20)$$

As in the case of Fluid-Fluid interactions, solid particles are also subjected to drag forces when they move through a liquid phase, and different specific models developed to characterize the

---

<sup>1</sup> Subindexes "s" and "l" are defined according to the association of the variable either to the solid phase or the liquid phase, respectively.



$f$  function are available in Ansys Fluent to be utilized depending on the nature of the flow. The Gidaspow model it's the most suitable one when it comes to multiphase flow where dense fluidized beds of solid particles may be formed [9]. Its governing mathematical expressions define an interphase exchange coefficient directly, and these are described by the Equations 2-21 [13] and 2-22 [13], when  $\alpha_l > 0.8$ , and by the Equation 2-23 [13] when  $\alpha_l \leq 0.8$ .

$$K_{sl} = 0.75C_D \frac{\alpha_s \alpha_l \rho_l |\vec{v}_s - \vec{v}_l|}{d_s} \alpha_l^{-2.65} \quad (2-21)$$

$$C_D = \frac{24}{\alpha_l Re_s} [1 + 0.15(\alpha_l Re_s)^{0.687}] \quad (2-22)$$

$$K_{sl} = 150 \frac{\alpha_s (1 - \alpha_l) \mu_l}{\alpha_l d_s^2} + 1.75 \frac{\rho_l \alpha_s |\vec{v}_s - \vec{v}_l|}{d_s} \quad (2-23)$$

## E. Lift Force

In multiphase flows, Ansys Fluent can account for the influence of lift forces on secondary phase particles, droplets, or bubbles. These forces arise predominantly from velocity gradients within the primary phase flow. While larger particles experience more pronounced lift effects, Ansys Fluent assumes that particle diameter significantly exceeds interparticle spacing [9].

The expression used to calculate the lift force acting on a secondary phase  $p$  within a primary phase  $q$  by Ansys Fluent is presented in the Equation 2-24 [9]. In this equation,  $C_l$  is the lift coefficient,  $\rho_q$  is the primary phase density,  $\alpha_p$  is the secondary phase volume fraction,  $\vec{v}_q$  is the primary phase velocity, and  $\vec{v}_p$  is the secondary phase velocity.

$$\vec{F}_L = -C_L \rho_q \alpha_p (\vec{v}_q - \vec{v}_p) \times (\nabla \times \vec{v}_q) \quad (2-24)$$

There're plenty of models that can provide a value for the lift coefficient  $C_l$ , and they mostly depend on the nature of the interaction between the dispersed phase and the primary phase. The Moraga model is available in Ansys Fluent to calculate a value for the lift coefficient, which is suitable for different scenarios including spherical solid particles, liquid drops and bubbles [9]. The model's lift coefficient, described by the Equation 2-26 [14], is defined by the particle Reynolds number already expressed in the Equation 2-17 and the vorticity Reynolds number expressed the Equation 2-25 [5].

$$Re_\omega = \frac{\rho_q |\nabla \times \vec{v}_q| d_p}{\mu_q} \quad (2-25)$$

$$C_l = \begin{cases} \frac{0.0767}{Re_p Re_\omega} & \text{if } Re_p Re_\omega \leq 6000 \\ \left(0.12 - 0.2e^{-\left(\frac{Re_p Re_\omega}{3.6}\right) \times 10^{-5}}\right) e^{\left(\frac{Re_p Re_\omega}{3}\right) \times 10^{-7}} & \text{if } 6000 < Re_p Re_\omega \leq 5 \times 10^{-7} \\ -0.6353 & \text{if } Re_p Re_\omega > 5 \times 10^{-7} \end{cases} \quad (2-26)$$

## F. Turbulent Dispersion Force

When simulating turbulent flows with two or more phases (like gas and liquid) using the Eulerian method, Ansys Fluent considers the effect of turbulent dispersion forces, which are important because they influence how momentum is transferred between the phases [10]. They act in a similar way to turbulent diffusion, which happens in single-phase flows. For instance, imagine a heated vertical pipe with boiling water flowing inside. Turbulent dispersion forces play a role in the vapor bubbles forming and moving around within the liquid due to the turbulent flow and the heat from the pipe wall. The way we include the effect of this force into the system is expressed in the Equation 2-27 [9].

$$K_{pq}(\vec{v}_p - \vec{v}_q) = K_{pq}(\vec{v}_p - \vec{v}_q) - f_{lim} K_{pq} \vec{v}_{dr} \quad (2-27)$$

The term on the left denotes the instantaneous drag. On the right-hand side, the initial expression, mentioned in Equation 2-9, represents the average momentum transfer between phases and it involves the interphase exchange coefficient detailed in Interphase Exchange Coefficients section, and the mean phase velocity vectors  $\vec{v}_p$  and  $\vec{v}_q$ . The second term,  $-f_{lim} K_{pq} \vec{v}_{dr}$ , represents the turbulent dispersion force itself (usually denoted by  $F_{td}$ ), where  $\vec{v}_{dr}$  is the drift velocity and it's related to the dispersion of the secondary phases due to transport by turbulent fluid motion. It can be noted that a multiplier,  $f_{lim}$ , is introduced into the formula. This term is called limiting function for turbulent dispersion force, and it's mainly focused on the imposition of a threshold to terminate the effect of the turbulent dispersion force. This last function is not used for the models treated in this thesis.

Various different models for incorporating the effect of the turbulent dispersion into a simulation are available in Ansys Fluent, being the one utilized for the scenarios considered in this thesis the Simonin Model. When a per-phase turbulence model is used, then the Simonin Model introduces the Equation 2-28 [15] to calculate the turbulent dispersion force  $F_{td}$ . In this equation,  $C_{TD}$  is an inherent constant of the model that can be approximated to 1,  $\sigma_{pq}$  is the Prandtl number (equal to 0.75), and  $\nabla\alpha_p$  is the gradient of dispersed phase volume fraction.

$$F_{td} = C_{TD} \frac{K_{pq}}{\sigma_{pq}} \left( \frac{\mu_p \nabla\alpha_p}{\rho_p \alpha_p} - \frac{\mu_q \nabla\alpha_q}{\rho_q \alpha_q} \right) \quad (2-28)$$

In the scenarios modelled in this thesis, the selected turbulence model corresponds to the SST  $k - \omega$  model applied in per-phase modality, making  $\nabla\alpha_p$  a relevant variable. In case the turbulence model is applied in a mixture mode, this variable equals to the mixture turbulent kinematic viscosity [9].

## G. Solids Pressure

In Ansys Fluent, multiphase simulations employing the Eulerian approach utilize the so-called concept of Solids Pressure. This expression doesn't represent pressure in the classical sense, but rather a contribution to the forces acting on the solid phase. Imagine solid particles suspended in a fluid, like sand in water, here the particles interact and collide, creating an

outward force similar to pressure. This interaction term is captured by the solids pressure concept.

For compressible granular flows (where the solids volume fraction is less than its maximum allowed value), the concept becomes more intricate. Here, an independent solids pressure calculation is used for the pressure gradient term ( $\nabla P_s$ ) within the granular-phase momentum equation. Since a Maxwellian velocity distribution describes the particles, a "granular temperature" is introduced [5], appearing in the expression for solids pressure and viscosities. This solids pressure itself has two components: The kinetic term which accounts for the random motion of the particles, and the collisional term which represents the forces arising from particle collisions [9].

The mathematical formulation for  $p_s$  is presented in Equation 2-29 [9]. Here,  $e_{ss}$  is the coefficient of restitution for particle collisions,  $g_{0,ss}$  is the radial distribution function,  $\alpha_s$  is the solid phase volume fraction, and  $\theta_s$  is the granular temperature.

$$p_s = \alpha_s \rho_s \theta_s + 2\rho_s (1 + e_{ss}) \alpha_s^2 g_{0,ss} \theta_s \quad (2-29)$$

It's worth noting that the Equation 2-29 doesn't consider the influences of other solid phases in case they exist.

#### H. Radial Distribution Function

The radial distribution function ( $g_0$ ) is a factor that corrects the probability of collisions between particles when the solid phase becomes dense. Its formulation is described in the Equation 2-30 [9], where  $s$  is the distance between grains, and  $d_p$  their characteristic length. According to this formulation, for a dilute solid phase (where particles are far apart),  $g_0$  approaches 1, indicating a collision probability close to that of non-interacting spheres. Conversely, when the solid phase becomes compact (particles are very close),  $g_0$  increases towards infinity, suggesting a much higher likelihood of collisions due to the tightly packed arrangement. The concept of the radial distribution function is analogous to the factor used in Chapman and Cowling's theory of nonuniform gases. In their theory, a similar factor accounts for the influence of molecular crowding on collision probabilities within a gas. Similar to  $g_0$ , this factor equals 1 for a dilute gas and increases as the gas becomes denser [16].

$$g_0 = \frac{s + d_p}{s} \quad (2-30)$$

Ansys Fluent incorporates a radial distribution fraction expression based on the work of D. Gidaspow with some modifications for its application to multiple solid phases running in a multiphase flow (Ma-Ahmadi model, for instance) [13]. The packing limit calculation method is also modified to consider the interaction between particles of different sizes, which inherently have different packing limits alone [9]. For simplicity and since the diameter of the particles do not differ much in the scenarios treated in this thesis, the packing limits of the solid phases are considered equal.

#### I. Solids Shear Stresses

In Ansys Fluent simulations involving granular flows, understanding solids shear stresses is crucial. These stresses originate from the interactions and movements of solid particles within the flow, impacting the overall behaviour of the solid phase.

The concept of solids shear stresses is rooted in the solids stress tensor. This tensor not only accounts for the shear stresses but also incorporates the bulk viscosity experienced by the solid phase, thus, both contribute to the momentum exchange between particles due to their translational motion and collision. Three key components can be identified in the Equation 2-31 [9], which is the mathematical formulation of this tensor. The collisional part arises from direct collisions between particles, representing the energy dissipation resulting from these interactions. This interaction is expressed through the collisional viscosity  $\mu_{s,col}$ . The kinetic part originates from the random motion of the particles within the granular phase, i.e., it reflects the internal energy associated with this phenomenon. This interaction is represented by the kinetic viscosity  $\mu_{s,kin}$ . The frictional part, which is often considered optional to include, accounts for the viscous-plastic transition that occurs when the solid phase reaches a critical packing density, in other words, it captures the increased resistance to flow caused by friction between the tightly packed particles. This effect is represented by the frictional viscosity  $\mu_{s,fr}$ .

$$\mu_s = \mu_{s,col} + \mu_{s,kin} + \mu_{s,fr} \quad (2-31)$$

### Collisional Viscosity

As the particles move and interact with each other, they collide, transferring momentum and losing some kinetic energy in the process. This energy loss contributes to the overall resistance of the solid phase to deformation, which is what the collisional viscosity represents. The modelling in Ansys Fluent occurs as shown in the Equation 2-32 [13].

$$\mu_{s,col} = \frac{4}{5} \alpha_s \rho_s d_s g_{0,ss} (1 + e_{ss}) \left( \frac{\Theta_s}{\pi} \right)^{0.5} \quad (2-32)$$

### Kinetic Viscosity

Unlike collisional viscosity that focuses on energy loss from collisions, kinetic viscosity captures the influence of the random motion of the particles within the granular phase. In Ansys Fluent, there're two models available to calculate this variable, being the Gidaspow model the one selected for the simulation scenarios treated in this thesis. Its formulation is shown in Equation 2-33 [17].

$$\mu_{s,kin} = \frac{10}{96} \frac{\rho_s d_s \sqrt{\Theta_s \pi}}{\alpha_s (1 + e_{ss}) g_{0,ss}} \left[ 1 + \frac{4}{5} g_{0,ss} \alpha_s (1 + e_{ss}) \right]^2 \quad (2-33)$$

### Frictional Viscosity

As the solid volume fraction of a solid phase within a granular flow increases, the space available for individual particle movement decreases. When the packing density reaches a certain limit, the particles become tightly packed, and friction between them becomes a significant factor. This frictional interaction leads to a rise in the overall resistance of the solid phase to deformation. The Schaffer frictional viscosity model quantifies this additional resistance, and its mathematical formulation is expressed by the Equation 2-34 [18], where  $p_{fr}$  is the frictional pressure,  $\varphi$  is the angle of internal friction, and  $I_{2D}$  is the second invariant of

the deviatoric stress tensor. The frictional pressure can be modelled using the Johnson and Jackson model, which is detailed in the Equation 2-35 [18] , where  $Fr = 0.08\alpha_s$ .

$$\mu_{s,kin} = \frac{p_{fr} \sin \varphi}{2\sqrt{I_{2D}}} \quad (2-34)$$

$$p_{fr} = Fr \frac{(\alpha_s - \alpha_{s,min})^2}{(\alpha_{s,max} - \alpha_s)^5} \quad (2-35)$$

## J. Granular Temperature

It's useful to imagine the following situation to describe the granular temperature concept: Sand flowing down a chute exhibits similar characteristics when compared to a fluid; since particles collide, transfer momentum, and exhibit some degree of random motion. This motion, even in the absence of actual temperature increase, contributes to the overall behaviour of the granular flow. Granular temperature essentially quantifies the average kinetic energy of this random fluctuating motion of the particles. It's not a measure of actual temperature in the classical sense, but rather a parameter introduced in granular flow theory to model the energy associated with particle movement.

Moving to the mathematical formulation, we can formulate the transport equation based on the principles of the kinetic theory, as shown in the Equation 2-36 [19].

$$\frac{3}{2} \left[ \frac{\partial}{\partial t} (\rho_s \alpha_s \theta_s) + \nabla \cdot (\rho_s \alpha_s \vec{v}_s \theta_s) \right] = (-p_s \bar{I} + \bar{\tau}_s) : \nabla \vec{v}_s + \nabla \cdot (k_{\theta_s} \nabla \theta_s) - \gamma_{\theta_s} + \varphi_{ls} \quad (2-36)$$

In this equation, the different terms represent different phenomena that are worth mentioning:  $(-p_s \bar{I} + \bar{\tau}_s) : \nabla \vec{v}_s$  represents the generation of energy by the solid stress tensor;  $k_{\theta_s} \nabla \theta_s$  represents the energy diffusion where  $k_{\theta_s}$  is the diffusion coefficient;  $\gamma_{\theta_s}$  represents the collisional dissipation of energy; and  $\varphi_{ls}$  is the energy exchange between the  $l^{th}$  fluid or solid phase and the  $s^{th}$  solid phase [9]. Ansys Fluent provides two different models to obtain the coefficient of granular energy  $k_{\theta_s}$ , being the one selected for the models treated in this thesis the Gidaspow et al method. Its mathematical formulation is shown in the Equation 2-37 [17]. On the other hand, the collisional dissipation of energy  $\gamma_{\theta_s}$  is calculated thanks to the model proposed by Lun et al and it's shown in the Equation 2-38 [17]. Finally, the transfer of kinetic energy defined by the term  $\varphi_{ls}$  is once again derived from the work of Gidaspow et al and it's expressed in the Equation 2-39 [17].

$$k_{\theta_s} = \frac{150d_s\rho_s\sqrt{\theta_s\pi}}{384(1+e_{ss})g_{0,s}} \left[ 1 + \frac{6}{5}\alpha_s g_{0,ss}(1+e_s) \right]^2 + 2\rho_s\alpha_s^2 d_s(1+e_{ss})g_{0,ss} \sqrt{\frac{\theta_s}{\pi}} \quad (2-37)$$

$$\gamma_{\theta_s} = \frac{12(1-e_{ss}^2)g_{0,ss}}{d_s\sqrt{\pi}} \rho_s\alpha_s^2 \theta_s^{3/2} \quad (2-38)$$

$$\varphi_{ls} = -3K_{ls}\theta_s \quad (2-39)$$

It's worth noting that Ansys Fluent neglects by default the convection and diffusion effects present in the Equation 2-36, in order to effectively obtain a result for the granular temperature [9]. This treatment can be manually adapted for different uses where these phenomena is relevant.

## 2.3 Turbulence Modelling

This chapter introduces the k- $\omega$  Shear-Stress Transport (SST) turbulence model chosen for simulating turbulent flow of granular materials in open channels using Ansys Fluent. It's worth mentioning that there're different models to include the effects of turbulence into simulations of granular flows, but the SST  $k - \omega$  stands out due to its computationally efficient execution within the Ansys Fluent Software and some key theoretic-related advantages: the flow separation handling and the wall compatibility with the presence of solid particles. To understand the principles of the SST  $k - \omega$  is necessary to study the formulations for the Standard  $k - \omega$  model, introduced by Wilcox et al in 1988 [20] and the BSL  $k - \omega$  model introduced by Menter et al in 1994 [21].

### Standard $k - \omega$ Model

The standard k- $\omega$  turbulence model treats turbulence by relying on two transport equations. The first equation, shown as Equation 2-40 [9], deals with turbulence kinetic energy, denoted by "k". This variable signifies the energy present within the turbulent motion itself. The second equation, shown as Equation 2-41 [9], describes the specific dissipation rate, symbolized by " $\omega$ ". This variable reflects how quickly this turbulent energy dissipates and converts into heat.

$$\frac{\partial}{\partial t}(\rho k) + \frac{\partial}{\partial x_i}(\rho k u_i) = \frac{\partial}{\partial x_j} \left( \Gamma_k \frac{\partial k}{\partial x_j} \right) + G_k - Y_k + S_k + G_{bk} \quad (2-40)$$

$$\frac{\partial}{\partial t}(\rho \omega) + \frac{\partial}{\partial x_i}(\rho \omega u_i) = \frac{\partial}{\partial x_j} \left( \Gamma_\omega \frac{\partial \omega}{\partial x_j} \right) + G_\omega - Y_\omega + S_\omega + G_{\omega b} \quad (2-41)$$

These transport equations incorporate various terms to account for different physical phenomena. The production term ( $G_k$ ) in the  $k$  equation reflects the generation of turbulent kinetic energy due to shear in the mean flow. Conversely, the dissipation term ( $Y_k$ ) represents the loss of turbulence kinetic energy due to viscous effects at small scales. An additional source term ( $S_k$ ) allows users to account for specific scenarios where turbulence kinetic energy might be generated through mechanisms not directly captured by the model. Similarly, the  $\omega$  equation also includes production ( $G_\omega$ ) and dissipation ( $Y_\omega$ ) terms. The production term is often linked to the production of turbulence kinetic energy, reflecting the generation of the specific

dissipation rate [9]. Dissipation of  $\omega$  due to viscous effects is represented by  $Y_\omega$  as well. Finally, a source term ( $S_\omega$ ) provides the flexibility to incorporate additional mechanisms influencing the specific dissipation rate.  $G_{bk}$  and  $G_{b\omega}$  account for buoyancy effects, often neglected for granular flows [9].  $\Gamma_k$  and  $\Gamma_\omega$  are the so-called effective diffusivities of  $k$  and  $\omega$ , and they are derived from the Equations 2-42 [9] and 2-43 [9], where the turbulent viscosity is model according to  $\mu_t = \alpha\rho k/\omega$ .

$$\Gamma_k = \mu + \frac{\mu_t}{\sigma_k} \quad (2-42)$$

$$\Gamma_\omega = \mu + \frac{\mu_t}{\sigma_\omega} \quad (2-43)$$

The model solves these two transport equations alongside the primary fluid flow equations and this combined solution allows for the prediction of the overall flow behavior while accounting for turbulence [9]. The strengths of this model include its ability to handle various flow conditions. It incorporates modifications for low-Reynolds number effects, compressibility, and shear flow spreading. Low-Reynolds number effects are crucial near walls, compressibility becomes important for high-speed flows, and shear flow spreading refers to the expansion of a shear layer between different fluid streams. An additional benefit is the improved accuracy for predicting free shear flows, that can be defined as flows where mixing layers exist between distinct fluid streams [22]. The improvement comes from the inclusion of production terms within the equations. However, the standard  $k - \omega$  model has a weakness: It can be sensitive to the initial values chosen for  $k$  and  $\omega$  outside the turbulent region, also known as the freestream [9]. This sensitivity can significantly impact the results, particularly for free shear flows. It's also important to remember that the standard  $k - \omega$  model is empirical, i.e. it relies on data gathered from experiments and incorporates adjustments to achieve accurate results.

### Turbulence Production

There are two turbulence production terms that need to be modelled. The first one is related to the production of  $k$ ,  $G_k$ , which is expressed in Equation 2-44 [20]. A simplified calculation for this term is shown in the Equation 2-45 [20] and it's based on the Boussinesq hypothesis [9] to relate the Reynolds stresses to the mean strain rate of the flow. Here,  $S$  corresponds to the modulus of the mean rate-of-strain tensor, taken from the formulation of the  $k - \epsilon$  model and expressed by the Equation 2-46 [23]. The rate-of-strain tensor concept is worth describing at this point. It is a fundamental concept in continuum mechanics, particularly in fluid dynamics, used to describe how quickly and in what way a fluid element is deformed at a specific point.  $S_{ij}$  then, are the individual components of the rate-of-strain tensor. There are nine components ( $i$  and  $j$  can take values 1, 2, and 3 representing the  $x$ ,  $y$ , and  $z$  directions) that describe the different types of deformation (elongation, compression, and shear) in a 3D flow.

$$G_k = -\rho \overline{\mu_i' \mu_j'} \frac{\partial u_j}{\partial x_i} \quad (2-44)$$

$$G_k = \mu_t S^2 \quad (2-45)$$

$$S = \sqrt{2S_{ij}S_{ij}} \quad (2-46)$$

The production of  $\omega$ ,  $G_\omega$ , it's dependent on  $G_k$  and it's represented by the Equation 2-47 [20], where  $\alpha$  is a coefficient presented in Equation 2-48 [20],  $Re_t$  by Equation 2-49 [20],  $\alpha^*$  by Equation 2-50,  $R_\omega = 2.95\alpha^*$ ,  $\alpha_0 = 0.024$ ,  $R_k = 6$ ,  $\alpha_\infty^* = 1$ , and  $\alpha_\infty = 0.52$ .

$$G_\omega = \frac{\alpha \omega G_k}{k} \quad (2-47)$$

$$\alpha = \frac{\alpha_\infty}{\alpha^*} \left( \frac{\alpha_0 + \frac{Re_t}{R_\omega}}{1 + \frac{Re_t}{R_\omega}} \right) \quad (2-48)$$

$$Re_t = \frac{\rho k}{\mu \omega} \quad (2-49)$$

$$\alpha^* = \alpha_\infty^* \left( \frac{\alpha_0 + \frac{Re_t}{R_\omega}}{1 + \frac{Re_t}{R_\omega}} \right) \quad (2-50)$$

### Turbulence Dissipation

Once again, there are two terms in the transport equations that need to be modelled in order to include the turbulence dissipation effects, one for  $k$  ( $Y_k$ ), and one for  $\omega$  ( $Y_\omega$ ). Based on the mathematical formulation of the standard  $k - \omega$  model,  $Y_k$  can be calculated as it's shown in Equation 2-51 [20]. The values for  $f_{\beta^*}$  can be calculated as it's shown in Equation 2-52 [20],  $X_k$  as it's shown in Equation 2-53 [20], and  $\beta_i^*$  as it's shown in Equation 2-54. The function  $F(M_t)$  accounts for the compressibility effect on the dissipation of turbulence, and it can be calculated as it's shown in Equation 2-55 [20], Where  $M_t^2 = 2k/\gamma RT$  and  $M_{t0} = 0.25$ . The remaining constants take the following values when using this model:  $\zeta^* = 1.5$ ,  $R_\beta = 8$ ,  $\beta_\infty^* = 0.09$ .



$$Y_k = \rho \beta^* f_{\beta^*} k \omega \quad (2-51)$$

$$f_{\beta^*} = \begin{cases} 1 & \text{if } X_k \leq 0 \\ \frac{1 + 680X_k^2}{1 + 400X_k^2} & \text{if } X_k > 0 \end{cases} \quad (2-52)$$

$$\beta^* = \beta_i^* [1 + \zeta^* F(M_t)] \quad (2-53)$$

$$\beta_i^* = \beta_{\infty}^* \left( \frac{\frac{4}{5} + \left(\frac{Re_t}{R_{\beta}}\right)^4}{1 + \left(\frac{Re_t}{R_{\beta}}\right)^4} \right) \quad (2-54)$$

$$F(M_t) = \begin{cases} 0 & \text{if } M_t \leq M_{t0} \\ M_t^2 - M_{t0}^2 & \text{if } M_t > M_{t0} \end{cases} \quad (2-55)$$

On the other hand,  $Y_{\omega}$  can be calculated using the Equation 2-56. The values of  $f_{\beta}$  are obtained according to Equation 2-57,  $X_{\omega}$  according to Equation 2-58,  $\beta$  according to Equation 2-59, and  $\Omega_{ij}$  according to Equation 2-60.

$$Y_{\omega} = \rho \beta f_{\beta} \omega^2 \quad (2-56)$$

$$f_{\beta} = \frac{1 + 70X_{\omega}}{1 + 80X_{\omega}} \quad (2-57)$$

$$X_{\omega} = \left| \frac{\Omega_{ij} \Omega_{jk} S_{ki}}{(\beta_{\infty}^* \omega)^3} \right| \quad (2-58)$$

$$\beta = \beta_i \left[ 1 - \frac{\beta_i^*}{\beta_i} \zeta^* F(M_t) \right] \quad (2-59)$$

$$\Omega_{ij} = \frac{1}{2} \left( \frac{\partial u_i}{\partial x_j} - \frac{\partial u_j}{\partial x_i} \right) \quad (2-60)$$

### Baseline $k - \omega$ Model

The standard  $k - \omega$  model is known to be very sensitive to the initial values of turbulence properties set at the flow boundaries (freestream conditions), and this sensitivity can lead to inaccurate results. To address this issue, Menter et al developed the Baseline (BSL) model in 1994 [21]. This model combines the strengths of two existing models: The Standard  $k - \omega$  Model and the older  $k - \epsilon$  model. The BSL model achieves this synergy through a two-step approach. Firstly, it transforms the Wilcox model into a formulation compatible with the  $k - \epsilon$  framework, then secondly, it utilizes a blending function that activates either the transformed  $k - \omega$  model or the standard  $k - \epsilon$  model depending on the proximity to the wall. This ensures

the model prioritizes the Wilcox model's accuracy near walls and seamlessly transitions to the  $k-\varepsilon$  model's freestream independence in the far field. The BSL model transport equations are similar to the ones used by the Standard model, with the only addition of one term in the “ $\omega$ ” equation,  $D_\omega$ , which represents the cross-diffusion of turbulence. These formulations are shown in Equations 2-61 [21] and 2-62 [21].

$$\frac{\partial}{\partial t}(\rho k) + \frac{\partial}{\partial x_i}(\rho k u_i) = \frac{\partial}{\partial x_j} \left( \Gamma_k \frac{\partial k}{\partial x_j} \right) + G_k - Y_k + S_k + G_{bk} \quad (2-61)$$

$$\frac{\partial}{\partial t}(\rho \omega) + \frac{\partial}{\partial x_i}(\rho \omega u_i) = \frac{\partial}{\partial x_j} \left( \Gamma_\omega \frac{\partial \omega}{\partial x_j} \right) + G_\omega - Y_\omega + D_\omega + S_\omega + G_{\omega b} \quad (2-62)$$

The blending function is a crucial part of this model's formulation since it's included in the calculation of different variables. To calculate the value of this variable, three equations are practically presented. The first one is the blending function itself,  $F_1$ , which is presented in the Equation 2-63 [9]; the second one is the auxiliary function  $\Phi_1$ , shown in the Equation 2-64 [9]; the third one is the positive portion of the cross-diffusion term,  $D_\omega^+$ , which is shown in the Equation 2-65 [9]. The constant  $\sigma_{\omega,2}$  takes a value of 1. The  $y$  variable accounts for the distance to the next surface.

$$F_1 = \tanh(\Phi_1^4) \quad (2-63)$$

$$\Phi_1 = \min \left[ \max \left[ \left( \frac{\sqrt{k}}{0.09\omega y}, \frac{500\mu}{\rho y^2 \omega} \right), \frac{4\rho k}{\sigma_{\omega,2} D_\omega^+ y^2} \right] \right] \quad (2-64)$$

$$D_\omega^+ = \max \left[ 2\rho \frac{1}{\sigma_{\omega,2}} \frac{1}{\omega} \frac{\partial k}{\partial x_j} \frac{\partial \omega}{\partial x_j}, 10^{-10} \right] \quad (2-65)$$

The production term  $G_k$  remains unchanged from the standard  $k - \omega$  model formulation, meanwhile the production term  $G_\omega$  changes according to the Equation 2-66 [21], where the auxiliary  $\alpha_\infty$  constant is calculated according to the Equation 2-67 [21], 2-68 and 2-69 [21]. Here the additional constants take the following values:  $\beta_\infty^* = 0.09$ ,  $\beta_{i,1} = 0.075$ ,  $\beta_{i,2} = 0.0828$ ,  $\sigma_{\omega,1} = 2$  and  $\kappa = 0.41$  [21].

$$G_\omega = \frac{\alpha\alpha^*}{\nu_t} G_k \quad (2-66)$$

$$\alpha_\infty = F_1\alpha_{\infty,1} + (1 - F_1)\alpha_{\infty,2} \quad (2-67)$$

$$\alpha_{\infty,1} = \frac{\beta_{i,1}}{\beta_\infty^*} - \frac{\kappa^2}{\sigma_{\omega,1}\sqrt{\beta_\infty^*}} \quad (2-68)$$

$$\alpha_{\infty,2} = \frac{\beta_{i,2}}{\beta_\infty^*} - \frac{\kappa^2}{\sigma_{\omega,2}\sqrt{\beta_\infty^*}} \quad (2-69)$$

The dissipation term  $Y_k$  is similarly evaluated compared to the standard  $k - \omega$  model, the difference lies in the way  $f_{\beta^*}$  is calculated, which in the case of the BSL  $k - \omega$  model is always equal to 1 and not a piecewise function [9]. On the other hand, the dissipation term  $Y_\omega$  is subjected to two changes compared to the standard  $k - \omega$  model (See Equation 2-56): The  $f_\beta$  constant is always equal to 1, and the  $\beta$  constant is now calculated according to the Equation 2-70 [21].

$$\beta = F_1\beta_{i,1} + (1 - F_1)\beta_{i,2} \quad (2-70)$$

Two more important modifications are incorporated into the BSL model, specifically into the effective diffusivities (Equations 2-42 and 2-43), where the Prandtl numbers,  $\sigma_k$  and  $\sigma_\omega$ , are calculated as it's shown in Equation 2-71 [21] and 2-72 [21]. Here, the last two constants for the model are present:  $\sigma_{k,1} = 2$  and  $\sigma_{k,2} = 1$  [21]. Finally, the cross-diffusion term can be calculated as it's shown in the Equation 2-73 [9].

$$\sigma_k = \frac{1}{\frac{F_1}{\sigma_{k,1}} + \frac{1 - F_1}{\sigma_{k,2}}} \quad (2-71)$$

$$\sigma_\omega = \frac{1}{\frac{F_1}{\sigma_{\omega,1}} + \frac{1 - F_1}{\sigma_{\omega,2}}} \quad (2-72)$$

$$D_\omega = 2(1 - F_1)\rho \frac{1}{\omega\sigma_{\omega,2}} \frac{\partial k}{\partial x_j} \frac{\partial \omega}{\partial x_j} \quad (2-73)$$

### The Shear-Stress Transport (SST) $k - \omega$ Model

The SST  $k - \omega$  model builds upon the BSL model's capabilities by incorporating the transport of turbulence shear stress into the definition of turbulent viscosity. This additional factor, detailed by Menter et al, enhances the SST model's accuracy and reliability for a wider range

of flow phenomena. Compared to the standard and BSL models, the SST model demonstrates superior performance in handling flows with adverse pressure gradients, airfoils, and transonic shock waves. All the equations are the same as in the BSL model, nevertheless, the formulation for the turbulent viscosity is expressed through new values for some of its constants:  $\sigma_{\omega,2} = 1.176$  and  $a_1 = 0.31$ . The new expression for the calculation of the turbulent viscosity, alongside the auxiliary variables  $F_2$  and  $\Phi_2$ , are shown in Equation 2-74, 2-75 and 2-76 [21].

$$\mu_t = \frac{\rho k}{\omega} \frac{1}{\max\left[\frac{1}{\alpha^*}, \frac{SF_2}{a_1 \omega}\right]} \quad (2-74)$$

$$F_2 = \tanh(\Phi_2^2) \quad (2-75)$$

$$\Phi_2 = \max\left[2 \frac{\sqrt{k}}{0.09 \omega y}, \frac{500 \mu}{\rho y^2 \omega}\right] \quad (2-76)$$

## 2.4 Numerical Solver Aspects

### Numerical Solvers

Ansys Fluent offers a variety of numerical solvers tailored for different types of Computational Fluid Dynamics problems. Two main categories exist: The Pressure-Based Solvers and the Density-Based Solvers.

The pressure-based solvers are ideal for incompressible or low-speed compressible flows (Mach number below 0.3) [5]. They solve for pressure and velocity fields simultaneously, making them efficient for steady-state and transient simulations with complex geometries. However, they may struggle with highly compressible flows where density variations become significant. The density-based solvers are designed for compressible flows at any speed, these solvers directly solve the governing equations for all flow variables (density, momentum, and energy) simultaneously [24]. This approach allows for accurate capture of shock waves and other phenomena associated with high-speed flows. However, density-based solvers can be computationally more expensive compared to pressure-based solvers for low-speed applications [9].

When a granular multiphase flow is modelled, being water the primary phase, a pressure-based solver is the best option for multiple reasons: the incompressible nature of the solid-liquid part of the flow, the handling of the complex interfaces, and the computational costs. flows are typically considered incompressible, even when the air is considered as a phase in the system. While there might be slight density variations due to pressure changes, the overall density remains relatively constant in the liquid-solid zone of the flow, being the gaseous zone usually not the one where phenomena must be accurately captured. Since granular flow also involves the interaction between water and solid particles, and pressure-based solvers perform well at handling these interfaces because they solve for pressure and velocity simultaneously. This allows for a more robust capture of pressure gradients and interfacial forces crucial for accurate representation of the multiphase flow. Density-based solvers, while powerful for compressible flows, can be computationally expensive for incompressible or nearly incompressible simulations. The additional complexity of solving for density variations becomes unnecessary for granular flows, where pressure-based solvers offer a more efficient and cost-effective approach.

### Spatial Discretization Schemes

Numerical simulations in Ansys Fluent rely on dividing the computational domain into smaller spatial elements (cells). These discretization schemes come into play when approximating the governing equations within these elements, thus, they determine how information like flow variables is transferred between neighbouring cells. While multiple approaches are offered in Ansys Fluent for spatial discretization, only the ones that were used for the models treated on this thesis are briefly discussed in this chapter: The First-Order Upwind Scheme and the Second Order Scheme (specifically for pressure calculations). The right choice between them depends on the desired accuracy and the specific flow regime being simulated, nevertheless, the computational cost is usually the limiting factor [24].

The first-order upwind scheme is a simple and computationally inexpensive scheme. It uses the flow variable from the upwind cell (the cell facing the opposite direction of the flow) to approximate the value at the current cell face [9]. While efficient, it can introduce numerical diffusion, smearing out sharp gradients in the flow field, which can be problematic for capturing details like shock waves [9]. This scheme is the most appropriate one when the computational power is limited, i.e. when user-oriented or basic workstations are being used for the modelling.

The second order pressure discretization scheme prioritizes accuracy in calculating the pressure field within the computational domain. This approach solves the convective term in the pressure equation by incorporating pressure values from both the upwind (flow origin) and downwind neighbour cells. This broader consideration compared to the first-order scheme (using only the upwind value) leads to a more refined representation of the pressure distribution, especially for smooth and predictable flows. However, the increased accuracy comes with a potential trade-off. Second-order discretization can be more prone to convergence difficulties, particularly in scenarios with intricate flow features or significant pressure variations [9].

### Gradient Evaluation

Ansys Fluent offers various gradient evaluation schemes to approximate the change of a variable (like pressure, velocity, or other scalars) across a computational domain discretized into cells. These schemes play an important role in the accuracy and efficiency of CFD simulations, just like the spatial discretization schemes, and once again its choice may be oriented to the less demanding models if a basic workstation is used. Only one method was utilized in the simulations treated by this thesis: The Cell-Based Scheme.

The cell-based scheme offers a simple and computationally inexpensive approach. It estimates the gradient by averaging the variable's value at the cell centre with its neighbours [24]. While this method is efficient, its reliance on averaging can lead to reduced accuracy, especially for flows with sharp variations or intricate geometries [9].

### Double Precision

When double precision is chosen in Ansys Fluent, the solver performs all calculations using this higher precision level, which translates to enhanced accuracy, particularly relevant for simulations involving intricate physics or highly sensitive outcomes. Double precision also allows the solver to represent a broader spectrum of magnitudes. Nevertheless, employing double precision comes with some difficulties, like the requirement of double the memory compared to single precision, which can be a limiting factor for large or intricate models. The choice between single and double precision is context dependent. While single precision serves as the default option and often suffices for many simulations, double precision might be necessary in specific scenarios. For instance, if the outcome of your simulation is critical and small errors can significantly impact conclusions, double precision becomes a necessity.

This is usually the case when simulating multiphase flows [9]. Similarly, simulations involving intricate physical phenomena or exhibiting highly non-linear behaviour can benefit from the enhanced accuracy provided by double precision.

### Parallel Processing

The Ansys Fluent software offers the "Parallel (Local Machine)" functionality, which is intended to configure parallel processing capabilities, i.e. a technique that distributes the computational workload across multiple cores or processors in a computer, leading to faster execution. Optimizing this option requires careful consideration of two key factors: the number of cores available and the total random-access memory (RAM) capacity.

The ideal number of cores to utilize depends on the complexity of the simulation and the limitations imposed by available memory. A general starting point suggests using a number of cores equal to the physical cores present on the machine (or slightly less) [25]. Assigning an excessive number of cores can lead to diminishing returns due to memory constraints and the communication overhead incurred when data is exchanged between cores.

Available memory plays an equally crucial role. Parallel processing necessitates sufficient memory to accommodate the solver's data structures and temporary storage needs when distributed across multiple cores. Ansys Inc. recommends 8 GB of RAM per core [25].

## 2.5 Meshing Considerations

Generating a high-quality mesh is crucial for obtaining accurate and reliable results from CFD simulations. In this study, we employed the best possible practices to ensure the mesh effectively captures the flow behaviour within the flume, and they can be explained based on three key control aspects.

### Global Mesh Size Selection:

A base mesh size of 4 [mm] was chosen for this study, selection that balances computational efficiency with sufficient resolution to capture the key flow features. Factors considered during mesh size selection included the flume geometry, expected flow gradients, and desired level of detail in the results. This mesh size provided a good compromise between capturing the flow phenomena of interest while maintaining reasonable computational cost.

### Wall Refinement:

Recognizing the influence of wall roughness on the flow behaviour, a refinement level of 3 (refinement up to a third of the base mesh size) was applied to all walls with roughness within the flume system. This refinement ensures a higher mesh density near the walls, capturing the effects of wall shear stress and boundary layer development more accurately. By refining the mesh near the walls, we can better resolve the thin viscous sublayer adjacent to the walls, which is critical for accurate prediction of turbulent flows.

### Mesh Quality Control:

Throughout the mesh generation process, a focus was placed on maintaining good mesh quality. This involved ensuring proper element aspect ratios, minimizing skewness and kurtosis, and avoiding highly distorted cells.

## 2.6 Other Equations Used

### 2D Formula for Development Length of Flow in Open Channel

In open channel hydraulics, the development length  $L_d$  is defined as the distance from the channel entrance to the point where the flow becomes fully developed. In fully developed flow, the velocity profile remains consistent along the flow direction, indicating that the effects of the

channel entrance and initial conditions have dissipated. The derivation of this development length in a two-dimensional (2D) context, particularly for a rectangular channel, involves understanding the hydraulic diameter and its relationship to flow characteristics. This variable is presented through Equation 2-77 [26] on its three-dimensional form, where  $b$  corresponds to the width of a rectangular channel, and  $h$  is the flow depth in a developed state. When  $b \gg h$  then Equation 2-78 [26] represents the hydraulic diameter, which can perfectly be a good approximation for a two-dimensional channel, where hypothetically, the effects sidewalls do not influence the flow.

$$D_h = \frac{4(bh)}{b + 2h} \quad (2-77)$$

$$D_h \approx 4h \quad (2-78)$$

The development length  $L_d$  in turbulent flow is empirically related to the hydraulic diameter. Experimental observations and theoretical analyses suggest that the development length can be expressed as a multiple of the hydraulic diameter with a coefficient  $\alpha$ , as shown in Equation 2-79 [26]. Here,  $\alpha$  is a coefficient that varies between 10 and 20 for turbulent flows. For analysis purposes,  $L_{d,min}$  is considered to be associated to the lower  $\alpha = 10$  limit, and  $L_{d,max}$  to be associated with the higher  $\alpha = 20$  limit.

$$L_d = \alpha D_h \quad (2-79)$$

### 3. Methodology

#### 3.1 Conditions and Assumptions for Modelled Flow

As discussed in the Introduction chapter, the motivation for this research comes from the experimental work conducted at the hydraulics laboratory of the Czech Technical University in Prague. To establish a close link between the numerical simulations and the laboratory experiments, the geometry and granular material characteristics employed in this study are directly based on those used in the experimental setup. Therefore, a description of the modelling approach necessitates first outlining the key geometrical dimensions of the system and the properties of the particles (size and density) used in the laboratory experiments. Subsequently, a summary of the configuration characteristics for the numerical models will be provided. This flume offers the ability to investigate sediment transport under various flow conditions. Here's a description of the flume's key characteristics:

- **Dimensions:** The flume has a width of 0.2 meters and a length of 8 meters. Additional details regarding specific dimensions can be found in Figure 3-1.
- **Tilting Mechanism:** The flume can be tilted to replicate a wide range of slopes from  $0^\circ$  to  $16.5^\circ$ , to cover different flow conditions from subcritical to supercritical.
- **Recirculation System:** The flume utilizes a recirculating system composed of two separate circuits. One circuit continuously recirculates a sediment-water mixture, while the other circuit recirculates water only. Both circuits are equipped with a centrifugal pump that allows for adjustments to the flow rate, enabling control over the intensity of sediment transport within the flume.
- **Measuring Devices:** Included to perform different measurement. The devices that can be found are ultrasonic gauges, pressure sensors, flowmeter for mixtures, among others.

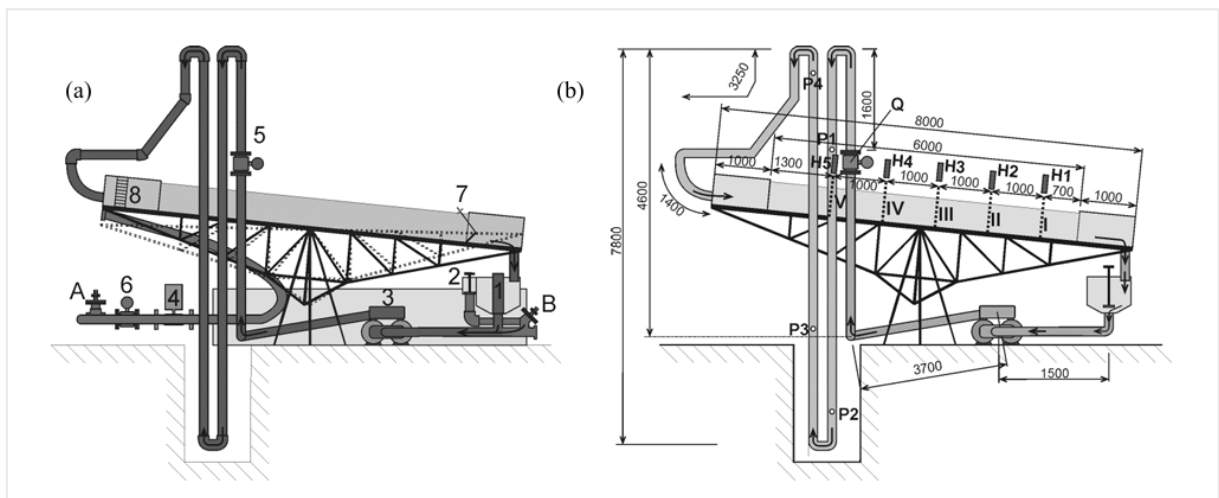


Figure 3-1. Layout with a recirculating flume. Supply and separation tank (1), overflow (2), sediment-water mixture pump (3), water pump (4), mixture and water flow meters (5 & 6), outlet weir (7), inlet distributors (8), control valve (A), inlet valve (B)) and a separate water recirculation circuit (flow meter (Q) for the mixture, pressure sensors (P) for concentration measurement, ultrasonic gauges (H) for water surface elevation, with distances in millimetres. Source: Matoušek-et-al [27].

This study utilizes a two-dimensional system inspired by the aforementioned flume. The system can be configured to accommodate one or two solid phases, depending on the simulation scenario (unimodal or bimodal). Regarding the solid phases, the particle characteristics emulated in the models presented in this thesis are based on those of FA30 and SUN25 particles, both described by Matoušek-et-al [25] in their previous work conducted at the same laboratory.



To facilitate a clear understanding of the model configuration details discussed in the following sub-chapter (focusing on Ansys setup), a summary of the input data for the system geometry and particle properties is presented in Table 3-1. It is important to note that some dimensional adjustments were made. Certain dimensions were reduced to optimize computational efficiency, while others were increased to allow for proper flow development within the system without significant volume loss (mostly the flume depth). This optimization process ensures a balance between capturing the essential flow characteristics and maintaining computational feasibility.

Table 3-1. Variables associated to the configuration of the system for the simulations.

| Variable Description         | Magnitude                 |
|------------------------------|---------------------------|
| Depth of the Flume           | 1.2 [m]                   |
| Length of the Flume          | 5.5 [m]                   |
| Density of Coarse Particles  | 1368 $\frac{[kg]}{[m^3]}$ |
| Density of Fine Particles    | 1280 $\frac{[kg]}{[m^3]}$ |
| Diameter of Coarse Particles | 0.00365 [m]               |
| Diameter of Fine Particles   | 0.0028 [m]                |

## 3.2 Introduction to Ansys Software

A relevant aspect to consider when using Ansys Fluent for any type of CFD model, is that the software works alongside other software to generate results. These pre-processing, post-processing and platform software tools perform specialized tasks that feed into the overall CFD simulation process and are as relevant as the actual numerical calculation of the model, mostly when the interpretation of the results takes place. We can view this process as a system with clearly defined roles for each software component.

- The **pre-processing software** prepares the geometry and defines the initial conditions for a CFD model, alongside the generation of a mesh. This is like setting up the blueprint and materials for a simulation. This category includes software like Ansys SpaceClaim and Ansys Meshing.
- The **calculation software**, Ansys Fluent, takes central role, performing the actual calculations that simulate fluid flow, heat transfer, or other relevant phenomena. It's the engine that analyses the system based on the provided conditions. This type of software corresponds to Ansys Fluent or Ansys Polyflow, for instance.
- The **post-processing software** takes the raw data from the calculation software and allows the user to visualize and analyse the results. This is like interpreting the data generated by the simulation to understand how the system behaves. An example of this would be Ansys CFD-Post.
- While not mandatory, Ansys Workbench is a highly recommended simulation **platform software**. It provides a highly intuitive graphical interface that simplifies organizing and connecting data across various models and their elements.

By working together, these software programs provide a comprehensive workflow for CFD simulations. Figure 3-2 illustrates this process in more detail, showing the specific functions of each software and how they interact. In this chapter, details about the processes of creation of geometry, meshing, configuration of the solver and treatment of results, are described in detail. Then, the software configuration workflow presented here describes a specific configuration developed according to the phenomena involved in this study. While many configurations of different variables exist beyond the ones treated here, they are not explored since they fall out of the scope of this thesis. Unaddressed options remain at their default settings.

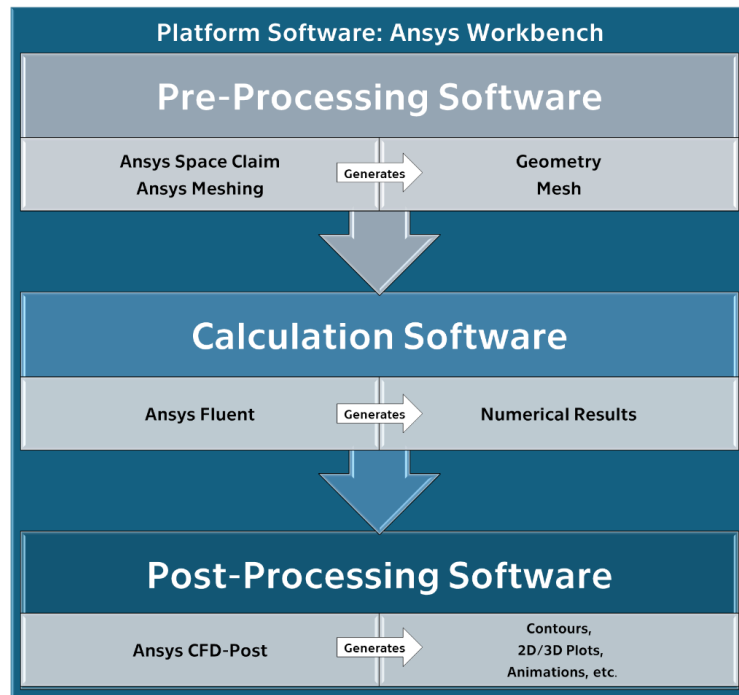


Figure 3-2. Workflow diagram for working with Ansys suite.

### 3.3 Platform Software: Ansys Workbench

Ansys Workbench is a platform software designed to streamline the simulation processes included in this thesis. It can be simply pictured as a central hub where the user can manage all the simulation data under one interface. Ansys Workbench does exactly that, allowing the user to import CAD geometry, connect them to a meshing activity, subsequently set up and run simulations, and finally analyse results, all within a graphical interface. This not only saves time by eliminating the need to switch between different programs, but also ensures seamless data transfer between various simulation types, leading to more accurate and efficient models and minimizing accidental mistakes that may lead to data loss.

Right after Ansys Workbench is executed, the default graphic interface will appear on the screen. On the left side, the software shows the components that can be added to the simulation under the name “Toolbox”, some of them containing complete simulation schemes (called “Analysis Systems”), including more than one single module (called “Component Systems”). The “Analysis Systems” are pre-configured workflows within Workbench that address specific simulation types, such as structural analysis, fluid flow analysis, or electromagnetic simulations. Each system comes with pre-defined steps like geometry definition, material properties, loads (forces, pressures, etc.), solving methods, and post-processing results handling. On the other hand, the “Component Systems” are more generic building blocks that offer functionalities like CAD geometry import, defining material properties, mesh generation, or results visualization. These elements can be seen in Figure 3-3.

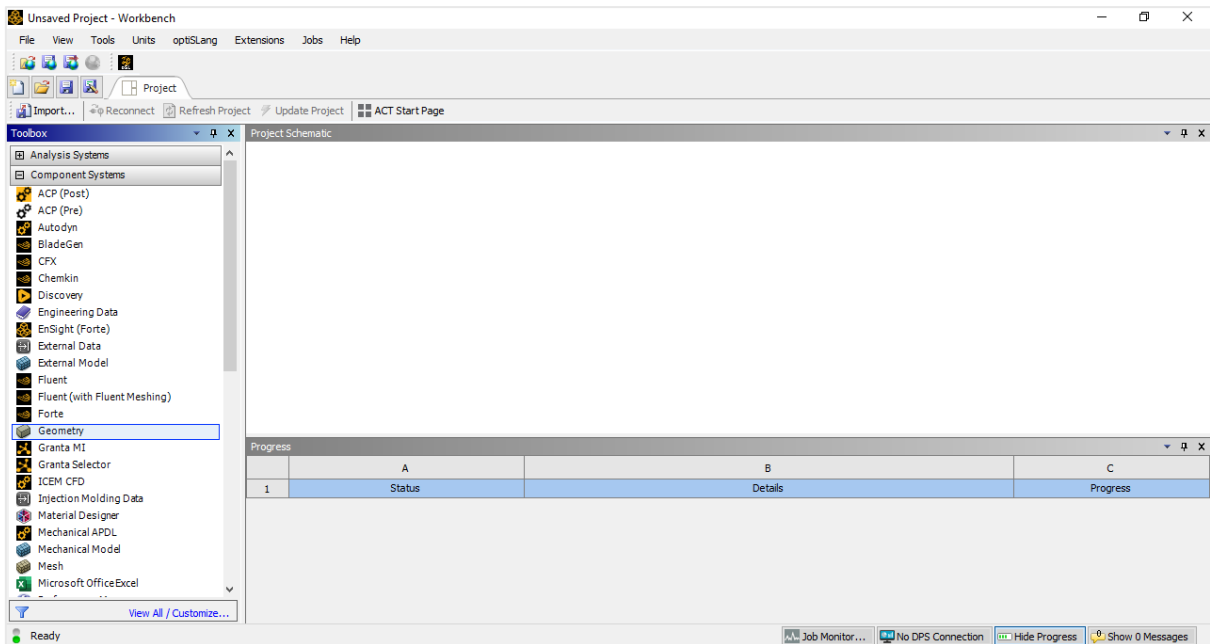


Figure 3-3. Blank interface of a new simulation project in Ansys Workbench.

For the models presented in this thesis, individual component systems were interconnected according to the nature of the workflow. The components included were “Geometry”, “Mesh”, “Fluent”, and “Results”, and as it can be seen in Figure 3-4, they were interconnected by simply dragging them from the left ribbon into the workspace. In the specific case shown in this figure, one sole geometry system serves as the origin for two different meshes, which subsequently lead to two different flow calculation systems in Ansys Fluent and their results.

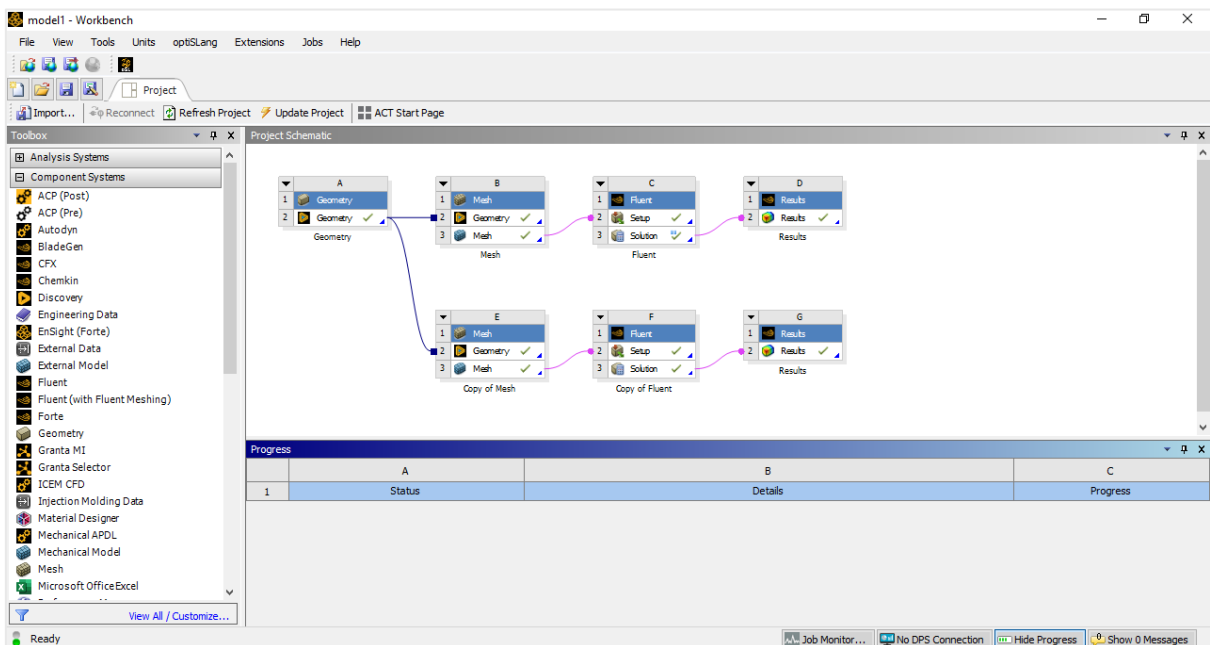


Figure 3-4. Interconnected simulations in Ansys Workbench.

One important consideration is that not all component systems can be connected to every target cell, since the compatibility is determined by the data type involved. Workbench highlights compatible drop zones in red for ease of use. As an example of this, in Figure 3-5 compatibility is possible for the drag-and-drop action of a CFX module (an alternative numerical

solver to Ansys Fluent) into an already created mesh. Also, it's worth mentioning that dragging a component system onto an empty space in the project schematic creates a standalone instance of that system.

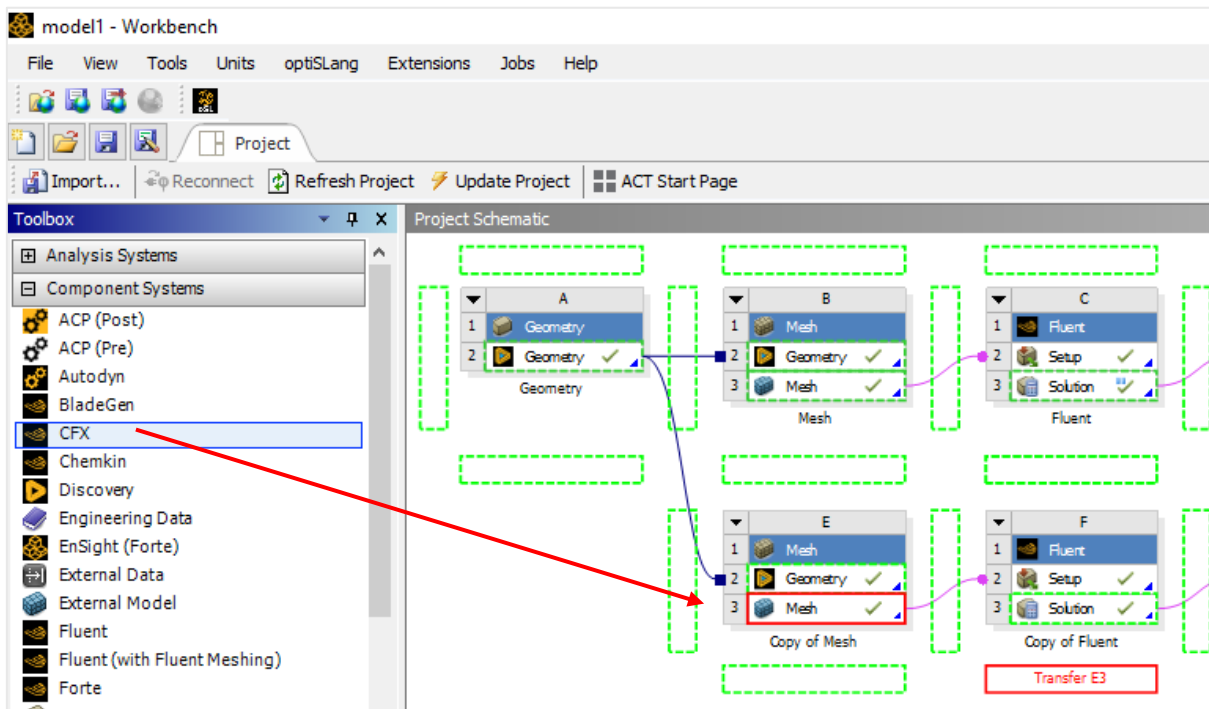


Figure 3-5. Drag-and-drop action of a CFX module into a Mesh module.

Finally, it's important to describe what the small icons next to the modules mean, since they provide valuable and quick information about the state of the simulation. A thunderbolt symbol signifies that the module is queued for execution, meaning its calculations are part of the analysis. A green checkmark shows to the user that the module has run successfully, and its outputs are ready for subsequent steps and connections to further compatible modules. A yellow exclamation mark indicates a potential issue, such as missing inputs or warnings that require attention in order to get the module executed correctly, thus, the user would want to double-check the module's settings and address any errors before proceeding. Finally, a red "X" symbol denotes a critical error that halts the simulation progress. Resolving this error within the module is essential before continuing with the analysis, since usually they simply cannot be executed further. By understanding these icons, it was possible to effectively monitor the simulations supported by Ansys Workbench.

To establish the initial geometry for our model, we utilized a single module within ANSYS Workbench, as shown in Figure 3-6. This process started by dragging a "Geometry" module onto a blank workspace in the project schematic. Subsequently, a right-click on the module revealed a context menu, where the "New SpaceClaim Geometry" option was elected to launch this dedicated geometry creation software.

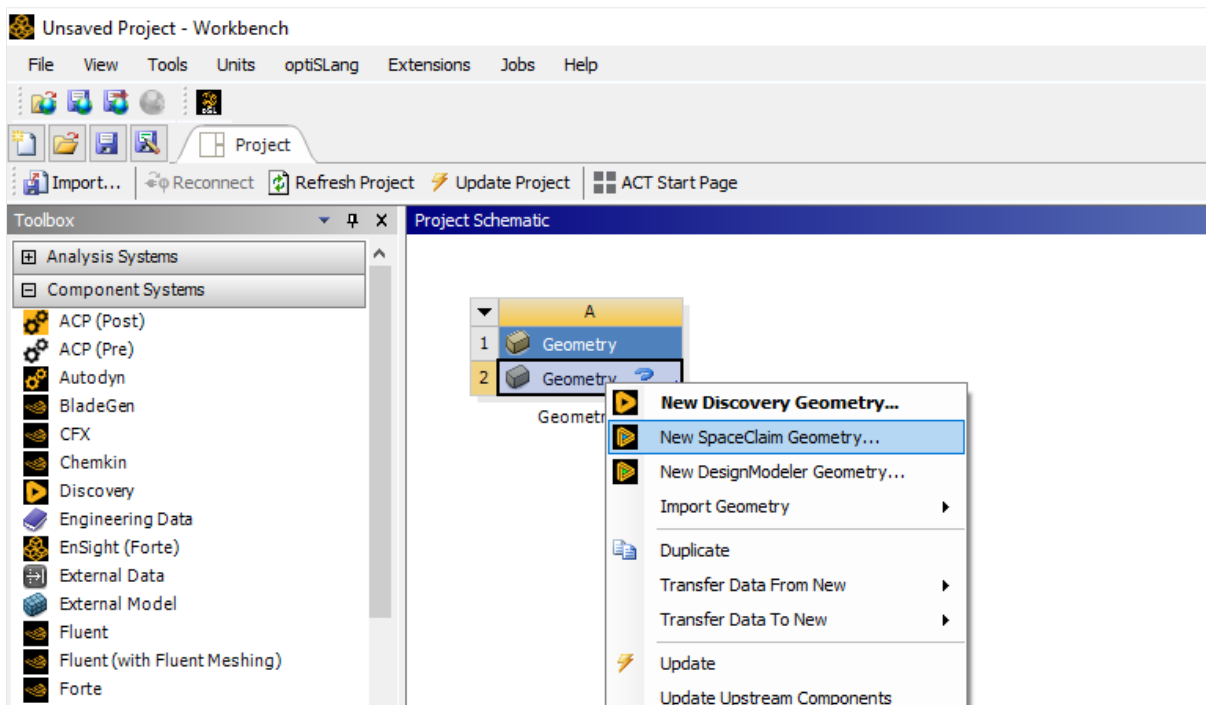


Figure 3-6. Geometry module creation in Ansys Workbench.

## 3.4 Pre-Processing Software

### 3.4.1 Ansys SpaceClaim Geometry

Ansys SpaceClaim is a user-friendly software within the Ansys suite for creating accurate and efficient geometries suited for Computational Fluid Dynamics (CFD) simulations in general. It outstands among the other geometry software options due to its intuitive functionality and native CAD capabilities. In the absence of a pre-existing CAD model, SpaceClaim provides the users with a comprehensive suite of modelling tools, which are enough to model non-complex geometric schemes like the ones used for open channels. Basic shapes like rectangles, circles, and extrusions serve as building blocks for constructing the channel geometry. Furthermore, advanced features like sweeps and blends enable the creation of more intricate channel configurations, including curved walls or uneven beds. In this chapter, the functions used for the purposes of this thesis are described.

Upon entering SpaceClaim, the first step was to define the sketch plane by clicking the button highlighted in red in Figure 3-7. Typically, the XY plane was selected as the most suitable canvas for a 2D channel representation. Next step consisted of the selection of the sketching tools to define the geometry of the channel, which depending on the case, can be done by using lines, rectangles, or even circles. These tools were together in the section “Create” in the upper ribbon, highlighted in green in Figure 3-6. We can also note that the “Rectangle” tool is being used in the same figure, allowing the user to accurately input the dimensions of the figure. For the models created for this thesis project, the dimensions of the channel were 1.2 meters of height and 5.2 of length.



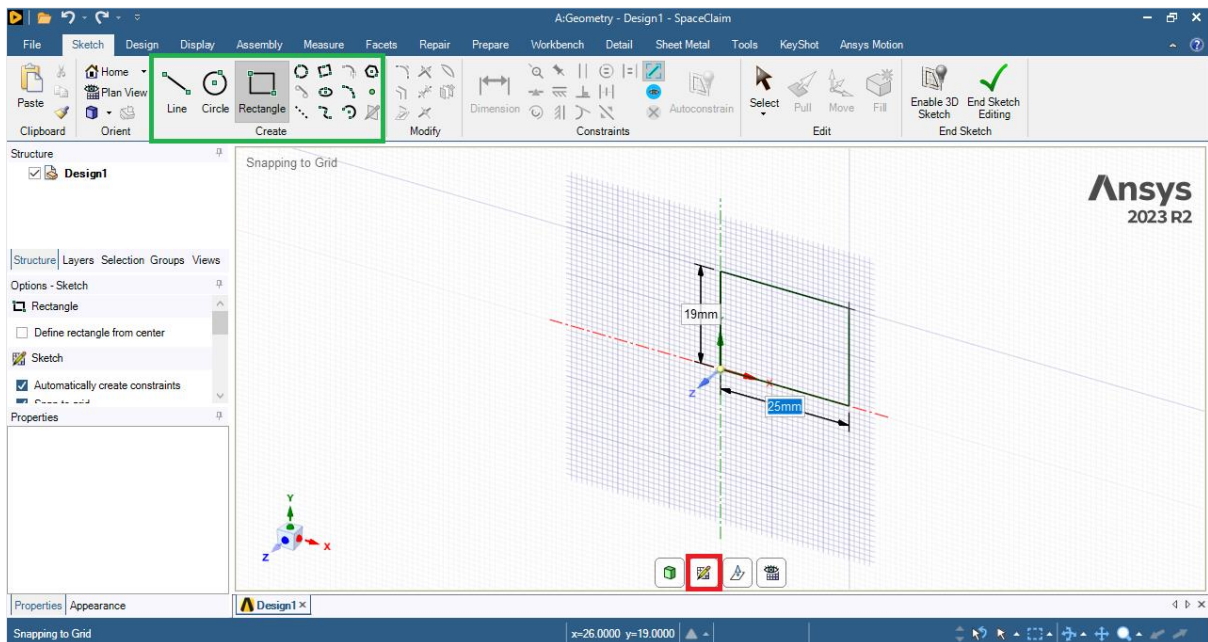


Figure 3-7. Plane selection for commencing the geometry sketch in Ansys SpaceClaim.

Following the creation of the main channel, additional geometrical elements were incorporated. As it is shown in Figure 3-8 (left side), an inlet is introduced on the lower-left portion of the channel. This inlet possesses a height of 0.24 meters and a length of 0.08 meters, positioned 0.1 meters above the channel bed. The "Rectangle" tool, previously used for the channel, facilitated the creation of this inlet with precise dimensions.

To integrate the inlet with the main channel structure, the "Trim Away" tool was used. Figure 3-8 (right side) illustrates this process, where the location of this tool is highlighted in orange. This tool allowed the targeted removal of lines, effectively creating the desired connection between the inlet and the channel geometry.

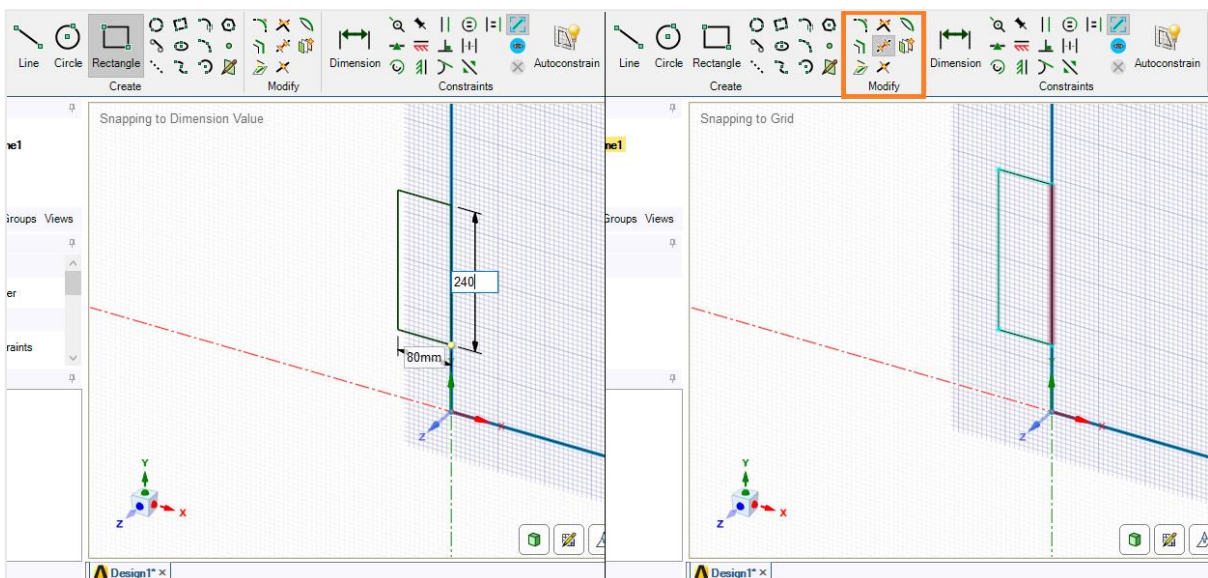


Figure 3-8. On the left side, the inlet of the channel is being set using the "Rectangle" tool. On the right side, the inlet is being connected to the channel using the "Trim Away" tool.

With the external boundaries of the channel established, the next step involved defining the fluid domain within the geometry. This distinction between fluid and solid regions was crucial

for accurate representation later in Ansys Meshing and Ansys Fluent. As it's shown in Figure 3-9, the "Select" tool (highlighted in purple) allowed the selection of the entire geometry, by enclosing it with the cursor. Once the desired region is highlighted, clicking the "Fill" button (highlighted in yellow) within the same figure completed the process. This action effectively created a closed surface that defined the fluid domain within the channel geometry for subsequent analysis in Ansys Meshing and Ansys Fluent.

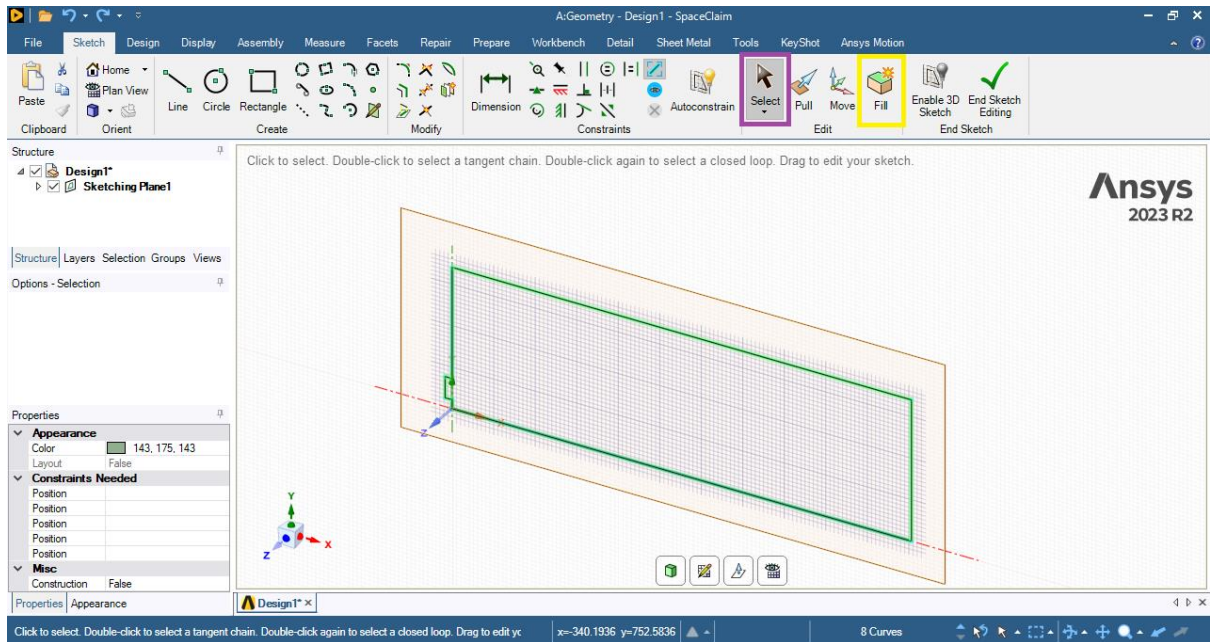


Figure 3-9. Definition of the inner region of the system using the "Convert" tool.

The final step in geometry definition involved creating a step on the right-most boundary, and the process is explained using Figure 3-10. This feature was specifically helpful for solid particle accumulation within the system. To achieve this, a switching to the "Design" tab (highlighted in light blue) on the upper ribbon was performed, then, in the "Intersect" section, the "Split" tool (highlighted in brown) was selected. The button highlighted in orange on the upper-left corner of the geometry window needs to be activated to ensure that the modifications are applied to the boundary and not to the interior of the geometry. Finally, the desired height of the step, which is 0.1 meters in this case, was defined using the value displayed in the centre of Figure 3-10. This step creation completed the geometric definition for our CFD simulation. It's worth noting that the rest of the right-most boundary will serve as the main outlet for the flow.

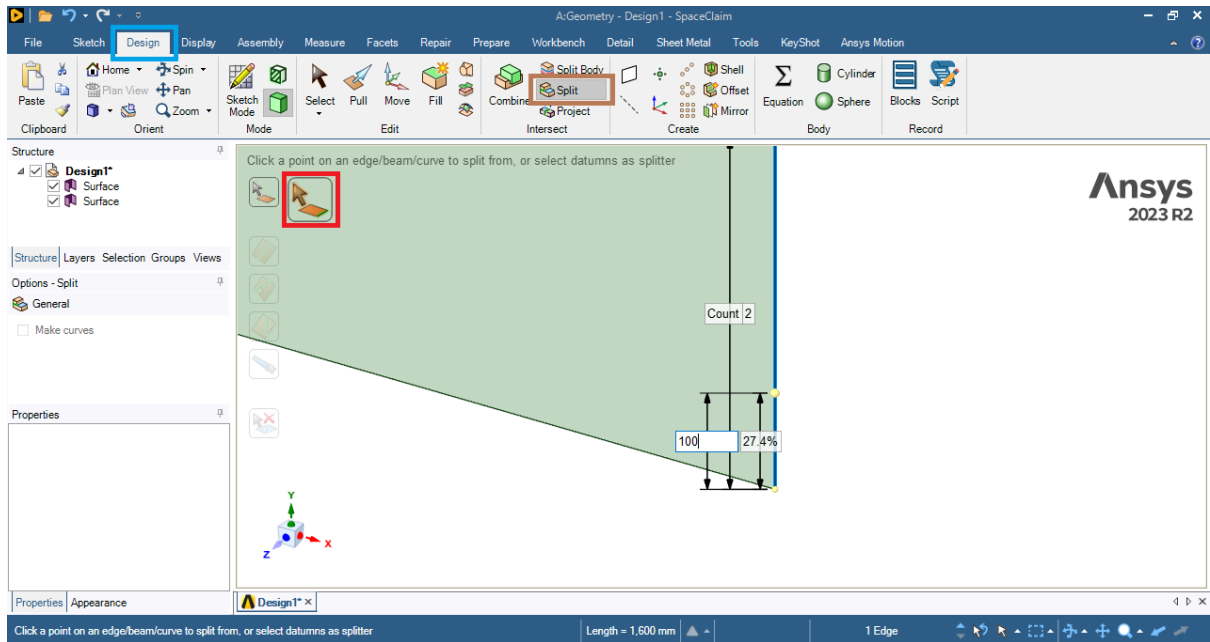


Figure 3-10. Right-most step creation in the geometry.

### 3.4.2 Ansys Meshing

Having established an accurate geometry for the model, the next crucial step involved mesh generation. Meshing essentially discretizes the computational domain into a network of small elements (cells for 3D, faces for 2D) upon which the governing equations of fluid flow will be solved in Ansys Fluent.

The quality of the mesh significantly impacts the accuracy and efficiency of any CFD simulation, that's why, Ansys Meshing offers a comprehensive suite of tools to create high-quality meshes focused on the specific demands of the different systems that the Ansys suite can handle. In the following section, the steps followed to complete the mesh generation within Ansys Meshing are described, taking as a base the geometry created in Ansys SpaceClaim in the previous steps.

The first step compromised going back to Ansys Workbench and drag a "Mesh" module over the "Geometry" module, which was already created. Subsequently, the contextual menu of the "Mesh" module was displayed by right-clicking on it, and then the "Edit" option was selected in order to open Ansys Meshing. This process is portrayed in Figure 3-11.



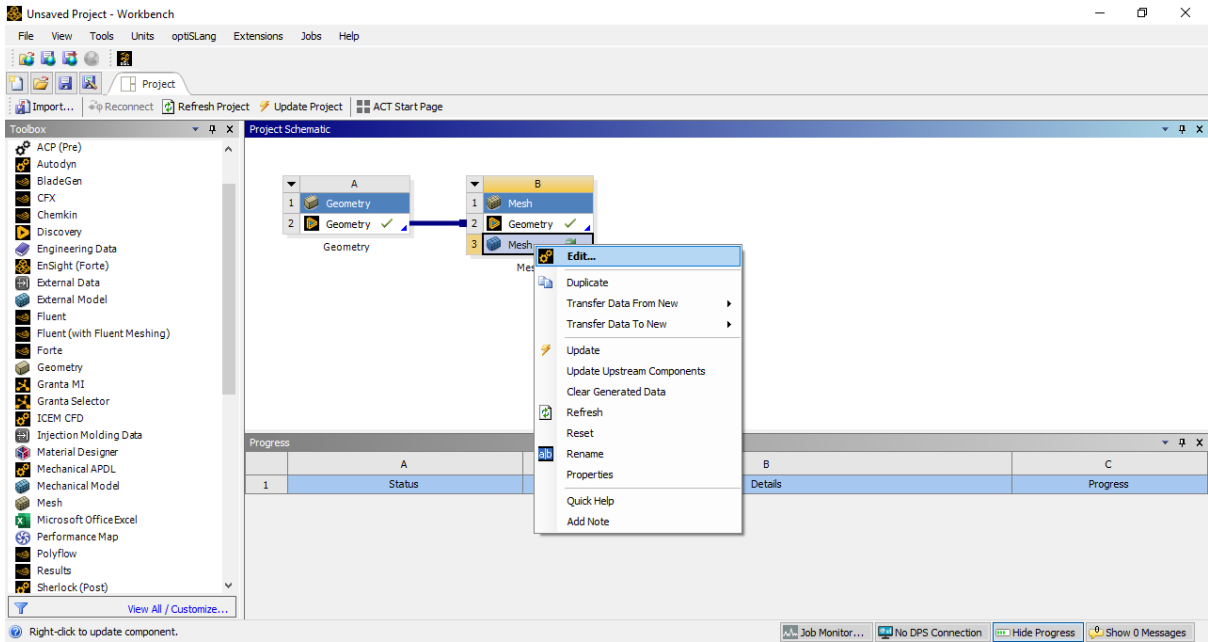


Figure 3-11. "Mesh" module inserted and connected to "Geometry" module.

The initial screen that Ansys Meshing shows corresponds to the one shown in Figure 3-12. Here, it was very useful to change the view so a planar view of the geometry of the channel was shown, which in this case was the XY plane. This was done by clicking the Z axis in the bottom right corner (Highlighted in red). Subsequently, the definition of the mesh characteristics was performed by clicking the "Mesh" section available under the "Project" list on the left (highlighted in green). Below this area, and by displaying the "Default" list, the mesh type was set to an Ansys Fluent compatible format, with an element size of 4 millimetres (section highlighted in yellow).

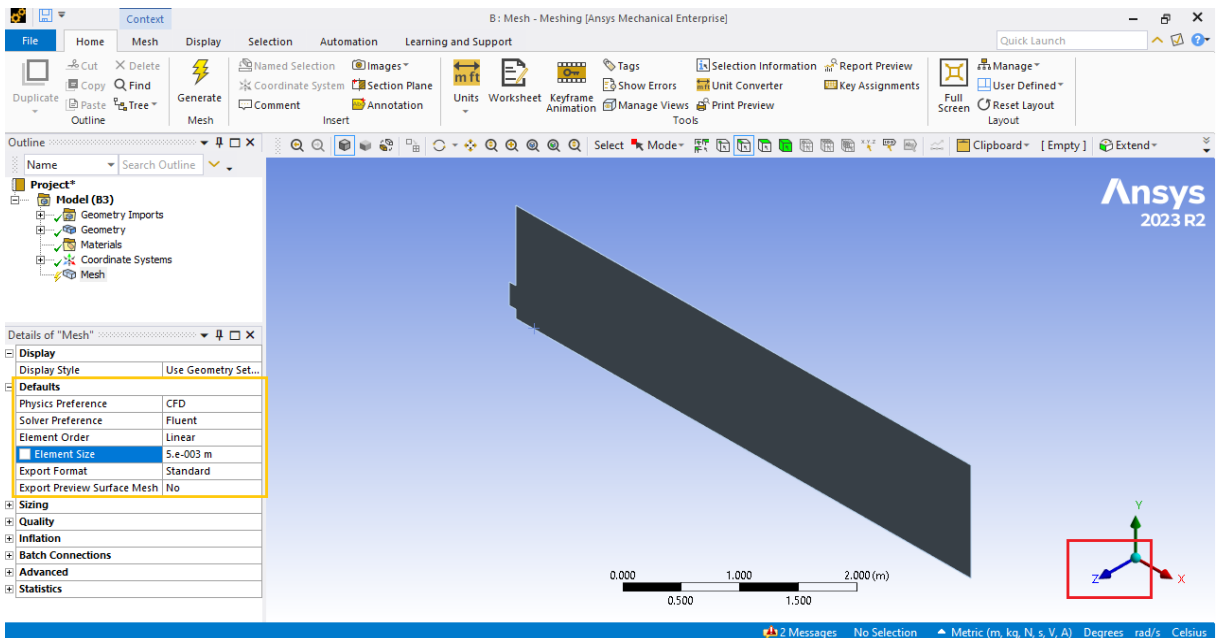


Figure 3-12. Definition of the general characteristics of the mesh.

A critical step in mesh generation involves refining the mesh in areas where boundary layer phenomena are expected to occur. This is particularly important near walls with roughness, as the boundary layer significantly influences overall flow behaviour. Figure 3-13 illustrates the mesh refinement process.

To start, the context menu was accessed by right-clicking on the existing "Mesh" item within the "Project" section (highlighted in green in Figure 3-12). From the menu, "Insert" followed by "Refinement" options were selected. This action created a new item named "Refinement" within the "Project" list. Clicking on this newly created item allowed to configure the refinement details. Under the "Scope" list, the "Geometry" option (highlighted in blue in Figure 3-13) is chosen. Next, the line selection mode was activated by clicking the button highlighted in red. This was done in order to target specific lines within the geometry for mesh refinement. While holding the "CTRL" key, multiple lines corresponding to the walls with roughness are then selected. Clicking the "Apply" button confirms the refinement configuration (highlighted in brown), ensuring a finer mesh resolution in these crucial boundary layer regions. Finally, the refinement level was set to 3 in the "Definition" box below.

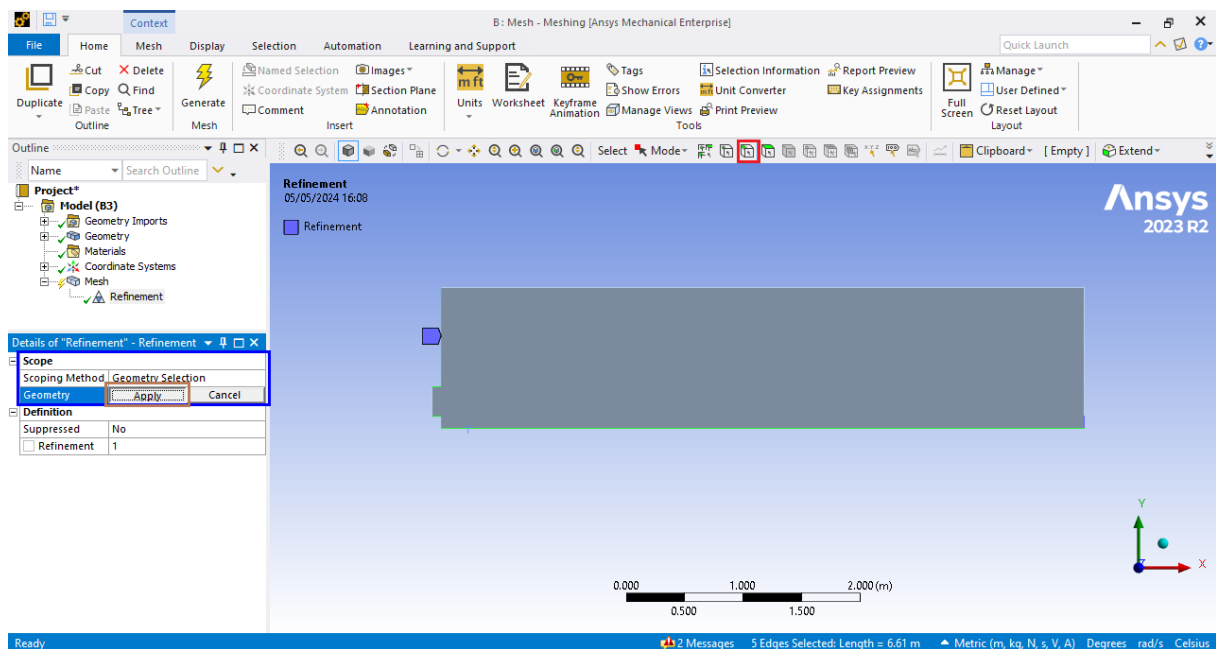






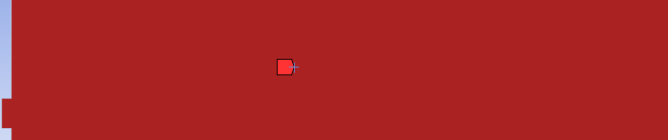


Figure 3-13. Refinement definition for the mesh creation.

Subsequently, the relevant elements on the system were named using the "Named Selection" tool, which is done for Ansys Fluent to recognize these elements as either boundary conditions, or the zone where the fluids interact. Using the same button highlighted in red in Figure 3-13, the selection of the zone using the "CTRL" button was done, then, in the contextual menu the "Create Named Selection" option was chosen. The detail about the naming of the zones is shown in Table 3-2<sup>2</sup>.

<sup>2</sup> This table only refers to the geometric localization of the boundaries, the physical characteristics definition of the boundary conditions can be seen in the "Calculation Software: Ansys Fluent" subchapter.

Table 3-2. Name and description of the "Named Zones" in Ansys Meshing.

| Selection Location  | Name        | Description   |
|---|-------------|---|
|    | walls-inlet | Represents then walls of the upstream zone of the channel, including the ones in the inlet structure. |
|    | inlet-down  | Represents the inlet of the mixture of water, air, and particles.                                     |
|    | bottom      | Represents the bottom of the channel.   |
|    | step        | Represents the small structure defined to accumulate particles over the bottom of the channel.        |
|   | outlet      | Represents the main outlet for the flow, at the right-most side of the channel.                       |
|  | top         | Represents the limit of the system on the top.  |
|  | fluid       | Represents the zones where the flow and the interactions between the phases occur.                    |

Finally, the "Generate" button located on the upper ribbon of the software was clicked to start the meshing process, and the final state after the meshing was successfully created is shown in the Figure 3-14.

## 3.5 Calculation Software: Ansys Fluent

### 3.5.1 Fluent Launcher and Initial Interface

Having established a well-defined geometry and a high-quality mesh, the next step was to configure Ansys Fluent for it to process the different selected scenarios according to the theoretical principles described in Chapter 2. This chapter aims to describe this configuration process.

The simulation process began by dragging a "Fluent" module from the Toolbox and connecting it to the existing "Mesh" module within the project schematic. This connection ensured the pre-generated mesh was readily available for the Fluent simulation. Subsequently, a right-click on the "Fluent" module revealed a context menu. Within this menu, the "Edit" option was selected. This action launched ANSYS Fluent and automatically loaded the information from the connected "Mesh" module, effectively initializing the setup process with the necessary mesh data. Figure 3-14 presents the state of Ansys Workbench up to this point.

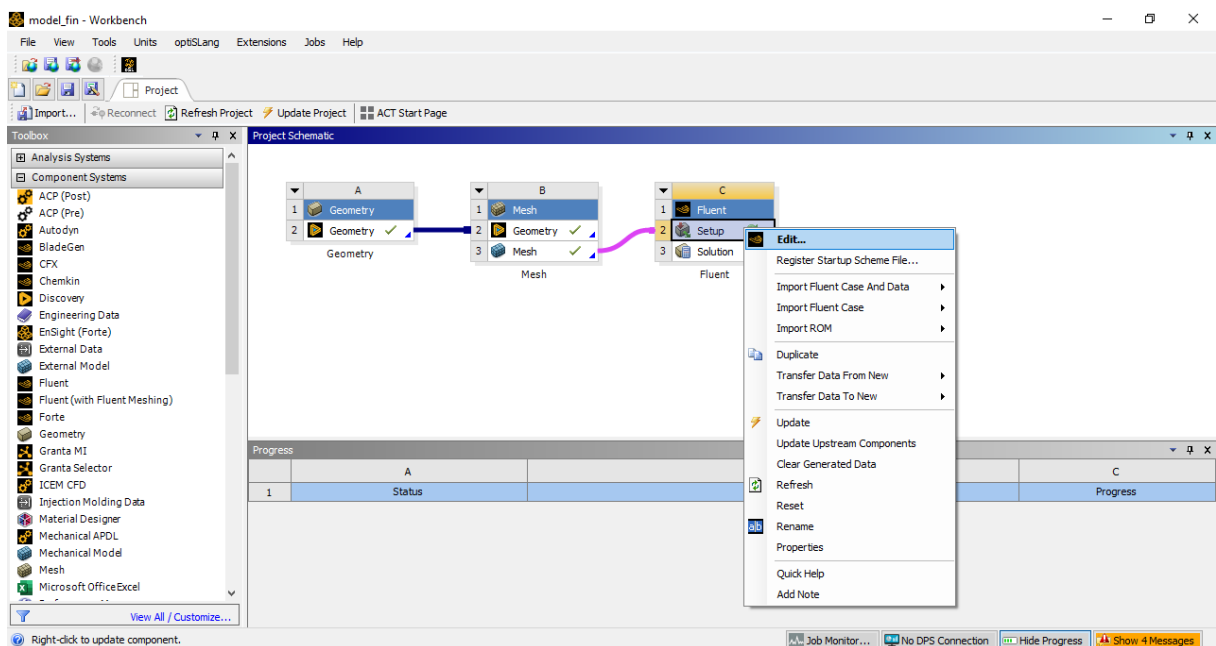


Figure 3-14. Ansys Workbench scheme, with Ansys Fluent module ready to be configured.

When Ansys Fluent is launched, a dialog box appears before the main interface, which serves as an entrance configuration point for the software (shown in Figure 3-15). This dialog is named "Fluent Launcher", and here, two important settings were defined: The "Double Precision" calculation checkbox, and the "Parallel (Local Machine)" core count. Since the simulation includes a multiphase flow, the "Double Precision" option was activated. Subsequently, four cores were assigned to work in parallel, which was set according to the characteristics of the computer used for the simulations<sup>3</sup>.

<sup>3</sup> See Appendix A.

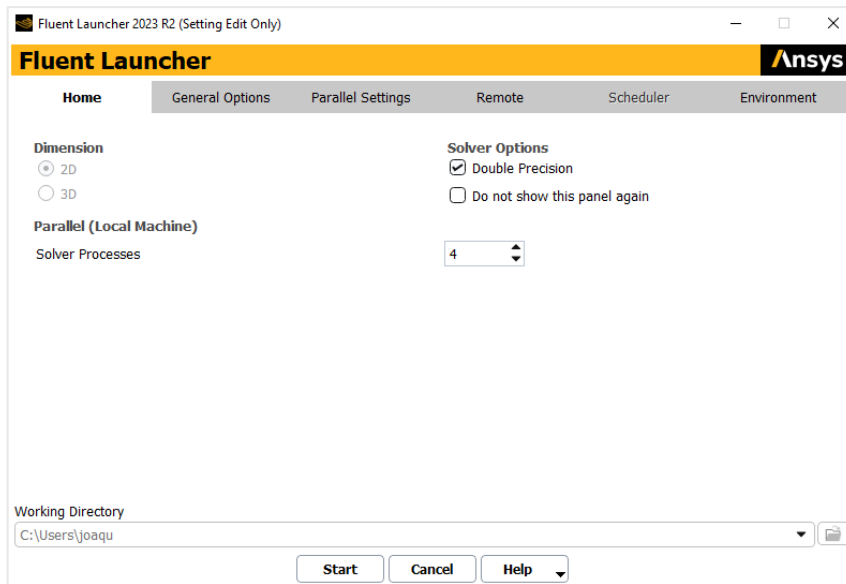


Figure 3-15. Fluent Launcher dialog box.

Upon clicking the "Start" button in the launcher, the Ansys Fluent interface appeared, as it is shown in Figure 3-16. This interface can be divided into two main areas that are constantly used for setting up a model: the "Outline View" (highlighted in red) and the "Task Page" (highlighted in blue). These two sections work together. Clicking on an item in the "Outline View" list brings up more specific settings for that item in the "Task Page". The "Task Page" may also contain buttons or sections that open new windows with even more detailed options. In addition to these two areas, there is a ribbon at the top of the interface (highlighted in green) that provides access to many of the same options, along with some additional ones. Finally, there is a visualizer (highlighted in purple) that is used to show graphical elements. This explanation provides a simplified overview of how to configure models in Ansys Fluent.

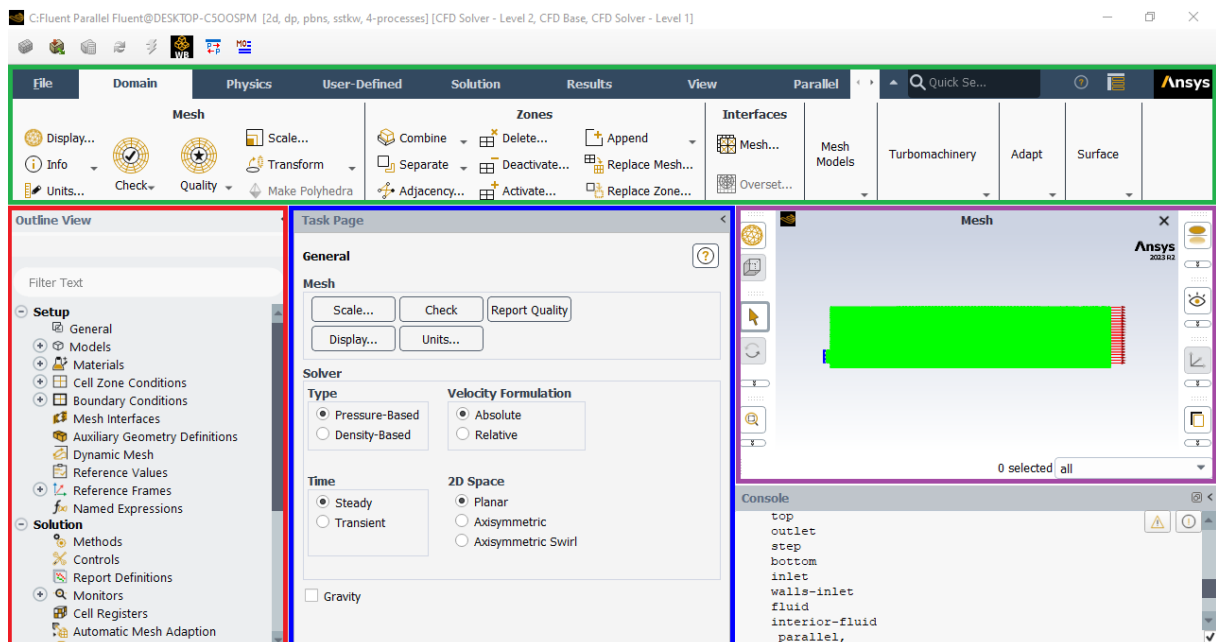


Figure 3-16. Initial interface of Ansys Fluent.

### 3.5.2 General Configuration

The configuration process began with the "General" item within the "Outline View." While mesh settings are typically configurable within this section, they were bypassed since the whole mesh information originated from Ansys Meshing and SpaceClaim, and it was directly imported into Ansys Fluent. Following this, the focus shifted to configuring the numerical solver. The specific options chosen for the solver are detailed in Table 3-3. It is noteworthy that with the exception of the gravity vector components, all other settings remained the same across the different modelled scenarios. This approach of modifying only the gravity vector components based on channel inclination  $\phi$  [deg] (a simpler method compared to altering the entire geometry and mesh) was employed for efficiency.

Table 3-3. Settings of "General" item in Ansys Fluent.

| Option                     | Description of the Set-up  |
|----------------------------|--|
| Type                       | Pressure-Based   |
| Velocity Formulation       | Absolute   |
| Time                       | Transient  |
| 2D Space                   | Planar   |
| Gravity (check box)        | On   |
| Gravitational Acceleration | X: $9.81 \sin(\phi) \left[ \frac{m}{s^2} \right]$ Y: $-9.81 \sin(\phi) \left[ \frac{m}{s^2} \right]$ |

### 3.5.3 Materials Configuration

This section details the process of defining the physical characteristics for materials representing the various flow phases. Double-clicking the "Materials" item within the "Outline View" revealed a list of materials categorized as "Fluid" and "Solid" on the "Task Page". By default, only "air" was pre-created. Subsequently, additional materials for water and particles (solids) were established. It is important to note that only "Fluid" category materials were created, as these can be associated with phases when employing the Eulerian model.

Upon double-clicking the "Fluid" item on the "Task Page", a "Create/Edit Materials" window appeared (see Figure 3-17, left side). This window provided access to the Ansys Fluent materials database. By clicking the corresponding button, a new window displayed a list of "Fluent Fluid Materials", from which "water-liquid" was selected and copied (see Figure 3-7, right side). This process successfully added regular water as a material for use in subsequent configuration steps.

An analogous process was then followed to add the "silicon-solid" element from the database. This material possessed a pre-defined silicon configuration, necessitating the modification of certain properties. This was achieved by double-clicking the "silicon-solid" element on the "Task Page". The name was then edited to either "particle," "particle-coarse," or "particle-fine" depending on the specific scenario. Most importantly, the density was also adjusted accordingly (refer to Table 3-4 for a detailed breakdown of these cases).

Table 3-4. Density set-up in "Materials" sections.

| Material Name                     | Density                              |
|-----------------------------------|--------------------------------------|
| <b>Single Size Granular Phase</b> |                                      |
| particle                          | $1368 \left[ \frac{kg}{m^3} \right]$ |
| <b>Double Size Granular Phase</b> |                                      |
| particle-coarse                   | $1368 \left[ \frac{kg}{m^3} \right]$ |
| particle-fine                     | $1280 \left[ \frac{kg}{m^3} \right]$ |

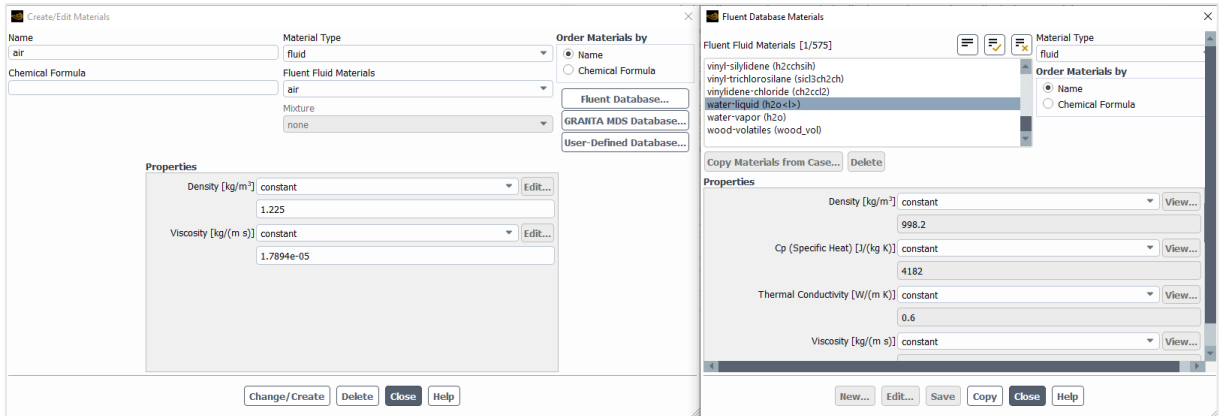


Figure 3-17. On the left side, the "Create/Edit" window. On the right side, the Ansys Fluent material database.

### 3.5.4 Model Configuration

This section focuses on defining the characteristics of the multiphase flow, including the turbulence model. The process began with selecting the "Models" item within the "Outline View", which opened the "Task Page" with a new list of options. By double-clicking the "Multiphase" item, a window titled "Multiphase Model" appeared. This window, illustrated in Figure 3-17, featured four tabs along the top.

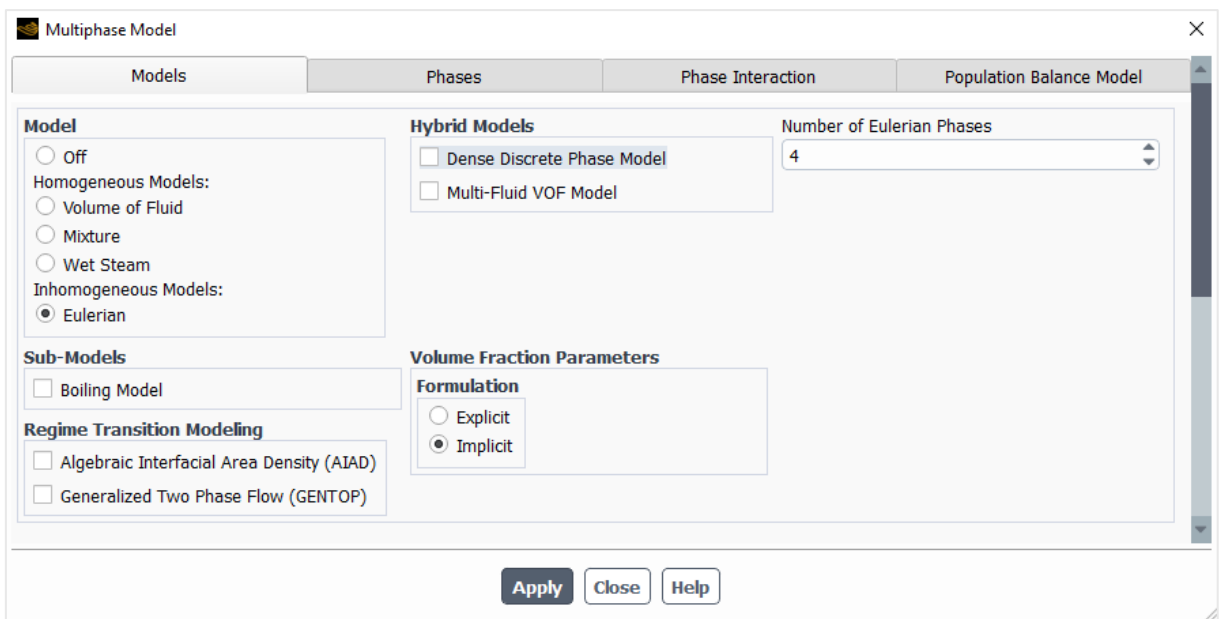


Figure 3-18. Multiphase Model window in Ansys Fluent model configuration.

Configuration changes were implemented in all tabs except for "Population Balance Model" and Tables 3-4 and 3-5 summarizes the specific settings chosen for both the unimodal and bimodal cases within this section. Any variables not explicitly addressed were left with their default values or options, and the configuration expressed in Table 3-5 the common configuration for all the simulations.

Table 3-5. Phase setup for unimodal and bimodal flows in Ansys Fluent.

| Tab                 | Variable/Option   | Value/Action         |                      |
|---------------------|---|----------------------|----------------------|
|                     |   | Unimodal             | Bimodal              |
| Models              | Inhomogeneous Model – Eulerian                                    | Checkbox Selection   |                      |
|                     | Number of Eulerian Phases   | 3                    | 4                    |
| Phases              | Phases – Primary Phase (phase-1) – Phase Setup – Name.            | water                |                      |
|                     | Phases – Primary Phase – Phase Setup – Phase Material             | water-liquid         |                      |
|                     | Phases – Secondary Phase (phase-2) – Phase Setup – Name           | air                  |                      |
|                     | Phases – Secondary Phase (phase-2) – Phase Material               | air                  |                      |
|                     | Phases – Secondary Phase (phase-3) – Phase Setup – Name           | particle             | particle-coarse      |
|                     | Phases – Secondary Phase (phase-3) – Phase Setup – Phase Material | particle             | particle-coarse      |
|                     | Phase Setup – Granular  | Checkbox Selection   |                      |
|                     | Phase Setup – Diameter  | Constant/0.00365 [m] | Constant/0.00365 [m] |
|                     | Granular Properties   | Table 3-5            |                      |
|                     | Phases – Secondary Phase (phase-4) – Phase Setup – Name           | Not used             | particle-fine        |
|                     | Phases – Secondary Phase (phase-4) – Phase Setup – Phase Material | Not used             | particle-fine        |
|                     | Phase Setup – Granular  | Checkbox Selection   |                      |
|                     | Phase Setup – Diameter  | Not used             | Constant/0.0028      |
| Granular Properties | Table 3-5   |                      |                      |

Table 3-6. Common configuration for "Granular Properties" in Ansys Fluent.

| Granular Property   | Model         |
|---|---------------|
| Granular Viscosity $\left[\frac{kg}{m \cdot s}\right]$      | Gidaspow      |
| Granular Bulk Viscosity $\left[\frac{kg}{m \cdot s}\right]$ | Lun-et-al     |
| Solid Pressure [Pa]   | Ma-Ahmandi    |
| Granular Temperature $\left[\frac{m^2}{s^2}\right]$         | Algebraic     |
| Frictional Viscosity $\left[\frac{kg}{m \cdot s}\right]$    | Schaeffer     |
| Frictional Pressure [Pa]                                    | Based-ktgf    |
| Friction Packing Limit                                      | Constant/0.61 |
| Angle of Internal Friction [deg]                            | 30            |
| Packing Limit   | Constant/0.65 |
| Radial Distribution   | Ma-Ahmadi     |
| Frictional Modulus [Pa]                                     | Derived       |
| Elasticity Modulus [Pa]                                     | Derived       |

Subsequently, the configuration process shifted to the "Phase Interaction" tab. This section holds significant importance as the available options can significantly impact both the accuracy and computational performance of the simulations. A critical aspect of this process involved minimizing simulation complexity by selecting the simplest models for interactions not central to the study's focus. An example of this is the turbulence dispersion model for the air-water interaction, which was disabled since it made the model unnecessarily complex, i.e. the interest is not on the details of the bubbly flow layer over the liquid-gas interface. Table 3-6 provides a detailed breakdown of the specific interaction models chosen for each relevant phenomenon within the multiphase flow, specifically for the bimodal granular flow. It's worth mentioning that some variables were not included in the model (set as "none" option in the configuration window). Alongside the more complex configuration for the bimodal flow scenario, Table 3-7



summarizes the setup for a unimodal flow scenario., which follows the same scheme as it can be noticed.

Table 3-7. Phase interaction model setup for the bimodal granular flow scenarios.

| Phase Interaction                 |                               | Variable                         | Model Option     |
|-----------------------------------|-------------------------------|----------------------------------|------------------|
| Water – Air                       |                               | Drag Coefficient                 | Schiller-Naumann |
|                                   |                               | Modification of Drag Coefficient | None             |
|                                   |                               | Lift Coefficient                 | None             |
|                                   |                               | Turbulent Dispersion             | None             |
|                                   |                               | Turbulence Interaction           | None             |
|                                   |                               | Virtual Mass Coefficient         | None             |
|                                   |                               | Surface Tension Coefficient      | Constant: 0.073  |
| Water – Coarse Particle           | Water – Fine Particle         | Drag Coefficient                 | Gidaspow         |
|                                   |                               | Modification of Drag Coefficient | None             |
|                                   |                               | Lift Coefficient                 | Moraga           |
|                                   |                               | Turbulent Dispersion             | Simonin          |
|                                   |                               | Turbulence Interaction           | None             |
|                                   |                               | Virtual Mass Coefficient         | None             |
| Air – Coarse Particle             | Air – Fine Particle           | Drag Coefficient                 | Gidaspow         |
|                                   |                               | Modification of Drag Coefficient | None             |
|                                   |                               | Surface Tension Coefficient      | None             |
| Coarse Particle – Coarse Particle | Fine Particle – Fine Particle | Restitution Coefficient          | 0.8              |
| Coarse Particle – Fine Particle   |                               | Drag Coefficient                 | Schiller-Naumann |
|                                   |                               | Modification of Drag Coefficient | None             |
|                                   |                               | Restitution Coefficient          | 0.8              |
|                                   |                               | Surface Tension Coefficient      | None             |

Table 3-8. Phase interaction model setup for the unimodal granular flow scenarios.

| Phase Interaction   |  | Variable                         | Model Option     |
|---------------------|--|----------------------------------|------------------|
| Water – Air         |  | Drag Coefficient                 | Schiller-Naumann |
|                     |  | Modification of Drag Coefficient | None             |
|                     |  | Lift Coefficient                 | None             |
|                     |  | Turbulent Dispersion             | None             |
|                     |  | Turbulence Interaction           | None             |
|                     |  | Virtual Mass Coefficient         | None             |
|                     |  | Surface Tension Coefficient      | Constant: 0.073  |
| Water – Particle    |  | Drag Coefficient                 | Gidaspow         |
|                     |  | Modification of Drag Coefficient | None             |
|                     |  | Lift Coefficient                 | Moraga           |
|                     |  | Turbulent Dispersion             | Simonin          |
|                     |  | Turbulence Interaction           | None             |
|                     |  | Virtual Mass Coefficient         | None             |
| Air – Particle      |  | Drag Coefficient                 | Gidaspow         |
|                     |  | Modification of Drag Coefficient | None             |
|                     |  | Surface Tension Coefficient      | None             |
| Particle – Particle |  | Restitution Coefficient          | 0.8              |

The next step was to configure the turbulence model. This selection aimed to achieve an optimal balance between accuracy and computational efficiency, and as it's outlined in the theoretical framework section, the chosen model corresponds to the SST k- $\omega$  model applied in "Mixture" mode. The configuration process was performed as it follows: First, clicking on the "Viscous" element within the "Outline View" section triggered the display of a window presenting turbulence model options. Since the default options aligned perfectly with the model

selection, a dedicated table summarizing these settings is not included. However, Figure 3-18 visually illustrates the "Viscous Model" window where this configuration was performed. The simplicity of the window reflects the straightforward nature of this setup process.

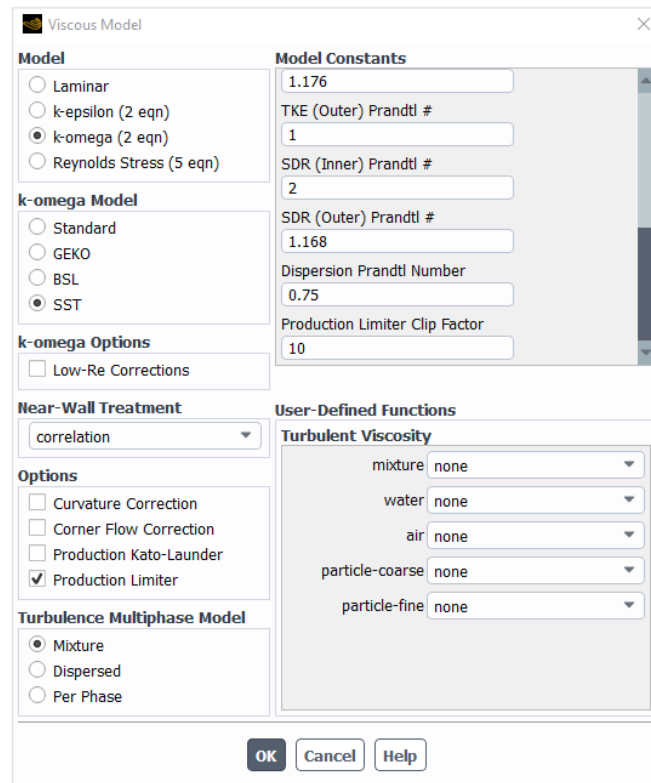


Figure 3-19. Viscous model configuration windows in Ansys Fluent.

### 3.5.5 Boundary Conditions Configuration

The boundary conditions for the system were established in accordance with the "Named Selections" previously defined in Ansys Meshing (refer to Table 3-1 for details), and this process involved a series of steps within Ansys Fluent. First, selecting the "Boundary Conditions" item within the "Outline View" populated the "Task Page" with a list of the previously defined "Named Selections". Following this, the configuration of boundary conditions for solid rough walls was performed. These walls included the "bottom" item, representing the rough channel bed; the "walls-inlet" item, representing the rough wall in the left-most zone of the channel including the inlet structure; and the "step" representing the small vertical rough wall section at the right-most zone of the channel as described previously. To configure each individual case, a double-click was performed on the corresponding item in the "Task Page" list. This action triggered the display of a configuration window (illustrated in Figure 3-20). The input box for "Roughness Height", highlighted in red within the figure, was used to specify a roughness height of 15 micrometres for all the aforementioned walls. Analogously, for the solid phases, and specular coefficient of 0.451 [4] was selected to model the interaction with the rough walls of the system. This was done by changing the "Phase" section to the solid phase(s) (highlighted in green in Figure 3-20).

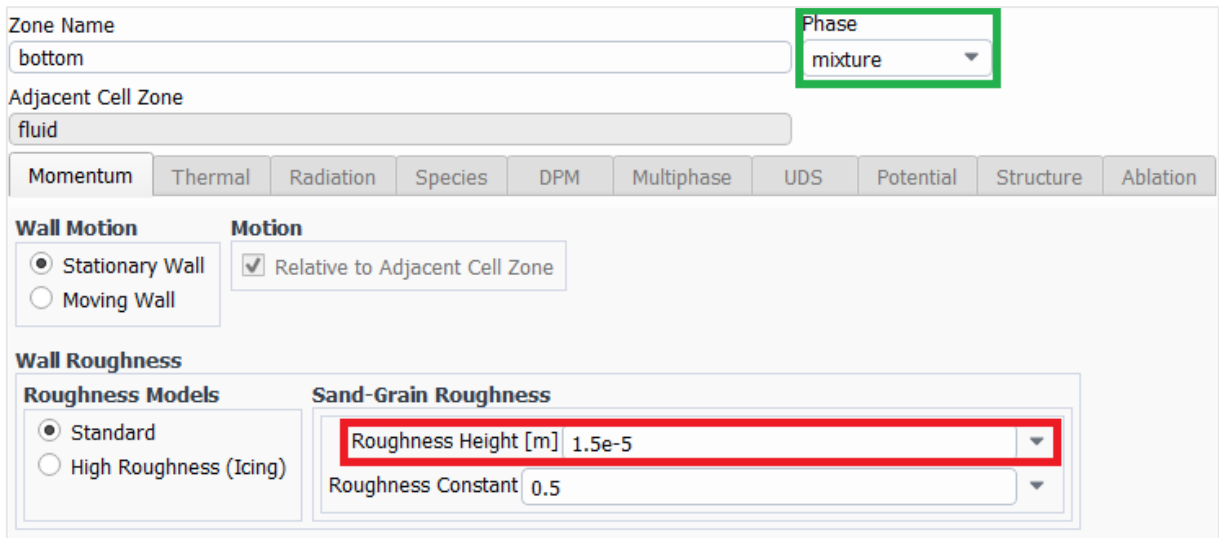


Figure 3-20. Wall boundary conditions setup in Ansys Fluent.

Following the definition of solid wall boundary conditions, the process shifted to configuring outlets representing the system's points of contact with atmospheric pressure. These outlets corresponded to two entries within the "Task Page" list: "top" representing the system's upper outlet to the atmosphere, and "outlet" representing the downstream outlet to the atmosphere.

To configure these outlets, the corresponding item in the "Task Page" list was first selected with a single click. Next, if not already selected, the "pressure-outlet" option was chosen from the "Type" contextual menu located at the bottom of the "Task Page". A double-click on the selected item then triggered the display of a configuration window, and the configuration was set according to what's illustrated in Figure 3-21.

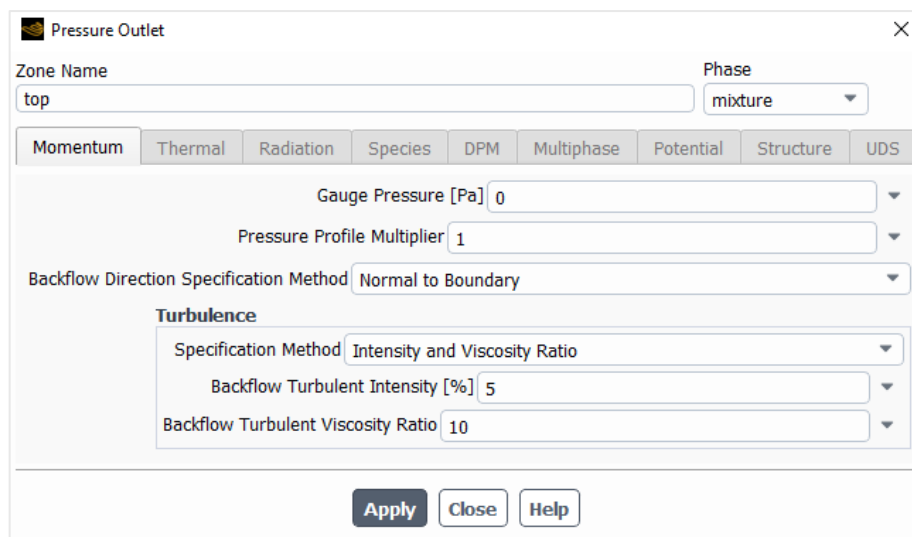


Figure 3-21. Pressure Outlet type of boundary condition setup in Ansys Fluent.

It is important to note that Ansys Fluent, by default, defines any backflow occurring in these outlets as consisting entirely of the primary phase (water, in the context of this study). This behaviour can be modified, however, to specify air as the main element flowing back into the system through these outlets. The process for defining air as the backflow element is illustrated in Figure 3-22, where first the "air" phase was selected in the upper-right corner of the window, and then the "Backflow Volume Fraction" was set to 0.9. The interpretation of this value can be thought as that 90% of the backflow needed by the system when performing calculations will

be composed of air, and the remaining 10% will be water which in turn represents the moisture of the atmospheric air.

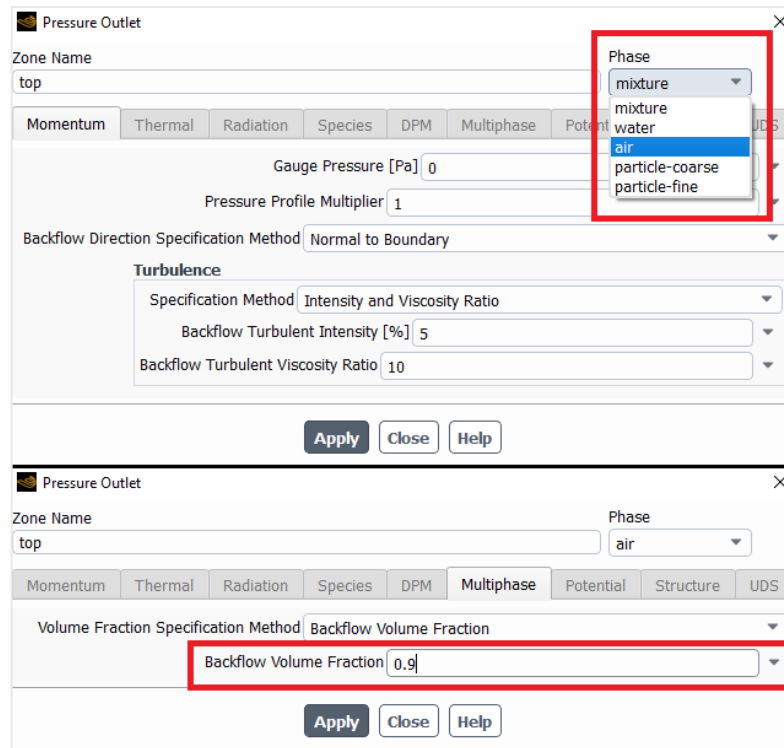


Figure 3-22. Backflow flow from outlet configuration in Ansys Fluent.

The inlet boundary condition, the only one varying across the simulation scenarios, defined the volume fraction and velocity at which different phases entered the system through the inlet structure. This configuration process involved a series of steps.

First, a single click on the "inlet" item verified that the "Type" contextual menu displayed the "velocity-inlet" option in the "Task Page", which should be the default selection when the named selection was designated as "inlet" during Ansys Meshing. A subsequent double-click on the same item triggered the display of the configuration window. By default, this window presented the configuration applicable to phases as a "mixture," reflecting the default selection in the "Phase" contextual menu. No modifications were made here.

The next step involved performing the configuration for individual phases. This was achieved by selecting the desired phase from the "Phase" contextual menu, where the available options included "mixture" (the initial default), the primary phase ("water" in this study), the first secondary phase ("air" in this study) and depending on whether the model was unimodal or bimodal, one or two additional granular phases ("particle" for unimodal, "particle-coarse" and "particle-fine" for bimodal). Selecting a secondary phase transformed the configuration window, as illustrated in the upper portion of Figure 3-23 (for the "momentum" tab) and the lower portion of Figure 3-23 (for the "Volume Fraction" tab). These options provided input options for defining the fraction of the entering mixture occupied by each phase and their respective velocities (highlighted in green). The absence of a volume fraction input for the primary phase reflects its role as the remaining fraction not occupied by other phases. Table 3-9 summarizes the specific configurations employed for the various scenarios modelled in this thesis.

Table 3-9. Inlet boundary condition setup in Ansys Fluent.

| Case               | Flume Bed Inclination ( $\phi$ ) | Water Phase     |                | Air Phase       |                | Particle Phase N°1 (Coarse) |                | Particle Phase N°2 (Fine) |                |
|--------------------|----------------------------------|-----------------|----------------|-----------------|----------------|-----------------------------|----------------|---------------------------|----------------|
|                    |                                  | Volume Fraction | Velocity [m/s] | Volume Fraction | Velocity [m/s] | Volume Fraction             | Velocity [m/s] | Volume Fraction           | Velocity [m/s] |
| Water-Only         | 0.5°                             | 1               | 1              | 0               | 0              | Not Used                    | Not Used       | Not Used                  | Not Used       |
| Unimodal Scenario  | 0.5°                             | 0.65            | 1              | 0.05            | 1              | 0.3                         | 1              | Not Used                  | Not Used       |
| Bimodal Scenario 1 | 0.5°                             | 0.65            | 1              | 0.05            | 1              | 0.15                        | 1              | 0.15                      | 1              |
| Bimodal Scenario 2 | 0.5°                             | 0.65            | 2              | 0.05            | 2              | 0.15                        | 2              | 0.15                      | 2              |
| Bimodal Scenario 3 | 1°                               | 0.65            | 1              | 0.05            | 1              | 0.15                        | 1              | 0.15                      | 1              |
| Bimodal Scenario 4 | 1°                               | 0.65            | 2              | 0.05            | 2              | 0.15                        | 2              | 0.15                      | 2              |

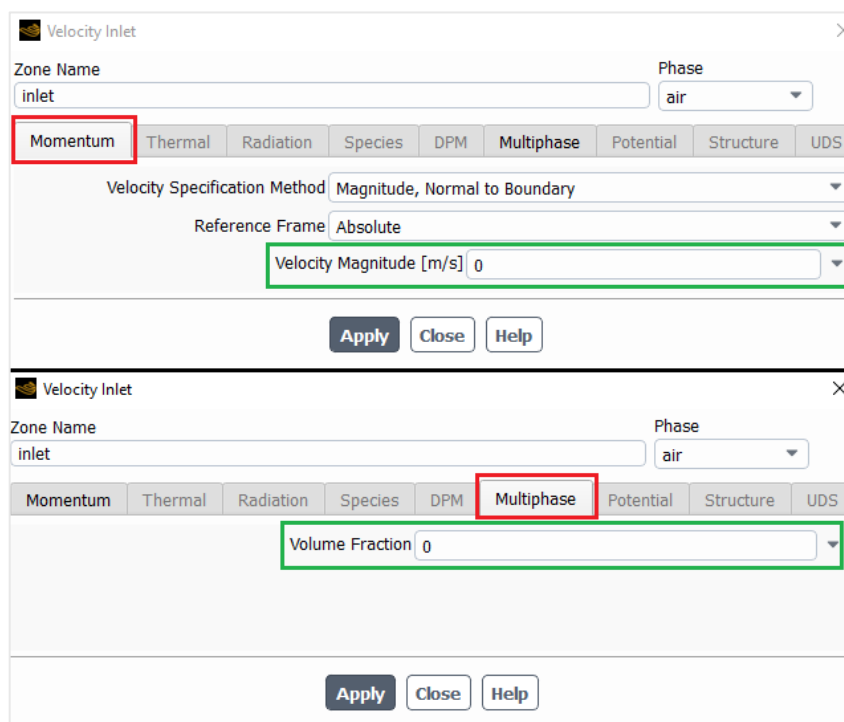


Figure 3-23. Inlet boundary condition window setup in Ansys Fluent.

### 3.5.6 Numerical Solver Configuration

This section details the configuration of discretization methods and initial conditions for the calculations. Additionally, it describes the calculation monitoring procedures employed through the creation of selected animated graphs.

The process commenced with a double-click on the "Methods" item within the "Outline View" section. This action populated the "Task Page" with a list of numerical techniques used to address the coupling of pressure and velocity variables, as well as the spatial discretization procedures for gradients, pressure, momentum, turbulent kinetic energy, and the specific dissipation rate. The displayed default configuration reflected Ansys Fluent's suggestions

based on the setup as it was done and described in the previous sections, and in most cases, proved suitable for the modelled scenarios. It is noteworthy, however, that the discretization schemes for solving pressure and momentum were occasionally suggested to be performed with the PRESTO! and QUICK methods, respectively. While these methods offer higher accuracy levels in some cases, they were ultimately replaced with "Second Order" for pressure and "First Order Upwind" for momentum to keep the computational cost according to the available hardware. Following these adjustments, the configuration for each case resembled Figure 3-24.

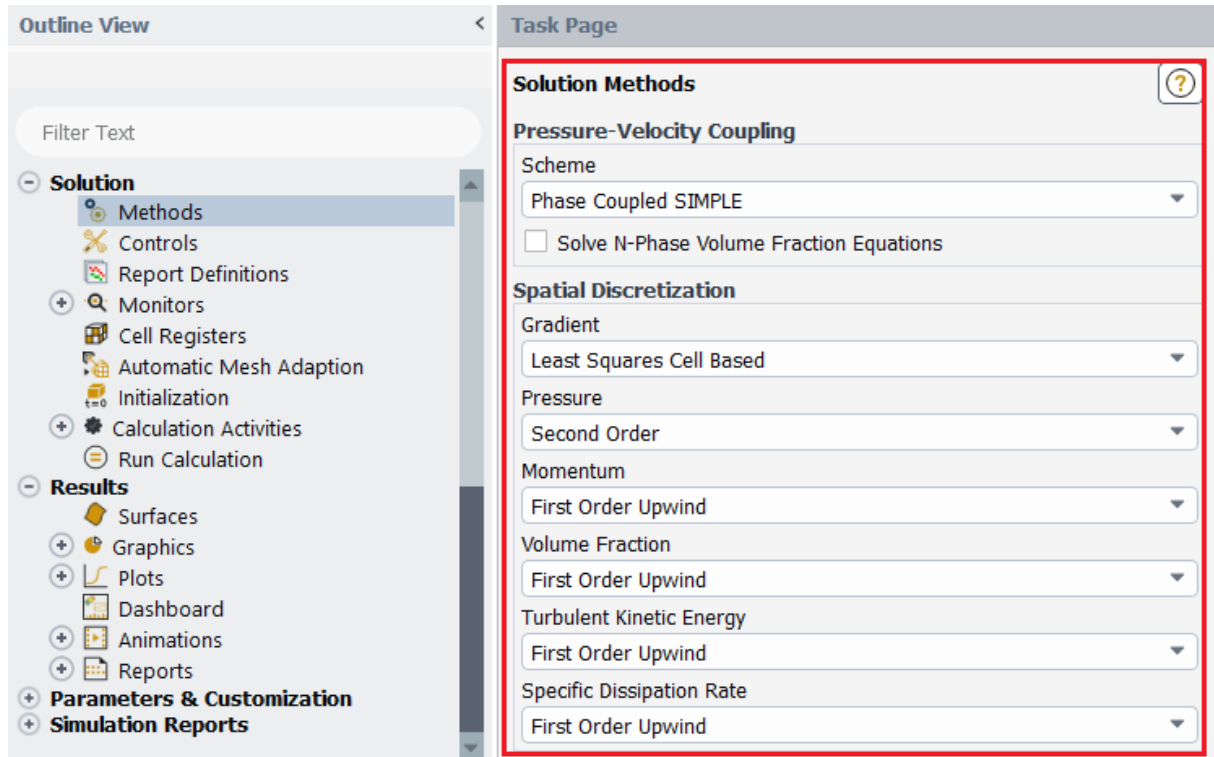


Figure 3-24. Coupling and spatial discretization methods setup in Ansys Fluent.

Following the definition of discretization methods, attention turned to establishing the initial conditions for the simulations. An inaccurate initial guess can lead to solution non-convergence, typically at the beginning of the calculation process, so the capability of easily setting up a case is crucial for success. To manage this risk, the "Initialization" item within the "Outline View" section was utilized. This section governs the initial state of the simulation, serving as the starting point for calculating subsequent time steps within mesh cells.

Before setting up the initialization state of the system, the "Cell Registers" item within the "Outline View" list provided a tool for marking specific areas of the system. These designated sections could then be used to assign values for different variables like volume fraction or velocities. To initiate the definition of these sections, a left click was performed on the "Cell Registers" icon. From the resulting contextual menu, the "New" and then "Region" options were selected. This action displayed a window titled "Region Register" (as illustrated in Figure 3-25).

Within the "Name" box in this window, the designation "region\_water" (highlighted in red) was assigned. This name reflects the intended purpose of the region, which is to designate a zone primarily containing water. In all cases, this region encompassed half of the channel, as depicted by the green highlighted area in Figure 3-25. Same procedure was followed to assign the remaining area of the system to a zone named "region\_air".

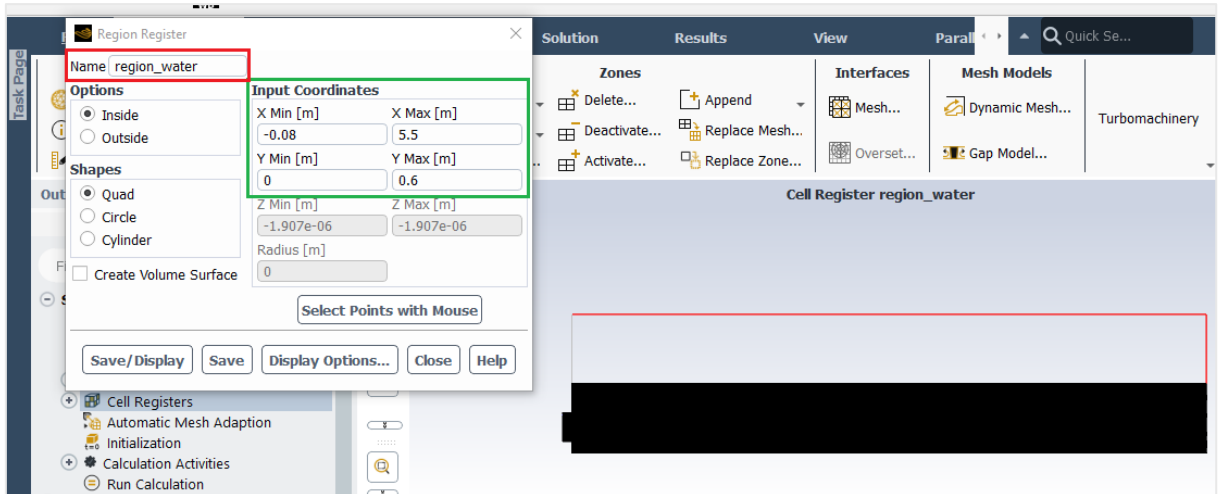


Figure 3-25. Cell registers setup process in Ansys Fluent.

For the water-only and the unimodal flow cases, the water cell register was equal in depth with the air cell register. (Water: 0 to 0.6 [m]; Air: 0.6 to 1.2 [m]). On the other hand, the bimodal cases cell registers had a special configuration (Water: 0 to 0.35 [m]; Air: 0.35 to 1.2 [m]).

Following the definition of cell registers, the next step involved continuing with the configuration the initial state for the flow calculations. This process was initiated by double-clicking the "Initialization" item within the "Outline View" section. This action populated the "Task Page" area with various options, as illustrated in Figure 3-26. Within the "Task Page," the initialization mode was chosen to be "Standard Initialization", which was the default selection (highlighted in red). Next, in the "Compute From" section (highlighted in blue), the "all-zones" option was selected from the drop-down menu. This option instructs Ansys Fluent to initialize the flow field using computed average values across all boundary zones, consequently, the software would compute and update the initial values based on the conditions defined at all boundary zones.

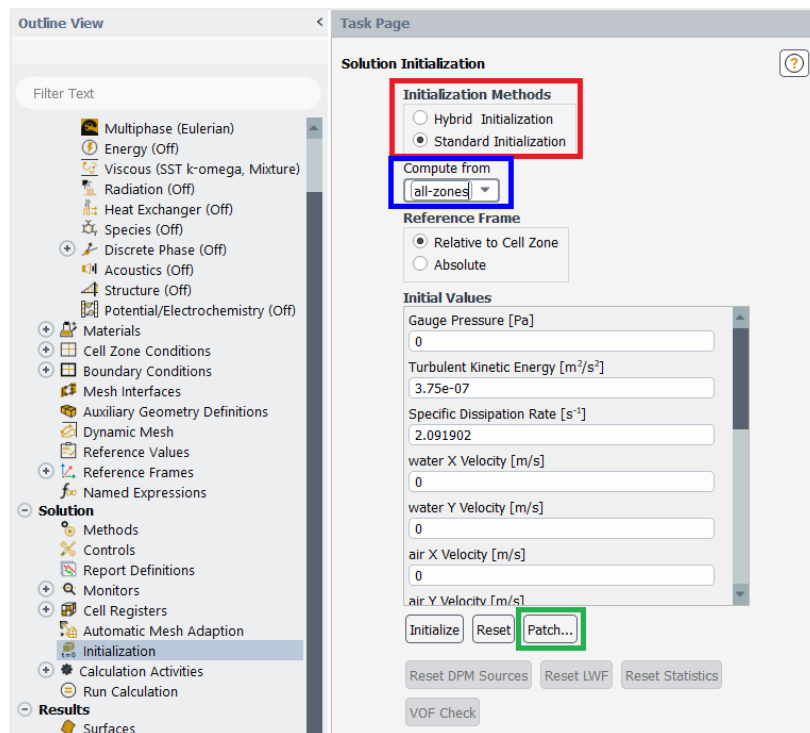


Figure 3-26. Initialization configuration in Ansys Fluent.

Following the creation of an initial condition for the entire system using the "all-zones" option, further modifications were implemented to refine this state. This refinement process utilized the "Patch" button (highlighted in green in Figure 3-26), which triggered the display of a window titled "Patch" (illustrated in Figure 3-27). Within this window, adjustments were made to the volume fractions of the phases in the initial state. The objective of these adjustments was to generate a system that was initially filled with a specific mixture in the lower half, consisting of 85% water, 10% particles, and a small amount of air (5%). In the upper half, the goal was to eliminate particles and reduce the water content to 10%, thus simulating realistic moist air conditions.

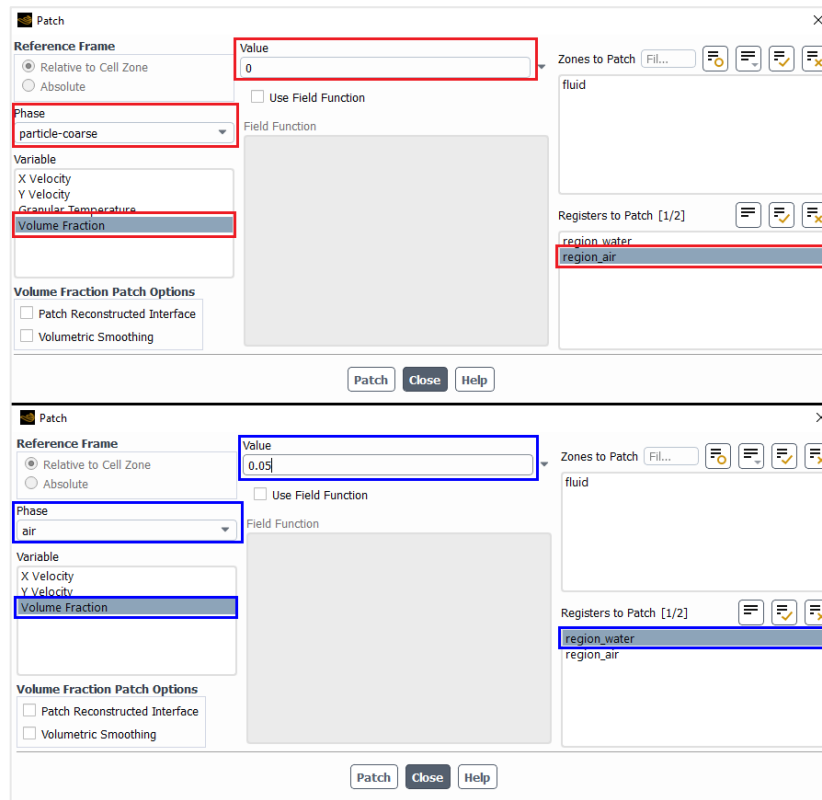


Figure 3-27. Patch configuration of the initial condition in Ansys Fluent.

In Figure 3-27, the upper portion of the figure showcases the configuration of the "particle-coarse" phase volume fraction to 0 within the previously defined "region\_air". Conversely, the lower portion shows the setting of the "air" phase volume fraction to 0.05 within the previously created "region\_water". This process of modifying volume fractions was repeated for each simulation scenario, considering the same pre-defined values and target zones. It is important to note that a distinction was made for unimodal and bimodal systems. In unimodal cases, the volume fraction of the only granular phase ("particle") was set to 0.1. For bimodal systems, the total 0.1 volume fraction was distributed equally between the "particle-coarse" and "particle-



fine" phases, resulting in 0.05 for each. A schematic representation of the treated initial condition for the system after these configurations is provided in Figure 3-28.

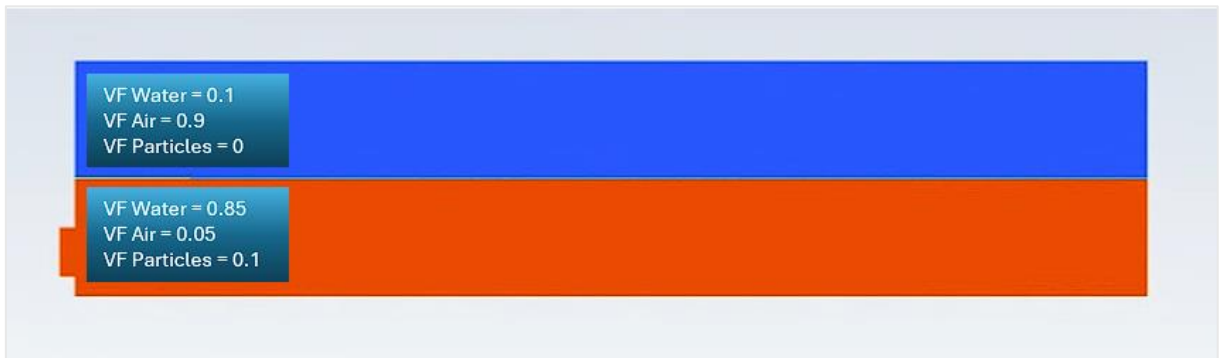


Figure 3-28. Generic scheme of the patched initial conditions of the system in Ansys Fluent.

Following the patching process, attention shifted towards defining the configuration for the "Calculation Activities" item within the "Outline View" list. Expanding this option using the "+" symbol on its left side revealed multiple sub-items, several of which required configuration.

The initial sub-item, "Autosave", was double-clicked, displaying a small configuration window (illustrated in Figure 3-29). This window allowed for defining the frequency at which Ansys Fluent would save calculated variables. The optimal selection for this setting depends on the specific context, user preference, and the complexity of the CFD model being performed, and additionally, the storage requirements of the generated data files must be considered, as they can occupy significant hard drive space. For the purposes of this thesis and considering the actual computational limits, a save interval of 0.5 seconds was chosen. The selection of variables to be saved was achieved by clicking the "Data File Quantities" button, which presented a list of all possible variables for saving. In all cases, all available variables were chosen for inclusion in the saved data.

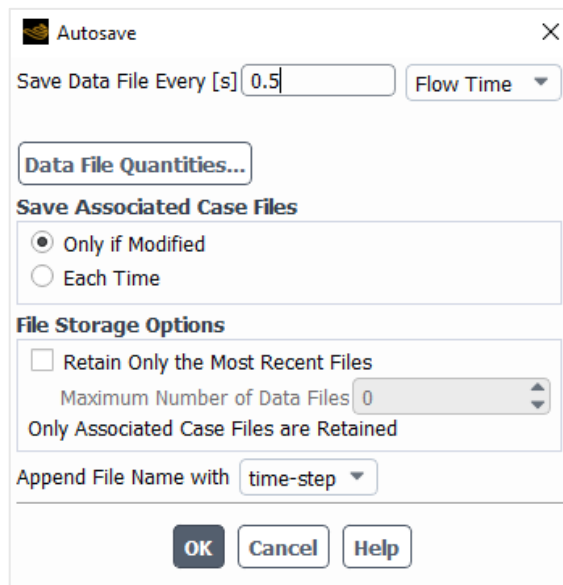


Figure 3-29. Autosave configuration in Ansys Fluent.

The final configuration step involved defining time discretization options within the "Run Calculation" item of the "Outline View" which was accessed through a double-click. The configuration for this section varied depending on whether the model scenario represented a unimodal or bimodal flow, and within the "Task Page" only two parameters were modified to

achieve the desired total flow time for the simulation (See Figure 3-30). For all of the simulation scenarios, targeting a total flow time of 2 minutes, the time step size was set to 0.1 seconds and the number of time steps was set to 1200. It is important to note that the time step size is a critical factor for some models used in the simulations. While a smaller time step generally leads to improved accuracy, it also significantly impacts the overall simulation runtime.

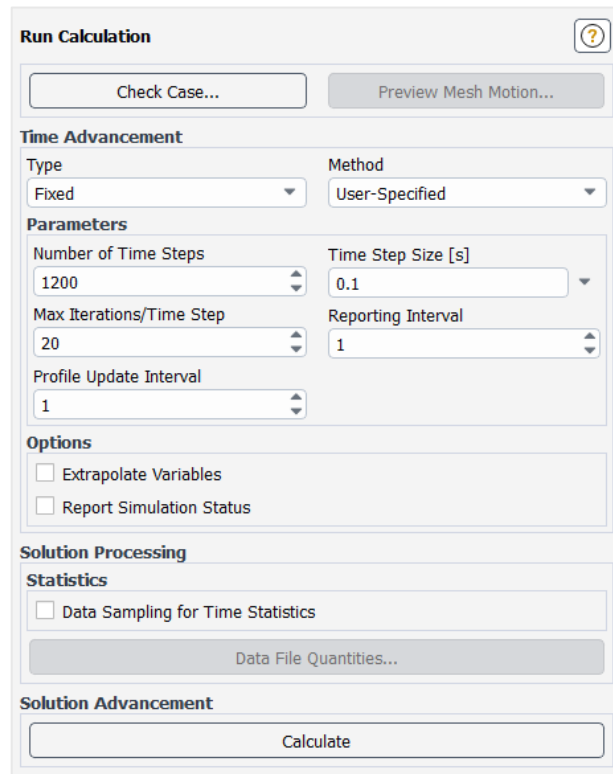


Figure 3-30. Time step and iteration count configuration in Ansys Fluent.

After the execution of all of the procedures described in this chapter, every scenario included in this thesis was executed by pressing the button “Calculate”, in the “Run Calculation” task page.

### A. Special Considerations for the Water-only Simulation

A preliminary water-only simulation was conducted prior to simulating the water-solid mixture flow within the flume. This scenario served two key purposes.

First, the results obtained for the water-only flow were compared with established analytical solutions, such as the Manning's equation. This comparison aimed to assess the accuracy and performance of the chosen computational fluid dynamics (CFD) model and the SST k- $\omega$  turbulence model employed in the simulations. By establishing a comparison between the simulated water surface profile and the solution from the Manning's equation for the same flume geometry, inlet velocity, and inclination, the model's ability to predict free-surface flows in the specific flume configuration was evaluated.

Second, simulating water flow without the complexities of solid particle interaction provided a clear understanding of the water's behaviour within the flume. This isolated analysis established a baseline for the following water-solid mixture simulations. By comparing the water-only scenario with the mixture scenarios, the influence of the presence of particles on the overall flow dynamics could be identified.

The water-only simulation setup is analogous to the water-solid mixture simulations in several aspects, with the primary difference being the number of phases involved. In this scenario, only two phases were considered (air and water). This contrasts with the three or four phases (air, water, and one or two solid phases) employed in the mixture simulations. The simulation was performed to achieve 2 minutes of flow duration, discretized in 0.1 seconds time-step.

The setup then is based in the following characteristics: First, the flume geometry remained a two-dimensional representation, replicating the actual flume's dimensions; Second, a constant inlet velocity of 1 [m/s] was employed; third, the flume has a  $0.5^\circ$  inclination angle; and finally, the SST k- $\omega$  turbulence model was chosen for consistency with the planned water-solid mixture simulations.

On the other hand, the analysis of the water-only simulation focused on three primary aspects:

- **Water Surface Location:** The location of the water surface within the flume was identified based by analysing the volume fractions of both phases.
- **Flow Depth Determination:** The flow depth (h) was determined by analysing the simulated water surface location relative to the bottom of the flume.
- **Comparison with Manning's Equation:** The most important aspect of this analysis involved comparing the simulated flow depth (h) with the results obtained from the Manning's equation for the same flume geometry, inlet velocity, and inclination. This comparison served as a preliminary validation of the CFD model's ability to predict free-surface flows.

### 3.6 Post-processing Software: Ansys CFD-Post

Ansys CFD-Post is a post-processing software specifically designed for visualizing and analysing the results generated by computational fluid dynamics (CFD) simulations performed using ANSYS Fluent. This software facilitates the transformation of complex simulation data into comprehensive and interpretable information. CFD-Post allows users to effectively evaluate flow characteristics, such as velocity, pressure, turbulence, and various other variables. By utilizing its graphical capabilities, CFD-Post enables the creation of informative plots, contours, and animation visualizations.

This chapter will describe the functionalities and applications of Ansys CFD-Post within the context of the current study, focusing on key parameters like the cross-sectional velocity distribution and volume fractions. It will be based on one of the cases, since the procedure to generate results is analogous in every case.

To start, it was necessary to go back to Ansys Workbench once the calculation process was done in Ansys Fluent. Here, a "Results" module was dragged from the "Toolbox" section over the "Solution" item within the pre-existent Ansys Fluent module. This created a new module that launched CFD-Post with a double click over it (See figure 3-31).

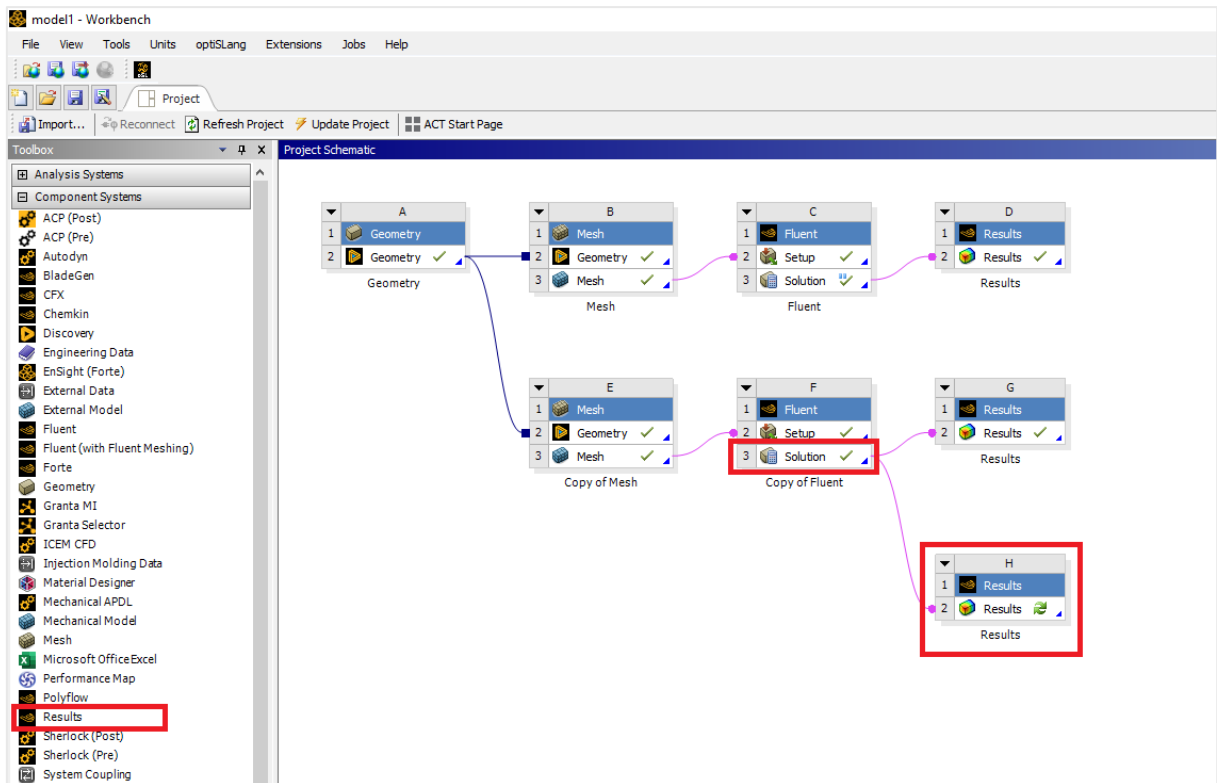


Figure 3-31. Ansys CFD-Post module added to the Ansys Workbench workspace.

The primary interface of Ansys CFD-Post was presented to the user following the simulation's completion (Figure 3-31). To obtain a clear two-dimensional view of the system within the X-Y plane, the Z-axis was deactivated by selecting it in the bottom-right corner of the window (highlighted in red in Figure 3-31).

Two principal tools were consistently employed in the analysis of various simulation scenarios within this thesis. These tools included:

- **Cross-Sectional Profiles:** This functionality facilitated the extraction and visualization of volume fraction and velocity profiles across user-defined cross-sections within the flume.
- **Contours:** This tool enabled the generation of density and velocity contour plots, providing a visual representation of the spatial distribution of these parameters within the flume.

The initial step involved defining the desired cross-section for generating a cross-sectional volume fraction plot. This definition was achieved by accessing the "Location" button within the ribbon menu (highlighted in blue in Figure 3-32). Selecting "Line" from the drop-down menu resulted in the opening of a window where a name was assigned for the cross section. In this instance, the name "CS1" was assigned for explanatory purposes.

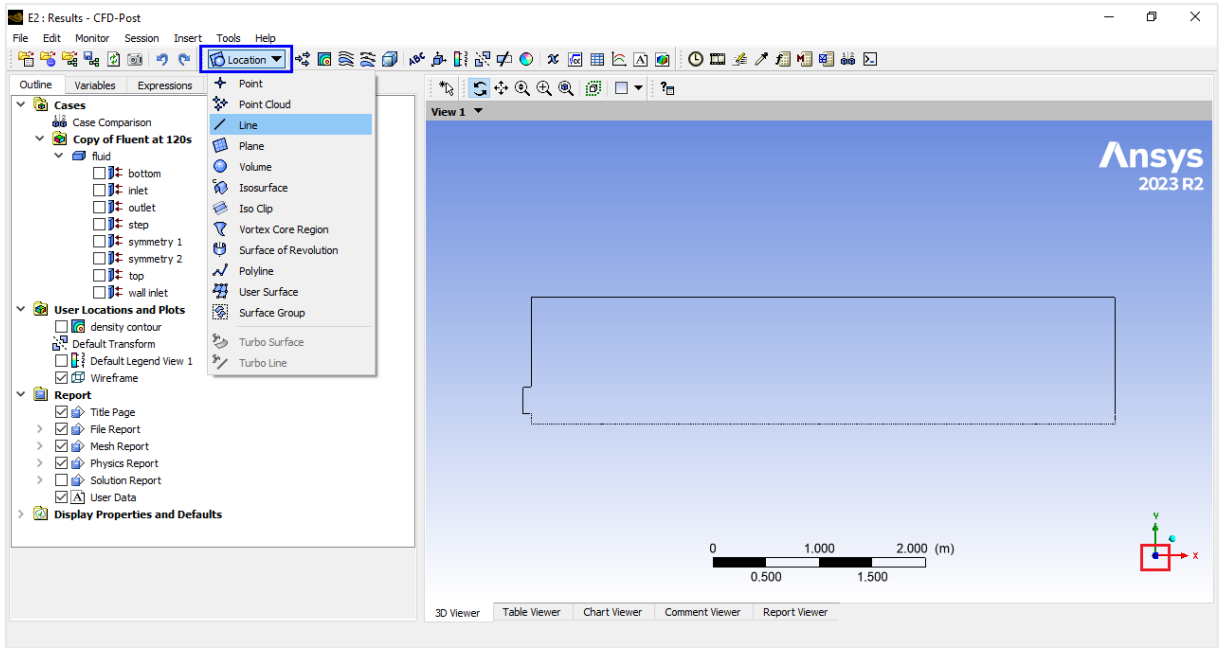


Figure 3-32. Main interface of CFD-Post and creation of "Line" element.

Following the selection of the "Line" option, a new configuration section titled "Details of CS1" was displayed in the right-hand pane (Figure 3-33). Within this section, the cross-section definition was established by specifying the coordinates of two points (highlighted in red). Subsequently, the "Apply" button was pressed to confirm the creation of cross-section CS1. This newly defined cross-section was then visualized in yellow within the main view of the system.

To generate a graph with the distribution of volume fractions across the defined cross-section, the "Chart" button located within the ribbon menu was subsequently selected (highlighted in blue in Figure 3-33). A little window opened again, where the name of the cross section was selected, which for explanation purposes will be "VFCS1".

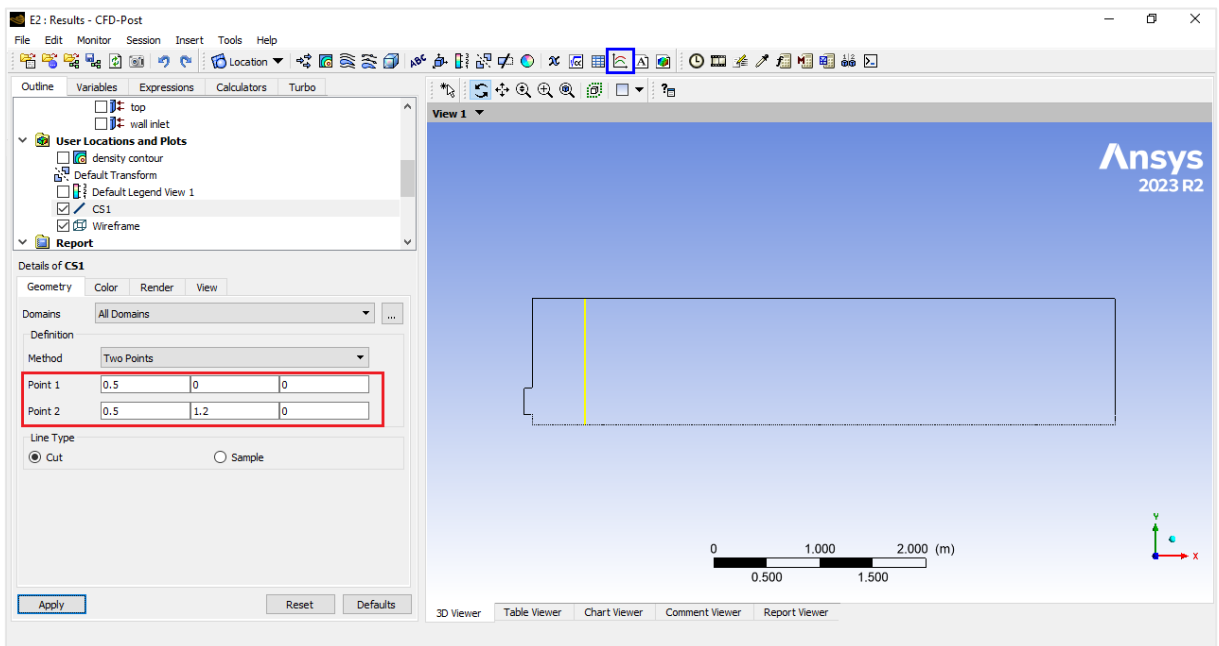


Figure 3-33. Cross section definition in CFD-Post.

A new section titled "Details of VFCS1" was created to document the data processing steps for the volume fraction plot at cross-section CS1 (Figure 3-34). This section details the user interface elements employed within the software package, and several tabs were utilized to configure the data to be plotted and the visual style of the resulting graph. These tabs are highlighted in red within Figure 3-34. This explanation will be centred in the definition of the variables for the chart ("General" tab) since the rest of the settings are mostly visual and very intuitive for the user.

It is noteworthy that the "3D Viewer" on the right side automatically transitioned to "Chart Viewer" mode, highlighted in blue within the same figure. A new data series was created by clicking the button highlighted in green, and then, the data series was named "Air Volume Fraction" within the designated "Name" section. Under the "Location" option, the previously created cross-section CS1 was selected from the available drop-down menu (highlighted in orange). Following the selection of the location, the "Custom Data Selection" option was chosen, leading to the opening of a new configuration section highlighted in magenta within Figure 3-34. Within this newly opened section, the specific variables intended for plotting were selected. For illustrative purposes, "Air.Volume Fraction" was chosen for the X-axis, and "Y" was chosen for the Y-axis. The chart creation process was analogous for every chart presented in the upcoming Results and Discussion chapter.

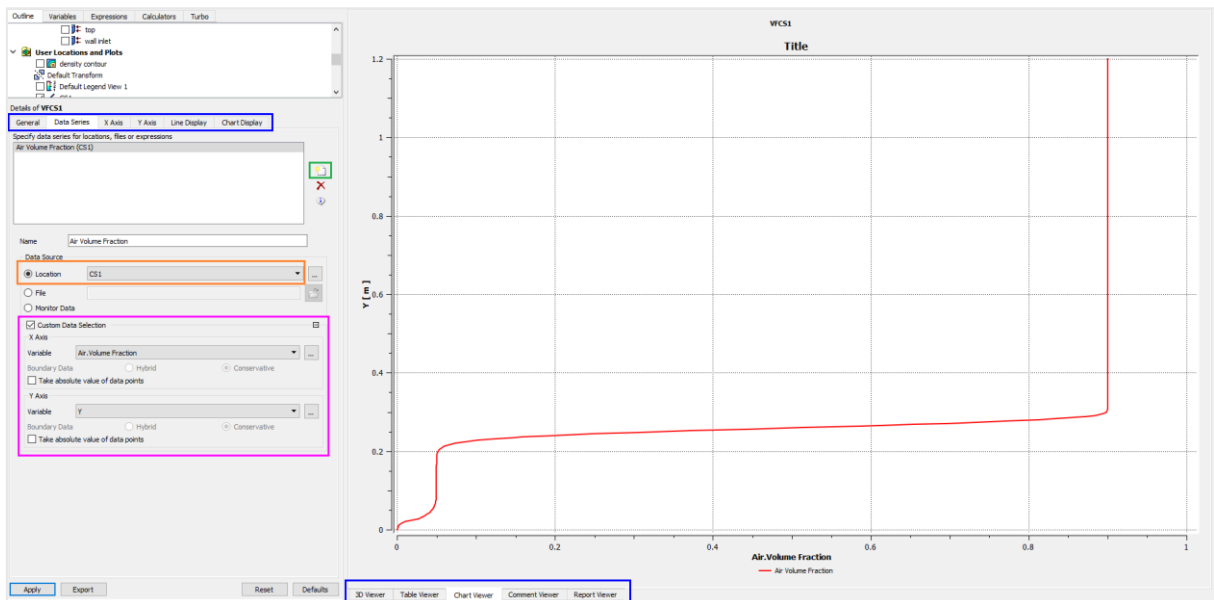


Figure 3-34. Creation of an example chart in CFD-Post.

Figure 3-35 illustrates the process of generating a density contour plot. The button highlighted in magenta was clicked to initiate a pop-up window where a name was assigned to the upcoming plot ("Density Contour" in this example). This action mirrored the process used for chart creation and resulted in a new section titled "Details of Density Contour" appearing on the left side of the interface.

Within this section, the domain and location for the contour plot was defined using the options highlighted in red in Figure 3-35. Subsequently, the variable to be plotted was selected, which in this case was "Density". The range was set to "Global" (highlighted in orange) allowing the software to automatically determine the appropriate limits based on the simulation results from Ansys Fluent.

The section highlighted in blue ("# of Contours") defined the number of contours within the chosen range. A value of 15 contours was selected for this example. Finally, the "Advanced Properties" section, highlighted in green, offered additional configuration options. These options included specifying the location of the variable (vertex or face of the cell), as well as customization of the colour scale and map for the resulting plot. Once again, the process was analogous for all of the contour plots presented in the Results and Discussion chapter.

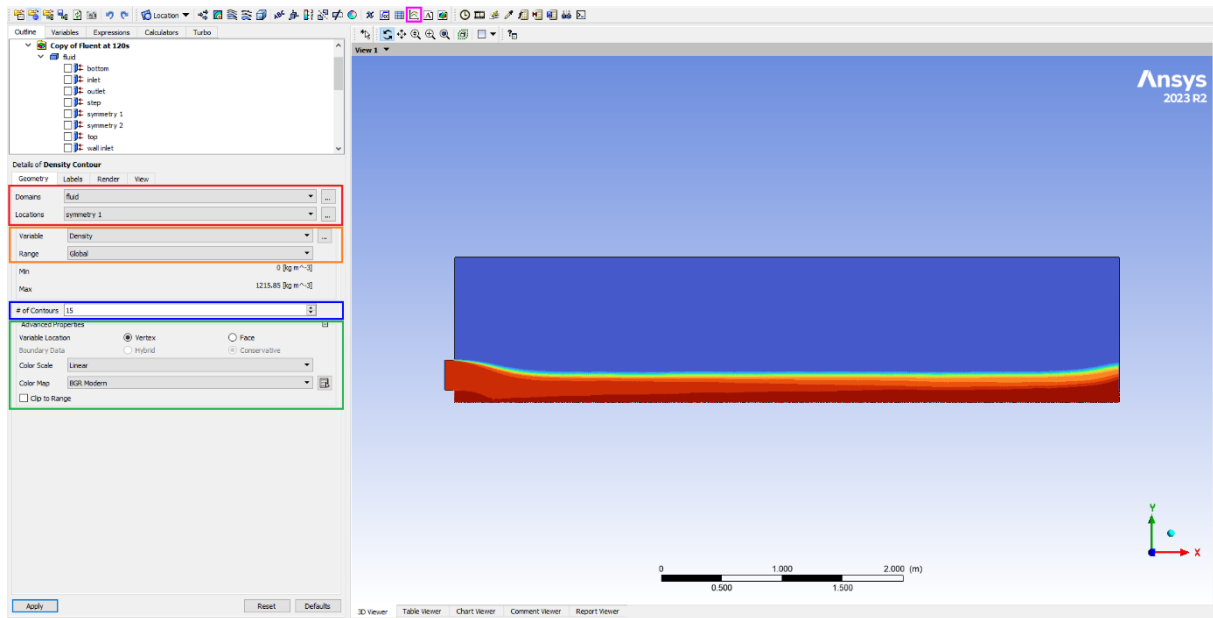


Figure 3-35. Creation of an example contour plot in CFD-Post.

## 4. Results and Discussion

The results of the various modelled scenarios are presented in two dedicated sections. The first section focuses on the unimodal granular flow, while the second section addresses the bimodal granular flow. This segregated presentation facilitates a clear and focused examination of the findings for each flow type.

To facilitate the analysis of the flow behaviour within the flume, three representative cross-sections were chosen along the flow path (Figure 4-1). These cross-sections, denoted as CS1, CS2, and CS3, represent specific locations where detailed information about the flow properties, such as volume fractions and velocities of the water and solid phases, can be extracted. Specific reasons for the localization of these cross sections exist:

- **CS1:** Located 0.5 meters downstream from the inlet, CS1 captures the initial development of the flow. Due to its proximity to the inlet, the water surface profile at this section is expected to exhibit a curvature. Additionally, at this stage, the water-solid mixture is anticipated to be homogeneously mixed without any signs of stratification.
- **CS2:** Situated at the midpoint of the flume, CS2 allows for the evaluation of potential changes in flow characteristics compared mostly to CS3, located further downstream almost at the end of the flume. This comparison will reveal any transformations in the distribution and interaction of the water and solid phases as the mixture progresses along the flume length.

- **CS3:** Located 0.5 meters upstream from the outlet, CS3 location is chosen to assess mainly if the flow is completely developed before the end of the flume, and secondarily to capture the influence of the step structure. The segregation of the phases should appear at this point.

In the water-only simulation, the same cross sections are maintained for comparison purposes, even though there is no analysis of solid phase segregation performed. Nevertheless, the curvatures at the beginning and the end of the flume are still expected to occur.

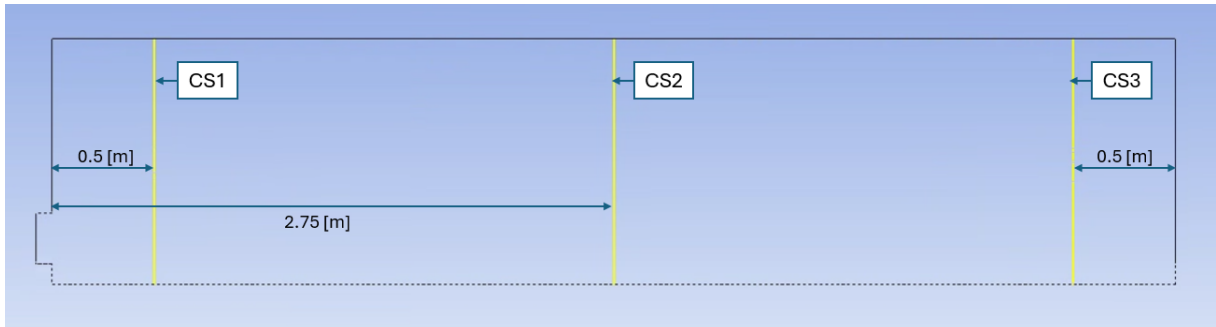


Figure 4-1. Cross section definition (CS1, CS2 and CS3).

## 4.1 Water-only Flow

To gain understanding of the water's behaviour within the flume before introducing solid particles, a preliminary simulation was conducted using a water-air multiphase system, using the procedure described in the Methodology chapter. Figure 4-2 presents a density contour plot that visualizes the overall flow pattern. As expected, the water exhibits two distinct curvatures. The first curvature occurs at the beginning of the flume due to the step-down inlet, where the water flow adjusts to the new geometry. The second curvature is observed at the end of the flume, likely caused by the accumulation step structure influencing the flow profile.

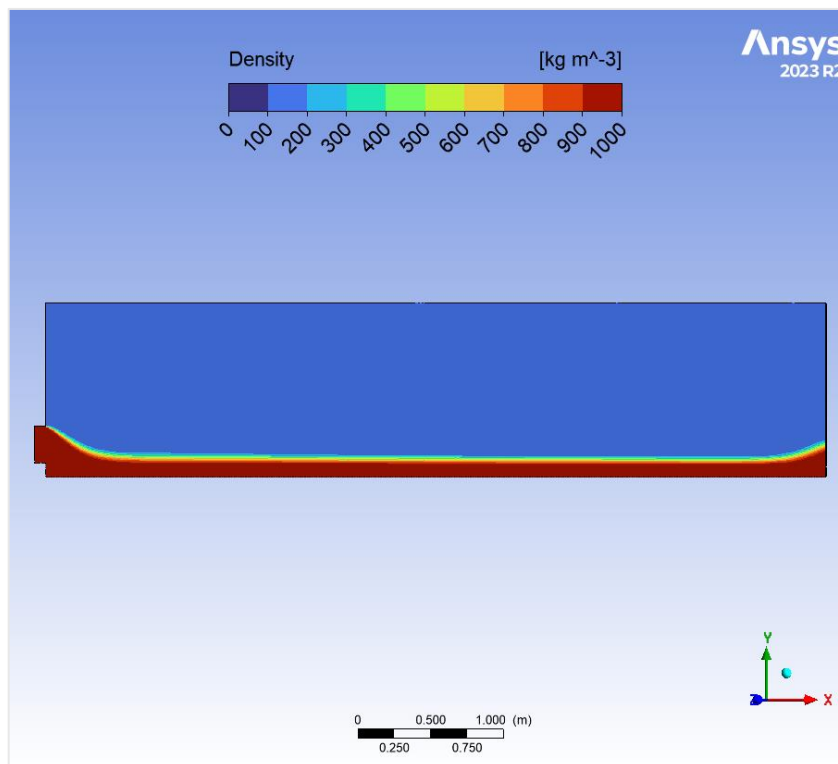


Figure 4-2. Density contour plot. Water-only simulation. Inlet velocity: 1 [m/s], Inclination: 0.5°.



Figures 4-3 presents volume fraction plots along cross-sections CS1, CS2, and CS3, respectively. These plots are useful for identifying the location of the water surface, which was assumed to occur where the volume fractions of air and water are equal [8]. The water surface elevations from the bottom are 0.144 [m] at CS1, 0.126 [m] at CS2, and 0.121 [m] at CS3. As expected, the flow depth progressively decreases from CS1 towards CS3, reflecting the development of the flow along the flume. Notably, the calculated development length ( $L_d$ ) for this flow is 3.417 [m], indicating that the flow becomes fully developed by the time it reaches CS3.

The calculated Froude number (1.89) shows a supercritical flow regime at CS3, which is an important observation because supercritical flow is not significantly influenced by downstream conditions, including the step structure and its associated curvature in the water surface profile.

For comparison, the flow depth obtained using Manning's equation with a friction coefficient of  $n = 0.010$  is  $h = 0.1139$  [m]. This value represents a percentual error of approximately 6.23% compared to the estimated water depth at CS3 based on the simulation results.

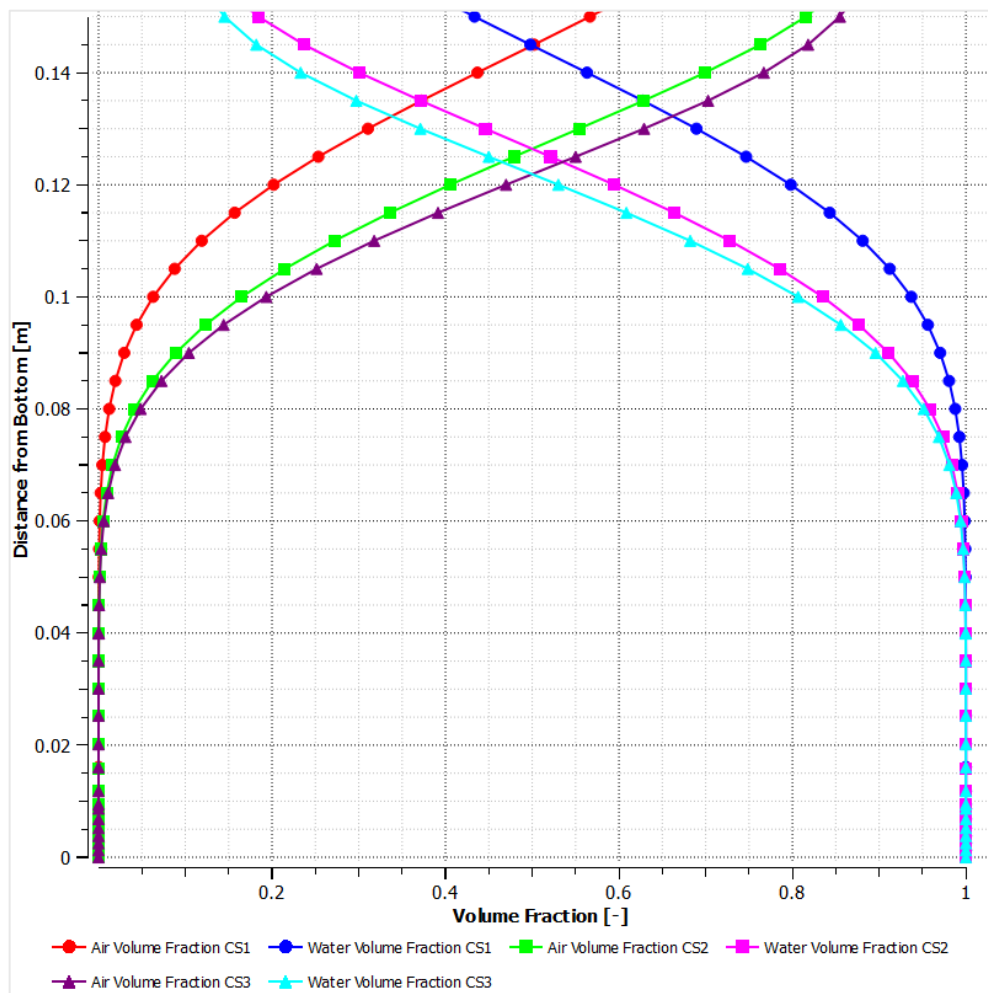


Figure 4-3. Volume fractions plot over CS1, CS2 and CS3. Water-only simulation. Inlet velocity: 1 [m/s], Inclination: 0.5°.

Similar to the volume fractions analysis, the velocity profiles across CS1, CS2, and CS3 are shown in Figure 4-4, as well as the flow depths for the same cross sections for enhanced interpretation. As expected, the velocity profile at CS1 exhibits a lower average velocity compared to CS2 and CS3. This corresponds well with the higher flow depth observed at CS1, where the water experiences greater frictional resistance from the flume bed.

Moving downstream to CS2, the velocity profile begins to approach a more expected distribution, yet it is not entirely identical to the profile at CS3. This subtle difference suggests that the flow at CS2 is likely close to, but not yet fully developed according to the calculated development length ( $L_{d,min} = 4.84 [m]$ ). In contrast, the velocity profile at CS3, located beyond the development length, exhibit what could be a definitive distribution across the flow depth in case the assumption of  $\alpha = 10$  is correct.

This analysis of the velocity profiles reinforces the importance of flow development in understanding the flow behaviour within the flume. The progressive decrease in flow depth across the channel width highlight the transformation of the flow from its initial state at the inlet to a fully developed state further downstream.

The comparison of the simulated water surface profile with the solution from the Manning's equation for the same flume geometry, inlet velocity, and inclination provided a preliminary validation of the chosen turbulence model (SST k- $\omega$ ). The observed discrepancy of approximately 6.23% between the simulated and calculated flow depths suggests acceptable accuracy for proceeding with the more complex water-solid mixture simulations.

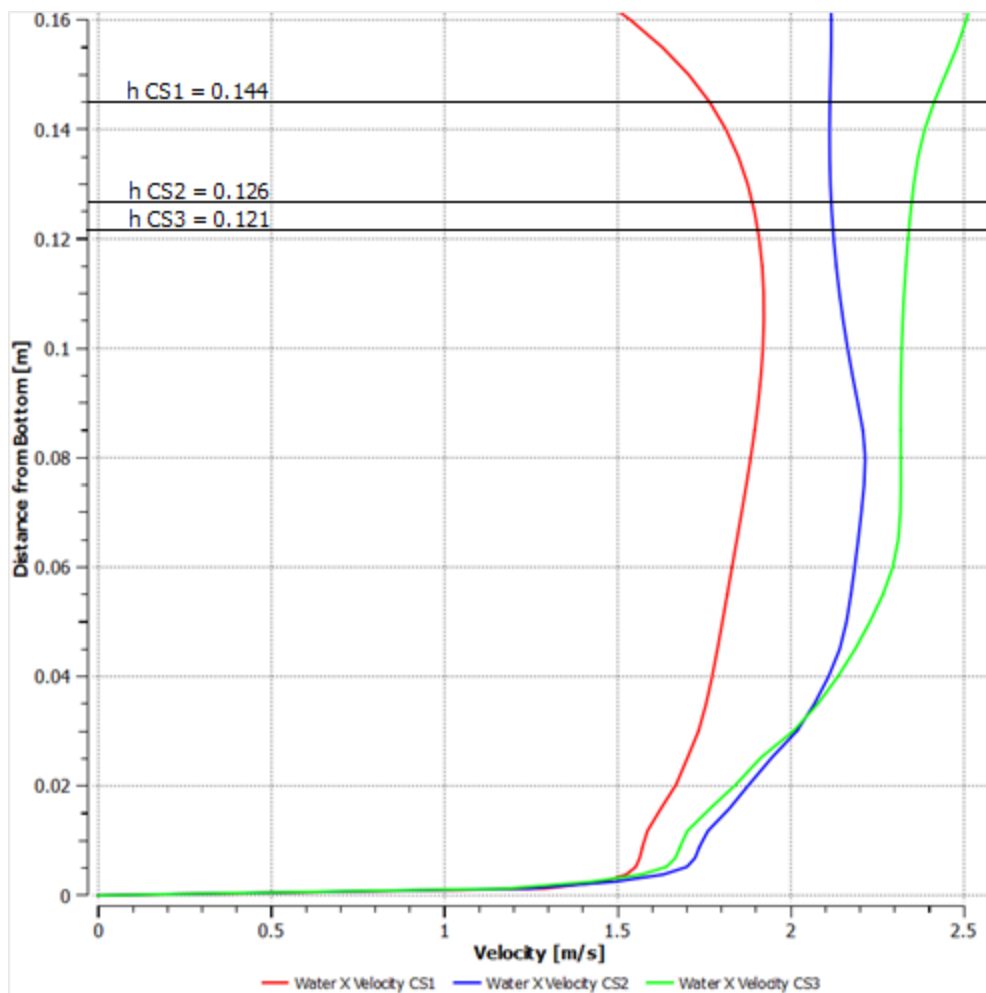


Figure 4-4. Velocity distribution plot over CS1, CS2 and CS3. Water-only simulation. Inlet velocity: 1 [m/s], Inclination: 0.5°.

## 4.2 Unimodal Flow

The water-solid mixture simulation utilized a two-dimensional flume model tilted at an angle of  $0.5^\circ$ . The model simulated a mixture of water and coarse particles (diameter: 0.00365 m, density:  $1368 \text{ kg/m}^3$ ) entering the flume inlet. The inlet velocity of the mixture was set to 1 m/s, resulting in a flow rate of  $0.25 \text{ m}^2/\text{s}$  (See Table 4-1). The simulation employed a time step of 0.1 seconds with 20 iterations per time step. A total of 1200 time steps were executed, corresponding to a simulated flow duration of 2 minutes. The flow achieved a relatively stable state within the first minute and exhibited minimal instabilities thereafter. This chosen simulation duration ensures a stable flow state suitable for further analysis. Therefore, the final time step provides the most appropriate data for a deeper investigation of the flow behaviour.

Table 4-1. Summary of unimodal flow conditions scenarios.

| Scenario | Channel Slope | Water       |                | Air         |                | Solids      |                |             |                |
|----------|---------------|-------------|----------------|-------------|----------------|-------------|----------------|-------------|----------------|
|          |               | V. Fraction | Velocity [m/s] | V. Fraction | Velocity [m/s] | Coarse      |                | Fine        |                |
|          |               |             |                |             |                | V. Fraction | Velocity [m/s] | V. Fraction | Velocity [m/s] |
| Unimodal | $0.5^\circ$   | 0.0.65      | 1              | 0.05        | 1              | 0.3         | 1              | Not Used    | Not Used       |

A density contour plot presented in Figure 4-5 visualizes the overall distribution of the three phases (water, air, and coarse particles) within the system at the final time step. This plot shows the computational mesh, with each cell's density value calculated as a weighted average based on the volume fraction of each phase occupying that cell. As evident from the figure, regions with higher density are concentrated near the flume bottom, indicating a greater concentration of solid particles in this zone. The density gradually decreases as we move upwards towards the top of the flume, where the air-water interface is located. The density plot also reveals a zone of high density just after the inlet, which might be attributed to an accumulation of particles or a swirling flow phenomenon. Finally, the plot clearly shows a distinct layer of water (light orange) occupying the last two-thirds of the flume, which shows that the solid phase necessitates a certain length to settle underneath the water.

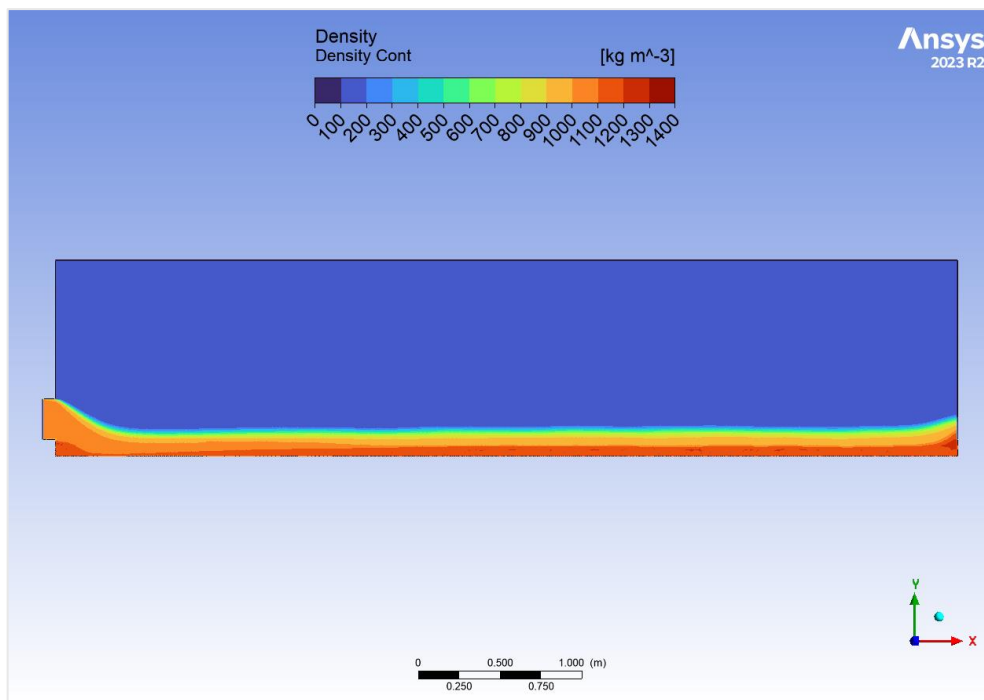


Figure 4-5. Density contour plot. Unimodal flow. Inclination:  $0.5^\circ$ , inlet velocity: 1 [m/s].

Figures 4-6, 4-7, and 4-8 show the volume fraction distribution across the previously analysed cross-sections (CS1, CS2, and CS3). The water surface location was estimated at the point where the water and air volume fractions become equal [8]. Based on this approach, the water surface heights are estimated to be 0.145 [m], 0.157 [m], and 0.163 [m] above the flume bottom for CS1, CS2, and CS3, respectively. CS1, located closest to the inlet, exhibits a lower water surface depth likely due to the convex curvature observed in the density contour plot (Figure 4-5). This curvature gradually disappears in CS2 and CS3, leading to progressively higher water surface levels.

The volume fraction plots reveal pattern in the distribution of the single solid phase (coarse particles) throughout the flume depth. Notably, CS1, despite being the initial section and lacking significant flow development, already exhibits a higher presence of particles near the bottom. Moving downstream to CS2, we observe a mix of particles and water extending approximately 7 [cm] above the bottom. This region displays fluctuating volume fractions, suggesting a dynamic interaction between the particles and the water flow. Notably, the water volume fraction tends to be higher in the upper half compared to CS1, which might be a preliminary indication of developing stratification.

Finally, at CS3, the flow behaviour becomes more stable. Here, the particle-water mixture occupies the lower 6 [cm], while the water volume fraction dominates the upper half. This pattern suggests a more developed state of stratification compared to CS1 and CS2. The increasing stability in the volume fraction distribution across the depth indicates a progression towards a fully developed flow regime further downstream.

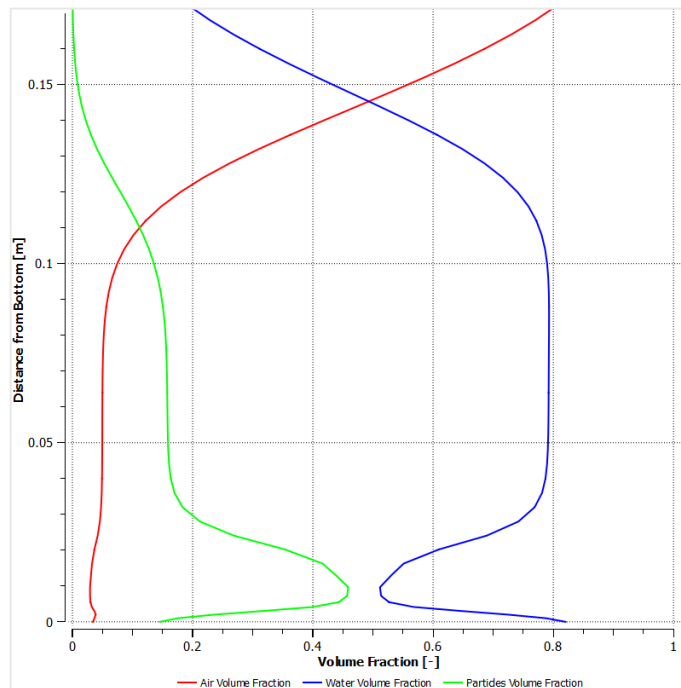


Figure 4-6. Volume fraction of air, water, and particles, and fine particles over CS1. Unimodal flow. Inclination: 0.5°, inlet velocity: 1 [m/s].

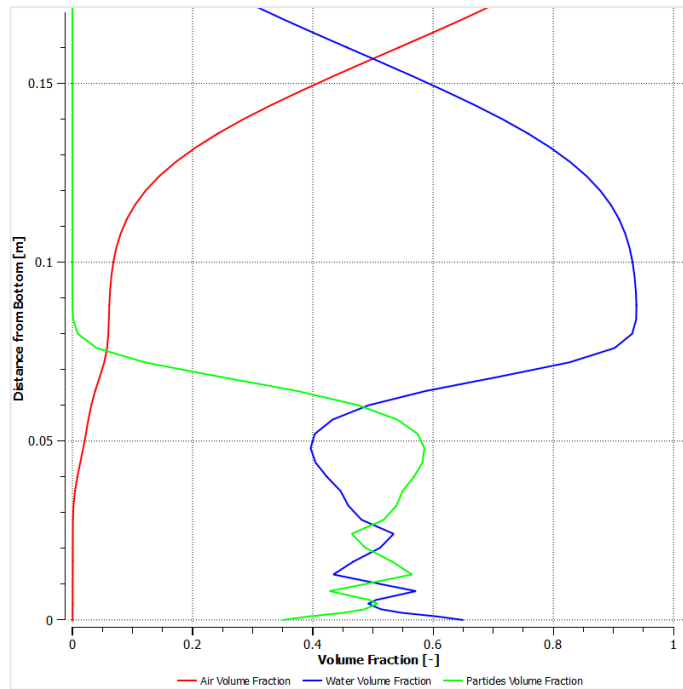


Figure 4-7. Volume fraction of air, water, and particles, and fine particles over CS2. Unimodal flow. Inclination:  $0.5^\circ$ , inlet velocity: 1 [m/s].

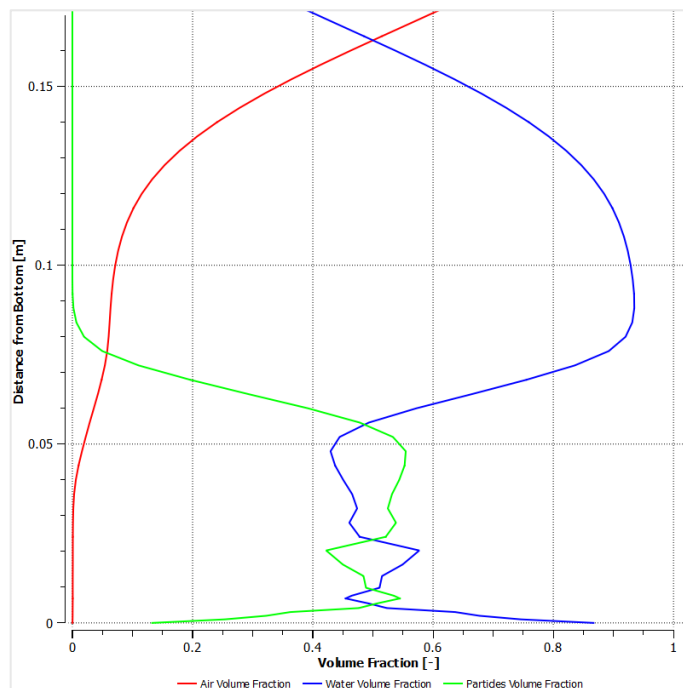


Figure 4-8. Volume fraction of air, water, and particles, and fine particles over CS3. Unimodal flow. Inclination:  $0.5^\circ$ , inlet velocity: 1 [m/s].

The velocity profiles across CS1, CS2, and CS3 (Figures 4-9, 4-10 and 4-11) provide more information about the development of the flow throughout the flume. At CS1, the closest section to the inlet, the velocity profiles for both water and particles exhibit a high degree of similarity. The water velocity, however, is slightly higher compared to the particle velocity. This observation aligns with expectations, as water serves as the primary driving force for the particles within the mixture. Furthermore, considering the homogeneous mixture entering the

flume from the inlet (as observed in the CS1 volume fraction plot), interactions between particles are likely minimal at this early stage.

Moving downstream to CS2, a more complex behaviour can be noticed. Above 3 [cm] from the bottom, the water phase exhibits a higher velocity compared to CS1. The particle velocity, in contrast, shows a dramatic decrease, reaching zero at the water surface. This behaviour aligns with the developing stratification observed in the CS2 volume fraction plot, where the water increasingly occupies the upper half of the flume. Below 3 [cm], the velocity profiles for both phases display more fluctuations, though not very intense. These fluctuations can be explained by the combined effect of several forces acting on the particles. Imagine the particles here are not bouncing around (colliding) as much, but instead rubbing against each other and the flume wall like a smooth layer. This sliding motion allows the particles to stay in contact with each other and the wall for longer periods compared to the quicker, bouncing interactions they can experience in the upper parts of the flow<sup>4</sup>.

At CS3, the furthest downstream section and expected to represent a more developed flow regime, the analysis needs to consider the combined insights from both the velocity and volume fraction plots. The presence of non-zero velocities for particles above 9 [cm] from the bottom is inconsistent with the volume fraction plot at CS3, which shows zero particle concentration in that region. This discrepancy suggests a potential miscalculation arising from numerical limitations of the CFD solver. Focusing on the valid portion of the velocity profile at CS3 (below 9 [cm]), a pattern emerges. The distribution of velocities appears reasonable, with minor fluctuations observed around the 3 [cm] mark, and their occurrence, being similar to those observed in CS2, could be associated with the previously discussed phenomenon.

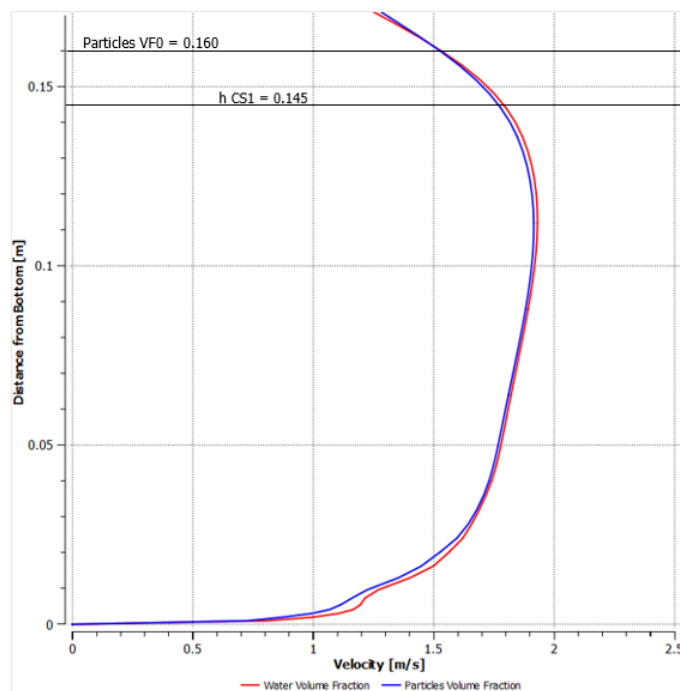


Figure 4-9. Velocities of water and particles over CS1. Unimodal flow. Inclination:  $0.5^\circ$ , inlet velocity: 1 [m/s].

<sup>4</sup> Further discussion on this topic is developed in the bimodal flow analysis.

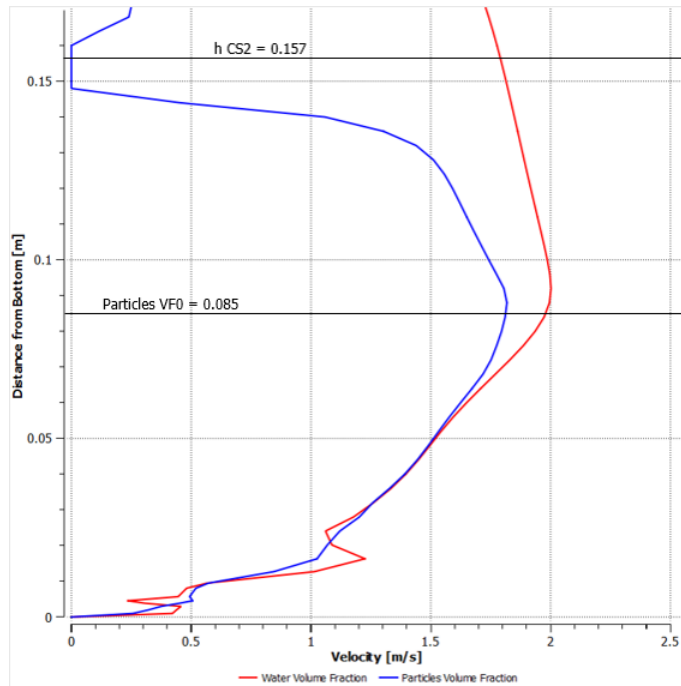


Figure 4-10. Velocities of water and particles over CS2. Unimodal flow. Inclination:  $0.5^\circ$ , inlet velocity: 1 [m/s].

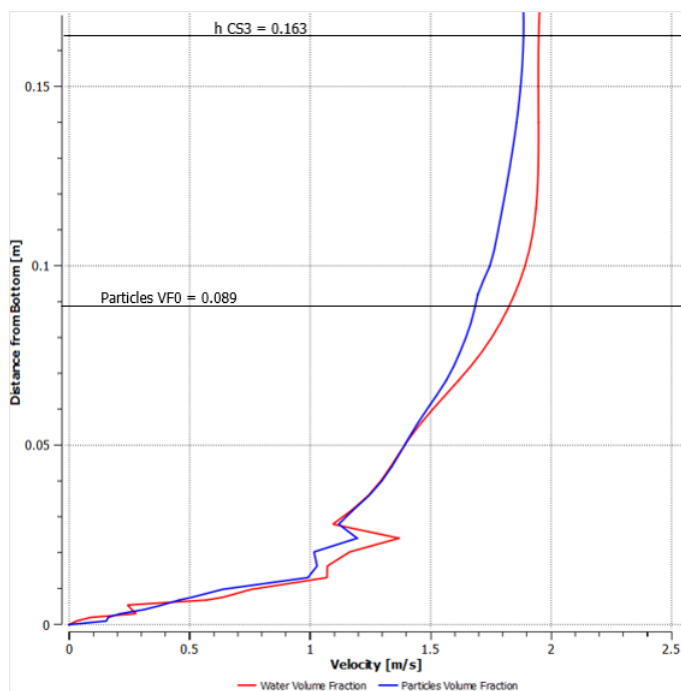


Figure 4-11. Velocities of water and particles over CS3. Unimodal flow. Inclination:  $0.5^\circ$ , inlet velocity: 1 [m/s].

Figure 4-12 offers a broader perspective on the horizontal ("X") velocity distribution for the solid particles throughout the flume. While lacking the detailed resolution of the velocity profiles at specific cross-sections, this plot provides a valuable overview of the flow.

In the first third of the flume, the particle velocities exhibit a more homogeneous pattern, mirroring the observations from the velocity plots at CS1 (Figure 4-9). This aligns with the initial mixing stage where the combined particle and water mixture is just entering the flume. Moving downstream, however, the picture changes. The particle velocities begin to differentiate,

forming distinct layers with varying velocity magnitudes. Notably, a pronounced zone of low velocities appears near the bottom in the vicinity of CS3. This observation reinforces the trend of particle settling and stratification observed in the velocity plots at CS3 (Figure 4-11).

Directly below the point where the inlet structure connects with the flume, a small zone with negative velocities is evident. This can be attributed to a localized swirling phenomenon, which is expected given the geometrical change at the inlet. Subsequently, some small dark green artifacts appear above the water surface in the first half of the flume, indicating seemingly positive velocities for particles in the air. This is unlikely to occur and can likely be attributed to minor miscalculations within the numerical solver used for the simulation.

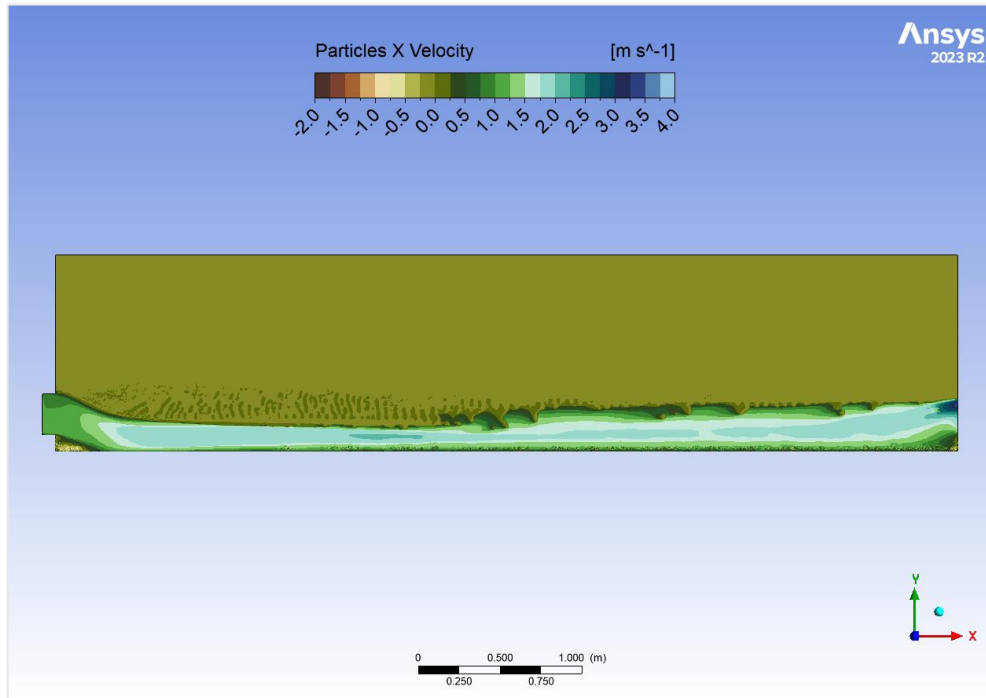


Figure 4-12. Particles velocity (X direction) contour plot. Unimodal flow. Inclination: 0.5°, inlet velocity: 1 [m/s].

The unimodal flow analysis provides a foundational point of view of the flow behaviour, however, the presence of two distinct solid phases in the bimodal flow scenario introduces additional complexities. The collisions or rubbing between the two particle sizes, their interactions with the water, and the resulting stratification patterns requires a deeper analysis, potentially revealing more pronounced segregation effects compared to the unimodal case.



### 4.3 Bimodal Flow

Following the evaluation of the solver software's performance in simulating unimodal granular flow, this chapter treats more complex scenarios involving bimodal particle size distributions. By incorporating two distinct particle sizes, these simulations aim to capture a more realistic representation of sediment transport in open channels. As with the unimodal simulations, a key objective remains assessing the solver's ability to handle granular flow phenomena. To achieve this, the simulations presented here utilize an analogous software configuration compared to the unimodal cases, being the adding of a new phase the only difference between the two types of simulations. Table 4-2 summarizes the input parameters for the various bimodal scenarios investigated in this chapter.

Table 4-2. Summary of bimodal flow conditions scenarios.

| Scenario | Channel Slope | Water       |                | Air         |                | Solids      |                |             |                |
|----------|---------------|-------------|----------------|-------------|----------------|-------------|----------------|-------------|----------------|
|          |               | V. Fraction | Velocity [m/s] | V. Fraction | Velocity [m/s] | Coarse      |                | Fine        |                |
|          |               |             |                |             |                | V. Fraction | Velocity [m/s] | V. Fraction | Velocity [m/s] |
| 1        | 0.5°          | 0.75        | 1              | 0.05        | 1              | 0.2         | 1              | 0.2         | 1              |
| 2        | 0.5°          | 0.75        | 2              | 0.05        | 2              | 0.2         | 2              | 0.2         | 2              |
| 3        | 1°            | 0.75        | 1              | 0.05        | 1              | 0.2         | 1              | 0.2         | 1              |
| 4        | 1°            | 0.75        | 2              | 0.05        | 2              | 0.2         | 2              | 0.2         | 2              |

#### A. Scenario 1

Based on the information presented in Table 4-5, the first scenario employed a two-dimensional flume model with an 0.5° of inclination. This model simulated a mixture of water and particles entering the flow zone through the inlet structure. The mixture inlet velocity was set to 1 [m/s], corresponding to a flow rate of 0.25 [m<sup>2</sup>/s]. The simulation utilized a time step of 0.1 seconds with 20 iterations per time step. A total of 1200 time-steps were executed, resulting in a simulated flow duration of 2 minutes. The flow achieved a state of relative stability within the first minute, exhibiting minimal instabilities after this. The simulation duration was chosen to ensure a stable flow state suitable for analysis, that's why the last time-step is the most appropriate to perform a deeper analysis.

To visualize the overall distribution of phases within the system at the final time step, a density contour plot is presented in Figure 4-13. This contour plot shows the computational mesh, with density values calculated as a weighted average based on the volume fraction of each phase occupying a particular cell. As evident from the figure, higher density regions are concentrated near the flume bottom, indicating a greater presence of the solid phases in this zone, decreasing while approaching the gas-liquid interphase.

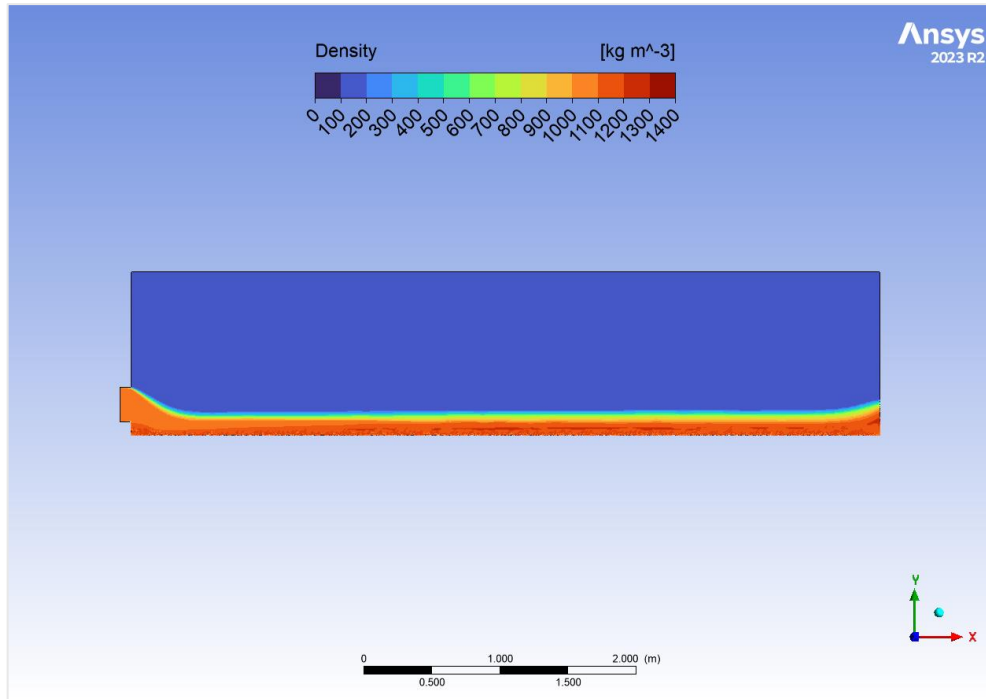


Figure 4-13. Density contour plot. Bimodal flow. Inclination:  $0.5^\circ$ , inlet velocity:  $1 \text{ [m/s]}$ .

Figures 4-14, 4-1, and 4-16 present a detailed examination of the volume fraction distribution across the previously analysed cross-sections (CS1, CS2, and CS3). A key observation corresponds to the identification of the water surface location, which is assumed to occur where the volume fractions of water and air become equal [8]. Based on this criterion, the water surface in CS1 is estimated to be situated  $0.142 \text{ [m]}$  above the flume bottom. Similarly, the water surface in CS2 and CS3 is estimated to be  $0.155 \text{ [m]}$  and  $0.157 \text{ [m]}$  respectively, above the bottom. This analysis aligns with expectations considering the position of the cross-sections. CS1, located closest to the inlet, exhibits a water surface curvature as observed in the density contour plot (Figure 4-13). In contrast, CS2 and CS3 are less to not influenced by this curvature due to their distance from the inlet structure. However, CS3 might be slightly influenced by the curvature of the outlet step structure, leading to a slightly higher flow depth.

The volume fractions of the solid phases reveal minimal signs of accumulation at the flume bottom in this scenario. In all three cross-sections, both solid phases exhibit non-zero velocities, suggesting minimal settling. Furthermore, CS1 displays minimal stratification of the solid phases, which is reasonable as the mixture is just entering the flume remembering that it's homogeneously incorporated in the inlet. Then, CS2 and CS3 exhibit a clearer stratification, with coarser particles concentrated closer to the bottom compared to the finer ones, which indicates a segregation process occurring as the flow progresses downstream. Additionally, a higher volume of water is observed flowing above the solid phases across all three cross-sections. The initial 2 centimetres above the flume bottom exhibit significant fluctuations in the volume fractions of both particles and water. This phenomenon can likely be attributed to the complex interplay of forces occurring in this near-wall region. These interactions include wall shear stresses acting between the particles themselves, between the particles and the flume wall, and between the particles and the water. Here, imagine the particles behave more like a sliding layer rather than experiencing purely collisional interactions. This sliding motion could lead to longer-lasting contacts between particles and between the particles and the wall (bottom) compared to collisional encounters observed in the bulk flow. These extended contacts could potentially explain the observed fluctuations in the volume fractions within this region.

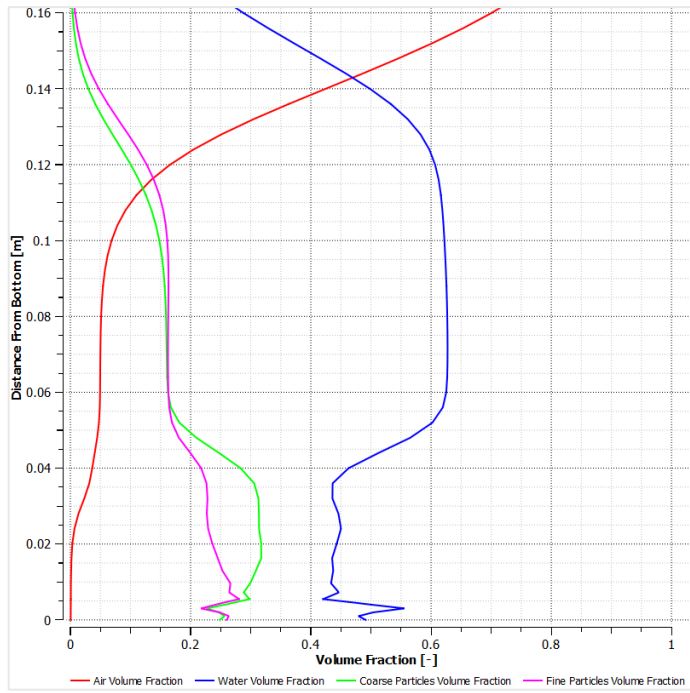


Figure 4-14. Volume fraction of air, water, coarse particles, and fine particles over CS1. Bimodal flow. Inclination: 0.5°, inlet velocity: 1 [m/s].

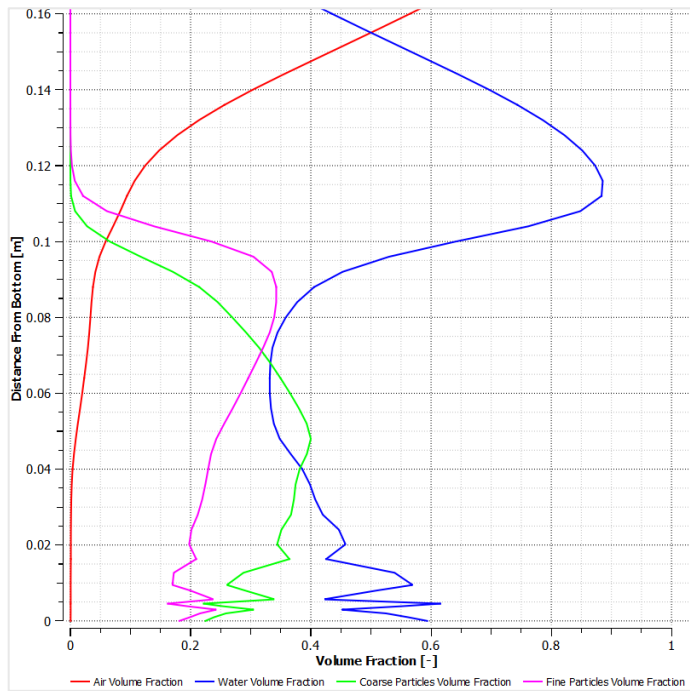


Figure 4-15. Volume fraction of air, water, coarse particles, and fine particles over CS2. Bimodal flow. Inclination: 0.5°, inlet velocity: 1 [m/s].

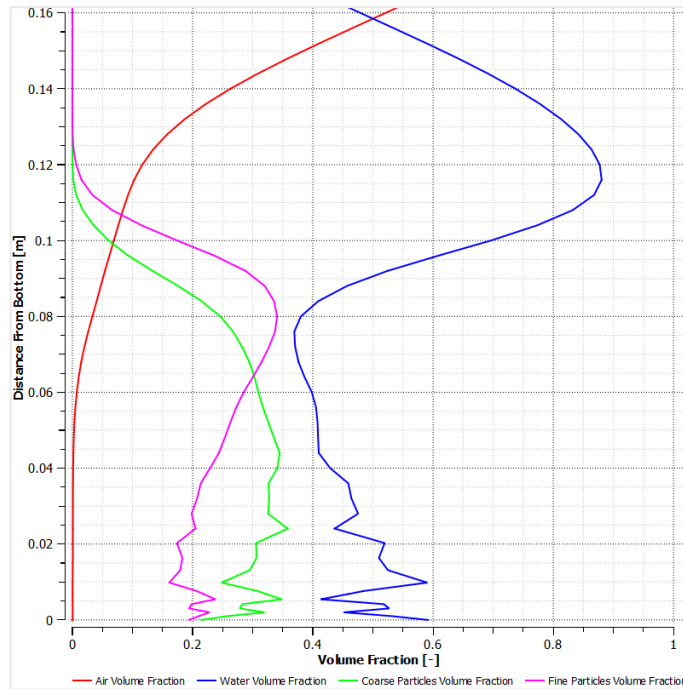


Figure 4-16. Volume fraction of air, water, coarse particles, and fine particles over CS3. Bimodal flow. Inclination:  $0.5^\circ$ , inlet velocity: 1 [m/s].

Figures 4-17, 4-18, and 4-19 show the horizontal (“X”) velocity profiles of the water and solid phases across cross-sections CS1, CS2, and CS3, respectively. The vertical (“Y”) velocities are observed to be minimal and are therefore considered to have a negligible impact on the overall flow behaviour. As expected, the velocity distribution in CS1 exhibits a uniform profile. Since this location is closest to the inlet, the mixing has not yet undergone significant development, resulting in a consistent velocity distribution across the channel depth.

In cross-section CS2, the coarser particles exhibit a lower velocity in the upper-middle region of the flow. The finer particles, however, display an unexpected behaviour where their velocity is slightly higher than the water velocity between approximately 0.11 [m] and 0.14 [m] above the flume bottom. This observation is considered unlikely in this zone due to the near-zero volume fraction of fine particles, as observed in the previous analysis. This discrepancy is likely attributable to numerical inaccuracies associated with the chosen solver method. A similar analysis can be made regarding the existence of non-zero velocities of coarse particles in the same zone. Near the flume bottom, all phases exhibit significant velocity fluctuations. Here, the particles generally maintain higher velocities compared to the water in at least two zones. This behaviour is considered more plausible within this region due to the higher concentration of particles, which can lead to a sliding behaviour of particle clusters. A similar analysis can be applied to the velocity profiles at cross-section CS3. These profiles exhibit a similar distribution compared to the ones observed in CS2, with the notable exception of an additional zone of intense fluctuations in the vicinity of the flume bottom. This new zone is located between 0.01 [m] and 0.03 [m] above the bed. The depths where the volume fraction of the coarse and fine particles reaches zero is also included in each velocity plot to enhance understanding.

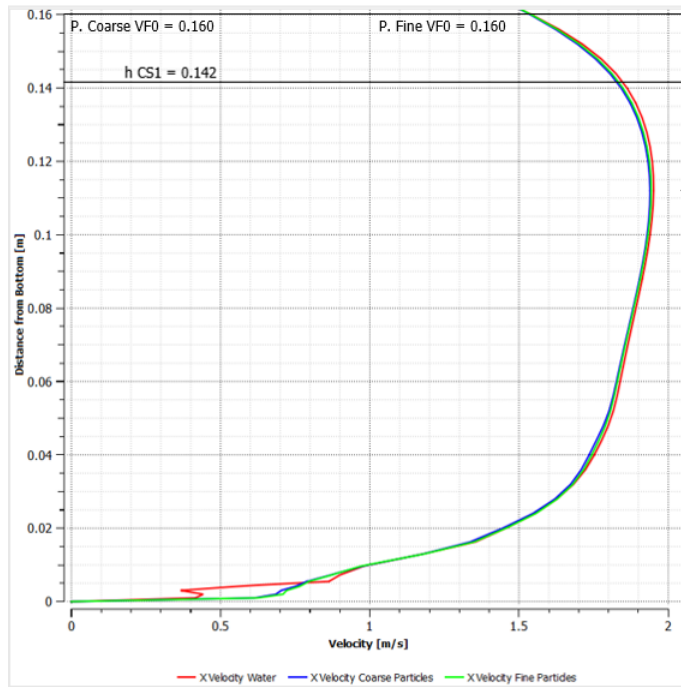


Figure 4-17. Velocities of water, coarse particles, and fine particles over CS1. Bimodal flow. Inclination:  $0.5^\circ$ , inlet velocity: 1 [m/s].

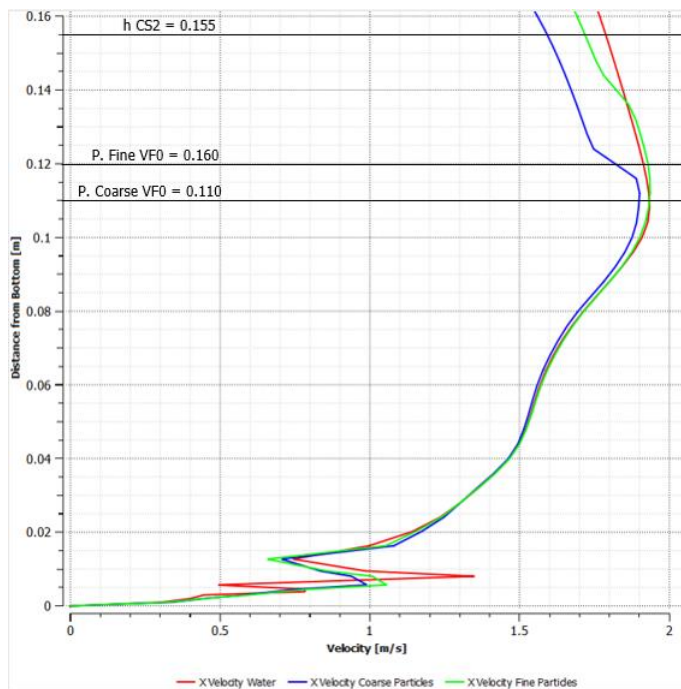


Figure 4-18. Velocities of water, coarse particles, and fine particles over CS2. Bimodal flow. Inclination:  $0.5^\circ$ , inlet velocity: 1 [m/s].

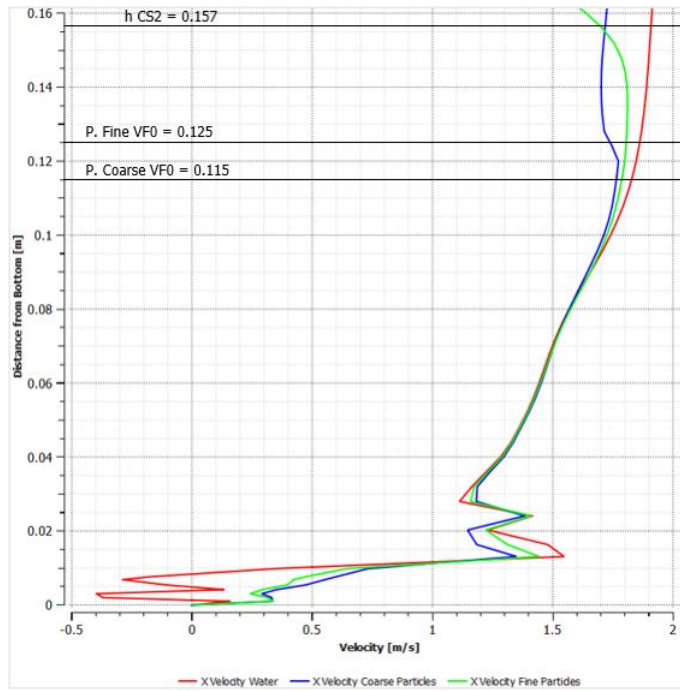


Figure 4-19. Velocities of water, coarse particles, and fine particles over CS3. Bimodal flow. Inclination:  $0.5^\circ$ , inlet velocity:  $1 \text{ [m/s]}$ .

To continue with the analysis of this scenario, Figures 4-12 and 4-13 present horizontal velocity contour plots for the coarse and fine particle phases, respectively. While these plots offer a broader view of the flow compared to the cross-sectional profiles, they don't capture deep insights into the flow behaviour. Nevertheless, they are a valuable tool for visualizing the longitudinal development of the flow velocity. As observed in the figures, the water-solids mixture exhibits generally higher, more uniform velocities in the first third of the flume (all three phases). This velocity stabilizes as it approaches the mid-section and remains relatively constant until reaching the outlet zone. Here, an increase in velocity is observed due to the evacuation through the atmospheric pressure boundary condition, right over the step structure.

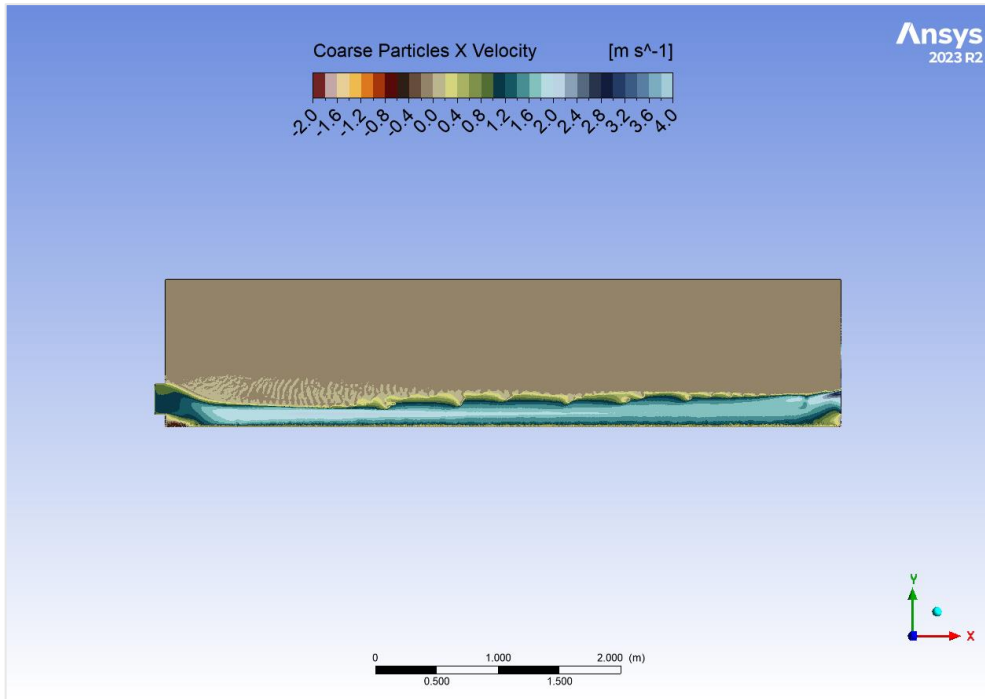


Figure 4-20. Coarse particles velocity (X direction) contour plot. Bimodal flow. Inclination: 0.5°, inlet velocity: 1 [m/s].

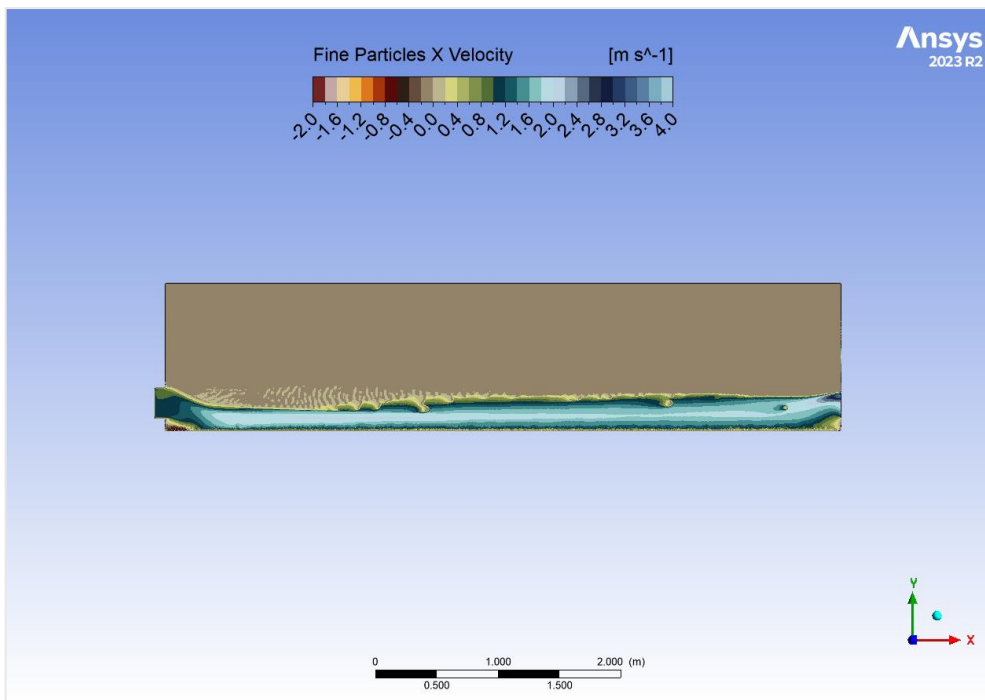


Figure 4-21. Fine particles velocity (X direction) contour plot. Bimodal flow. Inclination: 0.5°, inlet velocity: 1 [m/s].



## B. Scenario 2

Based on the information presented in Table 4-2, Scenario 2 maintained the same two-dimensional flume model with a  $0.5^\circ$  inclination and a mixture of water and particles entering the flow zone through the inlet structure. However, in this scenario, the mixture inlet velocity was increased to  $2 [m/s]$ , corresponding to a flow rate of  $0.5 [m^2/s]$ . The remaining simulation parameters remained identical to Scenario 1: a time step of 0.1 seconds with 20 iterations per time step, and a total of 1200 time-steps executed for a simulated flow duration of 2 minutes. As observed in Scenario 1, the flow achieved a state of relative stability within the first minute, exhibiting minimal instabilities thereafter. Consistent with Scenario 1, the final time step was chosen for further analysis to ensure a stable flow state.

Just like with Scenario 1, a density contour plot (Figure 4-22) is presented to visualize the overall distribution of phases within the system at the final time step. This plot utilizes the same weighted average calculation described in the previous section. As observed in Scenario 1, regions with higher density are concentrated near the flume bottom, indicating a greater presence of the solid phases in this zone. This behaviour aligns with the expectation that denser particles will preferentially migrate towards the bottom. However, due to the increased discharge in Scenario 2 ( $2 [m/s]$  compared to  $1 [m/s]$  in scenario 1), the overall flow depth appears higher in this case.

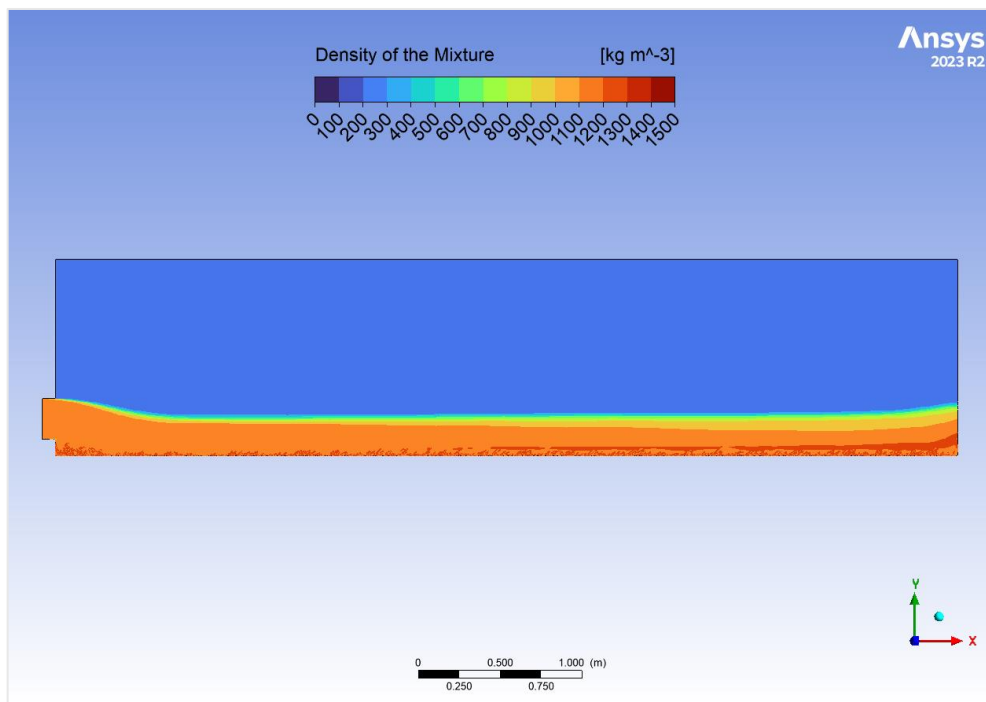


Figure 4-22. Density contour plot. Bimodal flow. Inclination:  $0.5^\circ$ , inlet velocity:  $2 [m/s]$ .

Figures 4-23, 4-24, and 4-25 present the volume fraction distribution across the previously analysed cross-sections (CS1, CS2, and CS3) for Scenario 2. Consistent with Scenario 1, the water surface location was identified based on the point where the volume fractions of water and air become equal [8].

In CS1, the water surface is estimated to be situated at  $0.26 [m]$  above the flume bottom, which is considerably higher compared to scenario 1 ( $0.142 [m]$ ). This difference can be attributed to the increased discharge in Scenario 2. Similarly, the water surface in CS2 and CS3 is estimated to be  $0.244 [m]$  and  $0.251 [m]$  above the bottom, respectively. CS3 exhibits a slightly higher water depth compared to CS2 and this aligns with the curvature observed in the density



contour plot (Figure 4-22) for Scenario 2, suggesting a potential influence of the step structure located upstream of the outlet on the flow profile in this region.

Similar to Scenario 1, the volume fractions of the solid phases in Scenario 2 reveal minimal signs of accumulation at the flume bottom across all three cross-sections. Non-zero velocities for both solid phases are observed along the flume, indicating minimal settling behaviour.

As expected, CS1 displays minimal stratification of the solid phases, reflecting the homogenous mixture entering the flume at this location. However, CS2 and CS3 exhibit a stratification pattern, with coarser particles concentrated closer to the bottom compared to the finer ones. This observation suggests a segregation process occurring as the flow progresses downstream, consistent with Scenario 1. Also, a higher volume of water is observed flowing above the solid phases across all three cross-sections.

The first 4 [cm] above the flume bottom exhibit significant fluctuations in the volume fractions of both particles and water. This phenomenon can be attributed again to the complex interactions occurring in this region, including wall shear stresses acting between the particles themselves, the particles with the flume wall, and the particles with the water. The increased distance of the fluctuation zone from the bottom (compared to 2 [cm] in Scenario 1) can be attributed to the higher discharge.

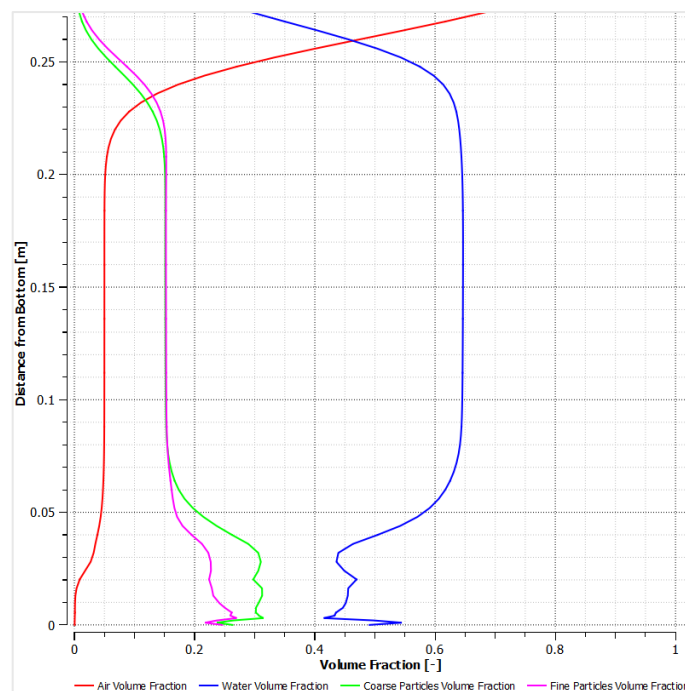


Figure 4-23. Volume fraction of air, water, coarse particles, and fine particles over CS1. Bimodal flow. Inclination: 0.5°, inlet velocity: 2 [m/s].

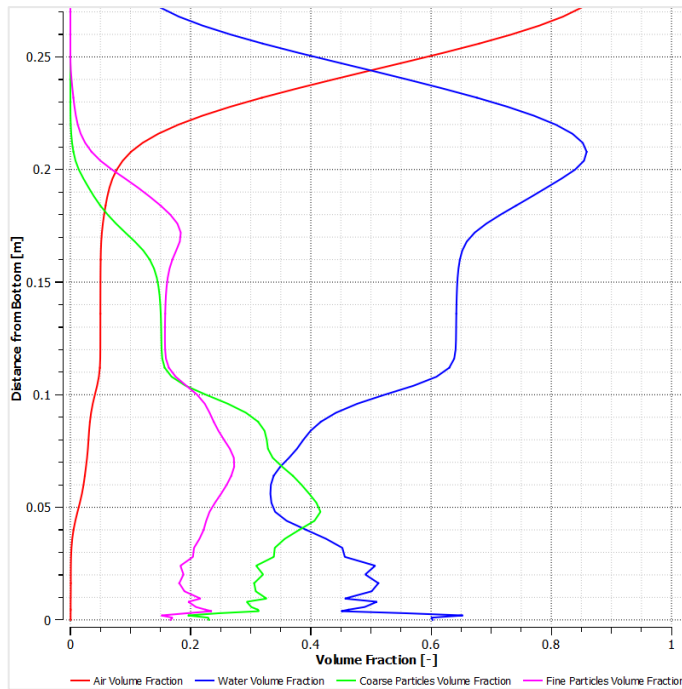


Figure 4-24. Volume fraction of air, water, coarse particles, and fine particles over CS2. Bimodal flow. Inclination:  $0.5^\circ$ , inlet velocity: 2 [m/s].

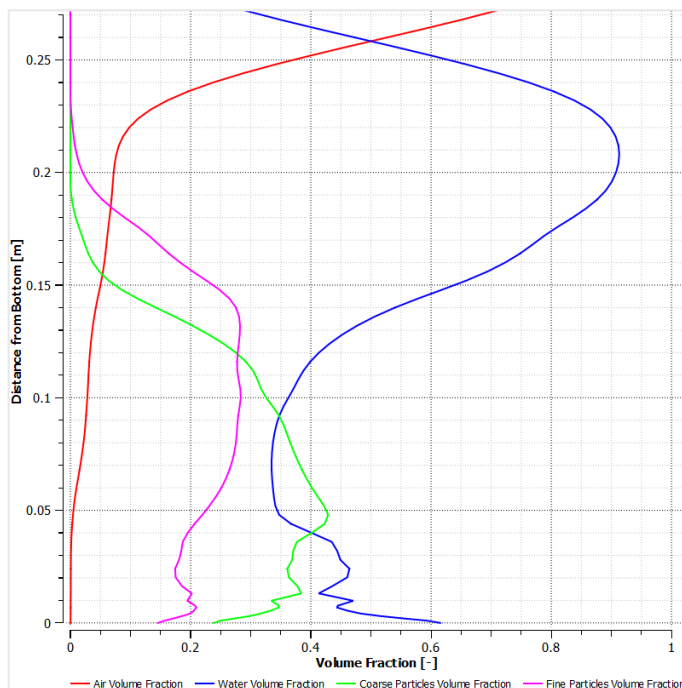


Figure 4-25. Volume fraction of air, water, coarse particles, and fine particles over CS3. Bimodal flow. Inclination:  $0.5^\circ$ , inlet velocity: 2 [m/s].

Figures 4-26, 4-27, and 4-28 present the horizontal ("X") velocity profiles of the water and solid phases across cross-sections CS1, CS2, and CS3, respectively, for Scenario 2. Similar to Scenario 1, the vertical ("Y") velocities are observed to be minimal and are considered to have a negligible impact on the overall flow behaviour. As expected, the velocity distribution in CS1 exhibits a relatively uniform profile. Since this location is closest to the inlet, the flow has not yet undergone significant development, resulting in a consistent velocity distribution across the channel depth.

The velocity profiles in CS2 display distinct differences compared to Scenario 1. In the upper quarter of the flow, both coarse and fine particles show a dramatic reduction in velocity close to the water surface. This observation aligns with the volume fraction plot presented, where minimal particle presence is found in this region. Right below the dramatic velocity reduction zone, both solid phases exhibit a slightly higher velocity compared to the water. This behaviour might be a result of numerical inaccuracies associated with the solver method.

The three phases (water, coarse particles, fine particles) in CS2 exhibit a more coupled velocity profile compared to Scenario 1, which suggests that the higher discharge affects the stratification. The less intense velocity fluctuations at the bottom compared to Scenario 1 further support this observation, since with a higher flow velocity, particles are less likely to settle and interact with the bed, leading to a smoother velocity profile in this region.

Similar to CS2, the velocity profiles in CS3 reveal a more coupled behaviour between the water and solid phases compared to scenario 1. Exceptions are observed near the water surface, where minimal particle presence leads to lower particle velocities, and near the bottom, where some fluctuations persist. However, the overall reduction in stratification due to the increased discharge in scenario 2 is evident in CS3 as well.

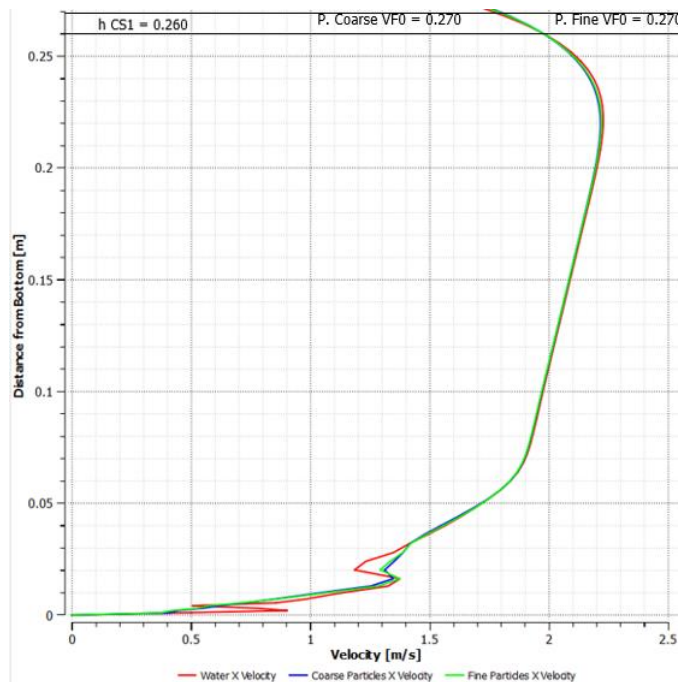


Figure 4-26. Velocities of water, coarse particles, and fine particles over CS1. Bimodal flow. Inclination: 0.5°, inlet velocity: 2 [m/s].

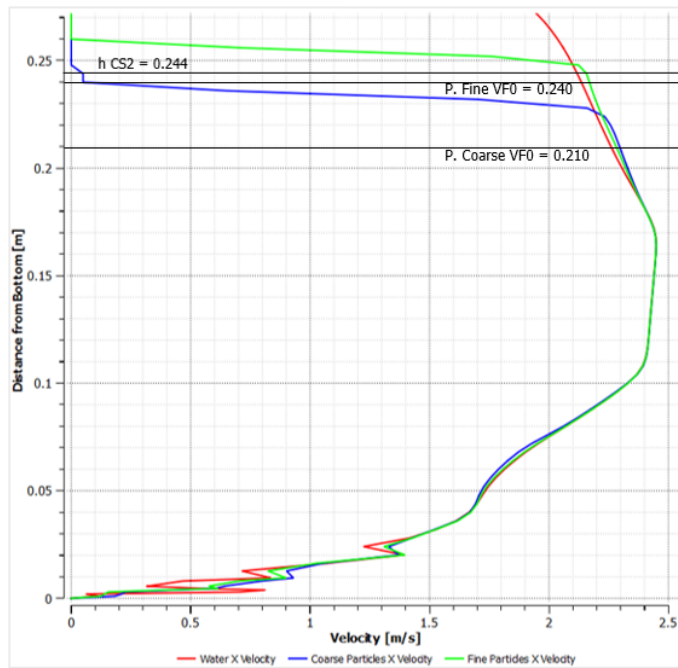


Figure 4-27. Velocities of water, coarse particles, and fine particles over CS2. Bimodal flow. Inclination:  $0.5^\circ$ , inlet velocity: 2 [m/s].

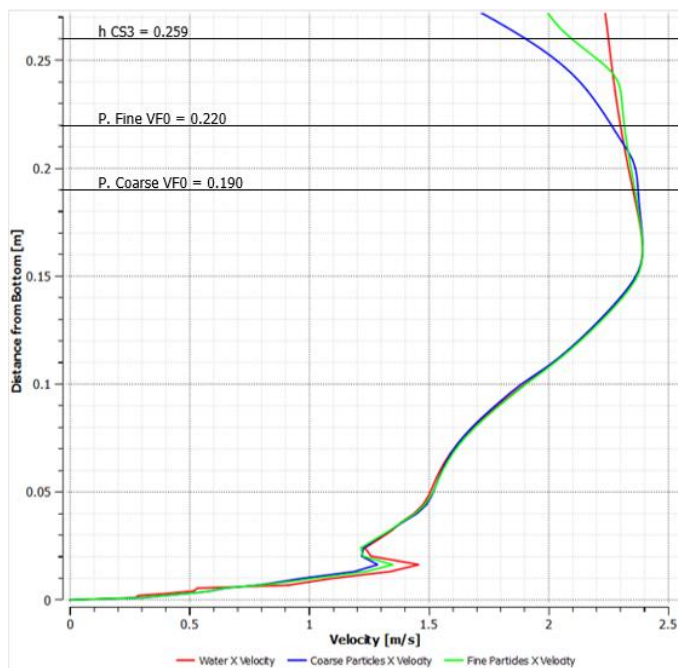


Figure 4-28. Velocities of water, coarse particles, and fine particles over CS3. Bimodal flow. Inclination:  $0.5^\circ$ , inlet velocity: 2 [m/s].

Continuing the analysis for Scenario 2, Figures 4-29 and 4-30 present horizontal velocity contour plots for the coarse and fine particle phases, respectively. As observed in the figures, the water-solids mixture exhibits generally higher and more uniform velocities throughout the flume compared to scenario 1. Notably, in the first third of the flume, velocities appear higher due to the increased inlet velocity in Scenario 2. This velocity stabilizes as it approaches the mid-section and remains relatively constant until reaching the outlet zone, where a small increase shows a velocity increase for both coarse and fine particles due to the evacuation through the atmospheric pressure boundary condition at the outlet.

However, a noteworthy discrepancy is observed in the velocity plots. Both figures show non-zero velocities for the coarse and fine particles in some areas above the water surface. This observation contradicts the density plot (Figure X-W), which suggests no presence of particles in any region above the water-air interphase. Additionally, it is considered physically unrealistic for particles to escape the water and flow independently in the air. Therefore, these non-zero velocities above the water surface are likely attributable to miscalculations by the numerical solver employed in the simulation.

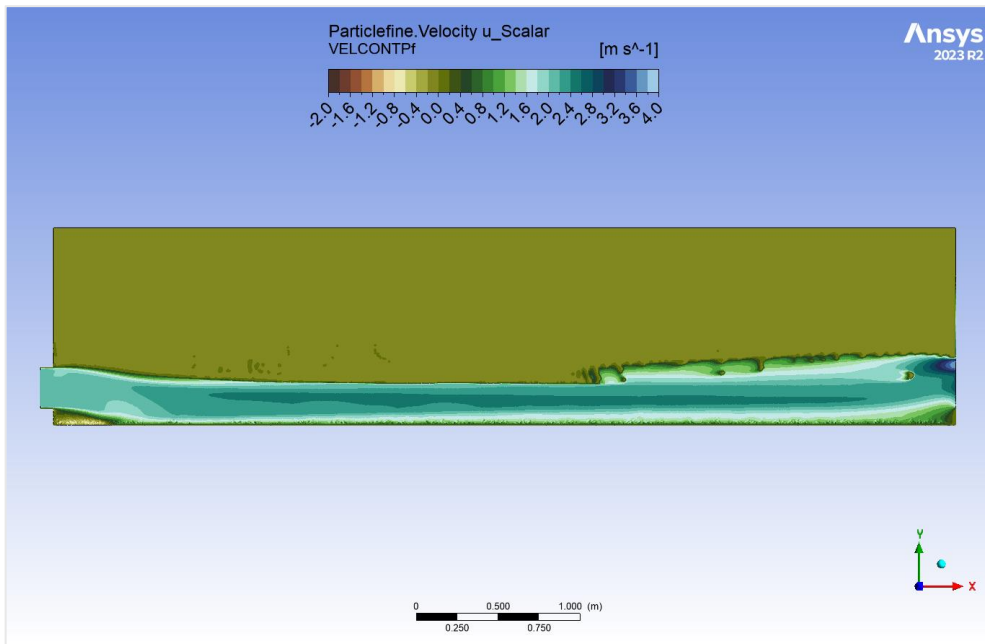


Figure 4-29. Coarse particles velocity (X direction) contour plot. Bimodal flow. Inclination: 0.5°, inlet velocity: 2 [m/s].

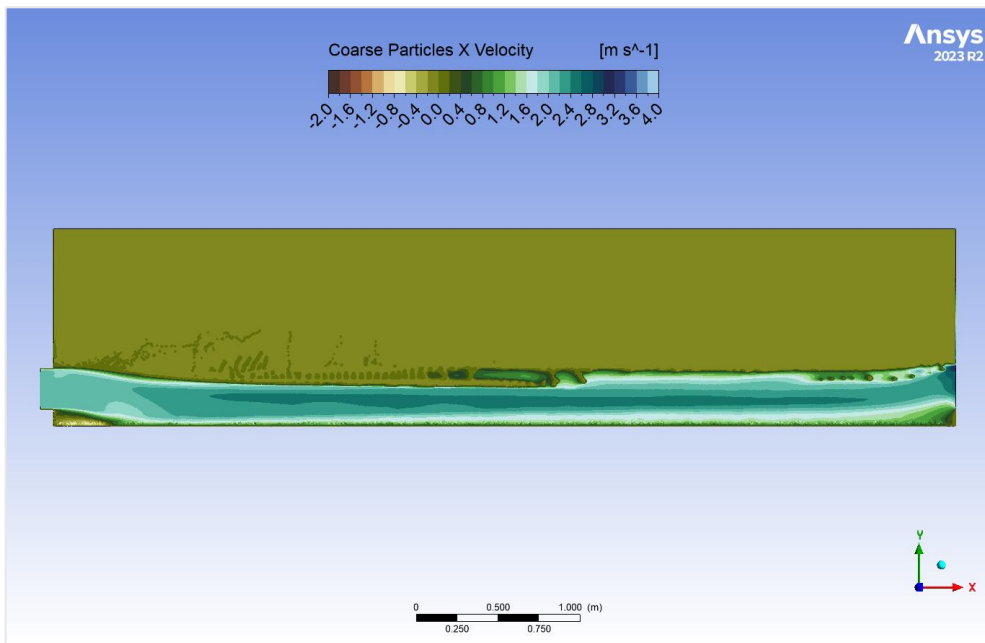


Figure 4-30. Fine particles velocity (X direction) contour plot. Bimodal flow. Inclination: 0.5°, inlet velocity: 2 [m/s].

### C. Scenario 3

Scenario 3 of the bimodal flow simulations utilizes an inlet velocity comparable to Scenario 1 but with a new flume inclination of  $1^\circ$ . The resulting density contour plot (Figure 4-31) exhibits a high degree of similarity to Scenario 1, suggesting that the change in inclination has a limited influence in the overall shape of the flow. However, a key difference lies in the reduced presence of high-density artifacts near the bottom compared to Scenario 1. This preliminary observation suggests a potentially more uniform distribution of the solid phases across the flume depth.

Similar to Scenarios 1 and 2, the density plot reveals curvature at both the beginning and end of the flume due to the presence of the inlet and outlet structures, respectively. As expected, the overall flow depth distribution in Scenario 3 appears lower compared to Scenario 2. This can be attributed to the combined effect of the lower discharge rate and the higher flume inclination in Scenario 3. The lower discharge rate leads to a reduced amount of material entering the flume, while the steeper inclination promotes faster flow velocities and potentially less settling of the solid phases.

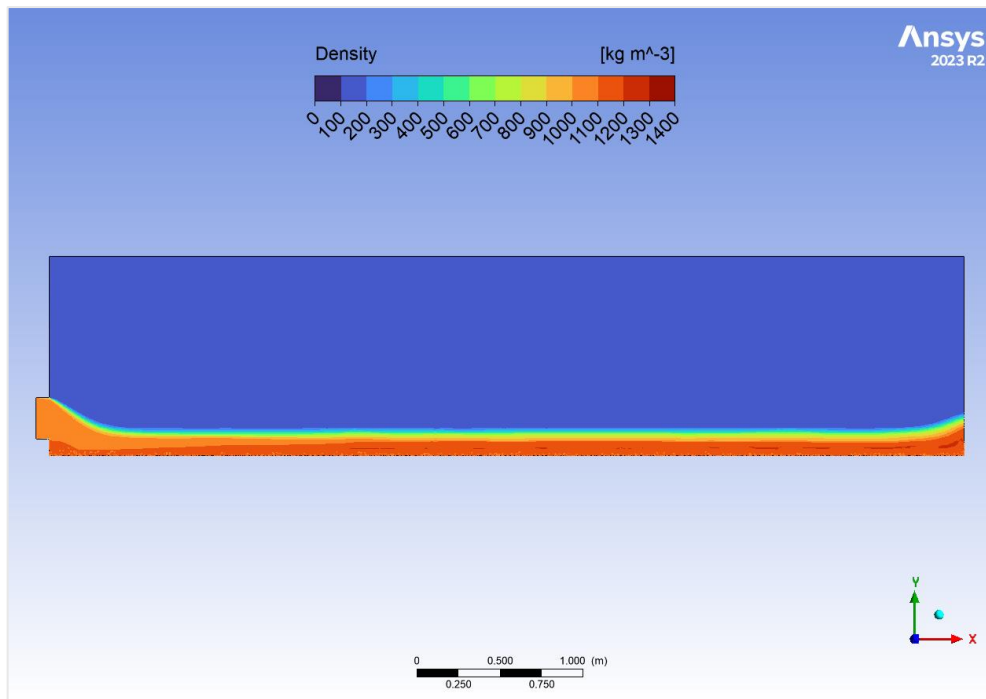


Figure 4-31. Density contour plot. Bimodal flow. Inclination:  $1^\circ$ , inlet velocity: 1 [m/s].

Similar to the previous scenarios, the water surface location was estimated at the point where water and air volume fractions become equal [8]. This case resulted in water surface depths of 0.145 [m], 0.143 [m], and 0.143 [m] above the flume bottom for CS1, CS2, and CS3, respectively. The slight decrease in water surface depth from CS1 to CS2 and CS3 aligns with expectations since the curvature at the inlet slightly influences the water surface at CS1.

Compared to all previous scenarios, including the unimodal flow, CS1 in Scenario 3 exhibits early signs of particle settling and stratification. Here, we observe a higher concentration of coarser particles below 5.5 [cm] from the bottom, while finer particles have a slightly higher presence above this mark. This initial stratification indicates a separation process beginning even at the initial stages of the flow.

Moving downstream to CS2, the stratification becomes more evident. This cross-section displays a dramatic increase in water presence in the upper third compared to CS1. Below this

zone, we observe a marked increase in the volume fraction of fine particles between 6 [cm] and 9 [cm] from the bottom compared to the coarse particles. Consequently, the coarse particles show a higher presence closer to the bottom. Notably, the region below 2 [cm] exhibits relatively intense fluctuations in the volume fractions of all three phases.

The flow behaviour at CS3, located further downstream, further follows the trend of stratification observed in CS2. The presence of a distinct water layer in the upper half and a clear separation between the fine and coarse particle concentrations below it suggest a more developed and stable flow regime compared to CS1 and CS2. Interestingly, the fluctuations in volume fractions near the bottom are less pronounced at CS3, potentially indicating a more established flow pattern due to its downstream location.

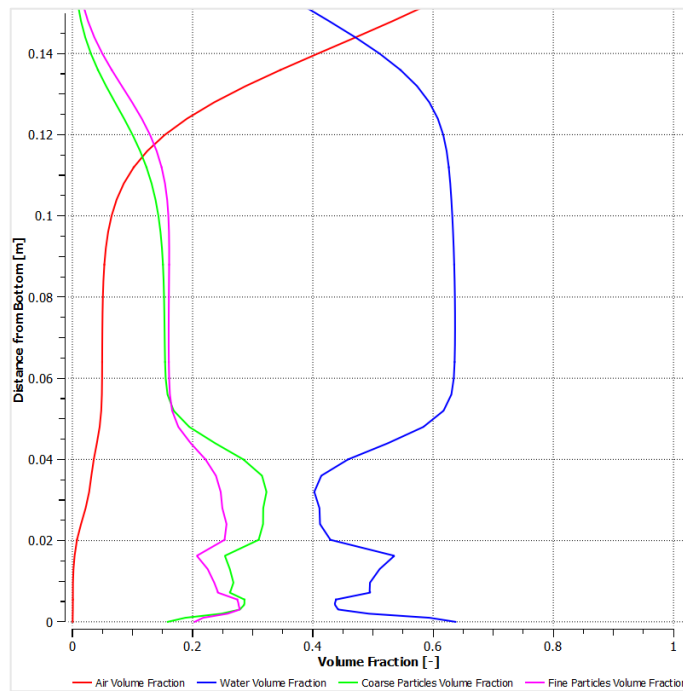


Figure 4-32. Volume fraction of air, water, coarse particles, and fine particles over CS1. Bimodal flow. Inclination: 1°, inlet velocity: 1 [m/s].

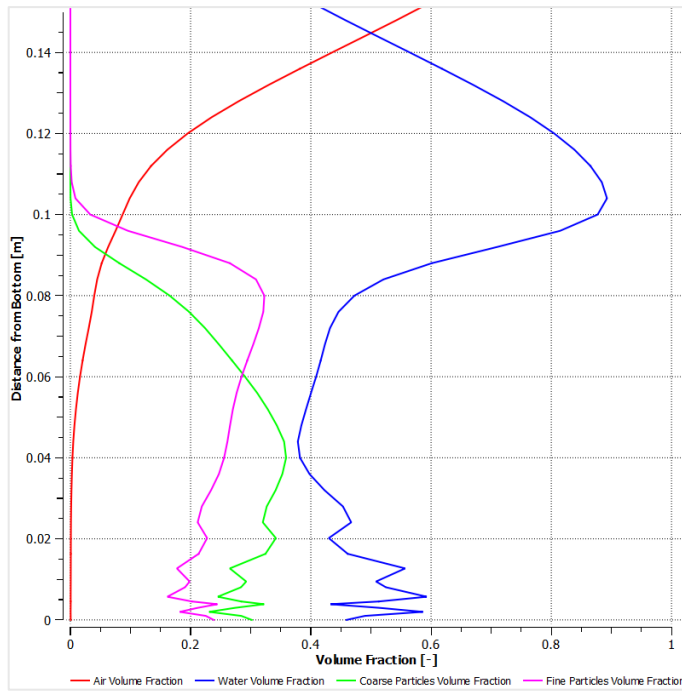


Figure 4-33. Volume fraction of air, water, coarse particles, and fine particles over CS2. Bimodal flow. Inclination: 1°, inlet velocity: 1 [m/s].

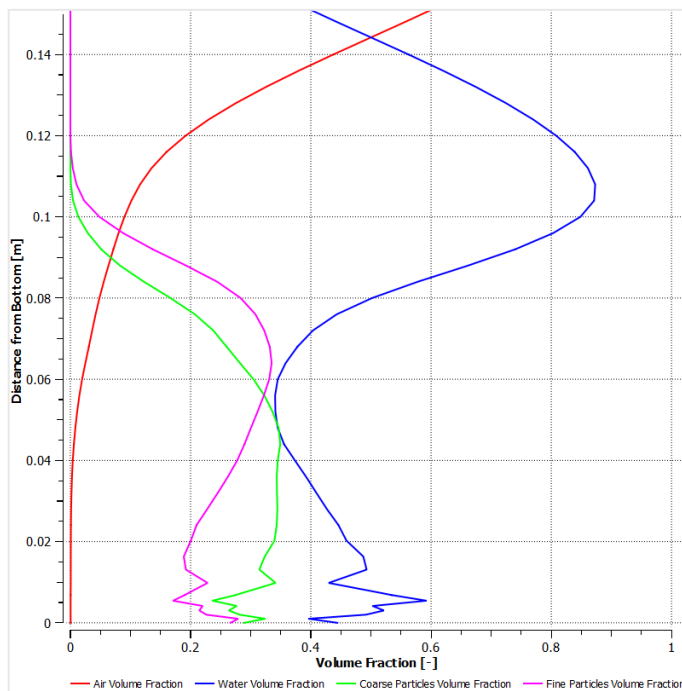


Figure 4-34. Volume fraction of air, water, coarse particles, and fine particles over CS3. Bimodal flow. Inclination: 1°, inlet velocity: 1 [m/s].



The velocity distribution plots across CS1, CS2, and CS3 in Scenario 3 reveal a significant difference compared to Scenario 1, which is the most important point of comparison in this case. The most notable feature is the high degree of coupling between the water and particle velocities across all three cross-sections (CS1, CS2, and CS3). This contrasts with Scenario 1, where the water and particle velocities exhibited a more differentiable behaviour. Another notable observation is the disappearance of the fluctuations when moving downstream in the cross sections, which represents the opposite behaviour compared to Scenario 1, where they become more intense when analysing further downstream. These fluctuations, often seen in Scenario 1 and attributed to complex near-wall interactions, are noticeably less present in Scenario 3.

The aforementioned behaviour suggests that the higher slope promotes a more stable flow regime near the bottom, but it's important to consider two facts. First, it can be mentioned that at lower slopes, particle interactions might play a more significant role in the near-bottom fluctuations. The steeper slope in Scenario 3 could potentially reduce the relative importance of these interactions, leading to a smoother, more coupled velocity distribution. Second, it must be noted that while the reduced fluctuations might be a positive sign, it's important to consider potential limitations of the model. The disappearance of fluctuations could also indicate a smoothing effect within the model itself and may not entirely reflect the true physical behaviour.

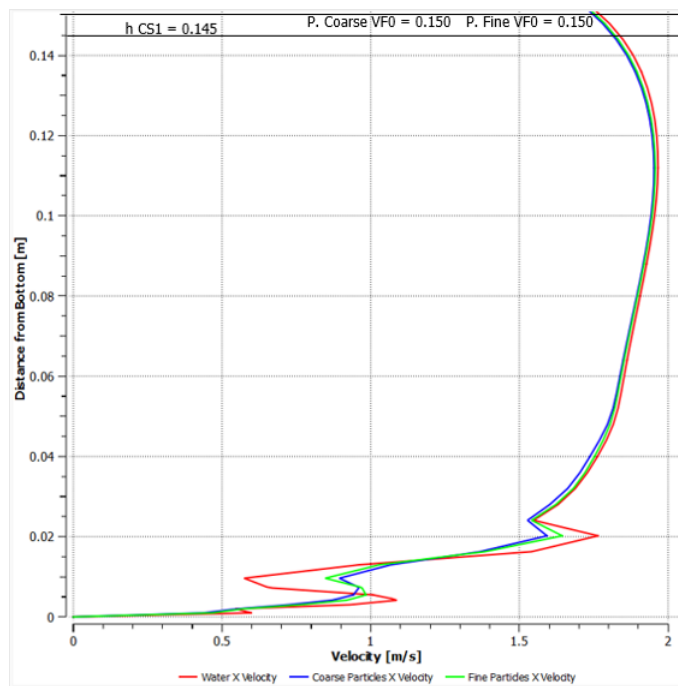


Figure 4-35. Velocities of water, coarse particles, and fine particles over CS1. Bimodal flow. Inclination: 1°, inlet velocity: 1 [m/s].

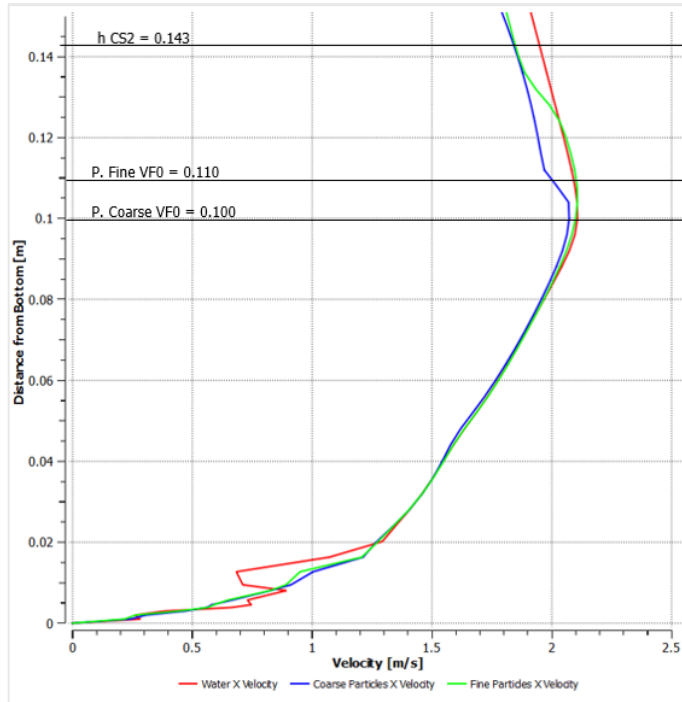


Figure 4-36. Velocities of water, coarse particles, and fine particles over CS. Bimodal flow. Inclination:  $1^\circ$ , inlet velocity: 1 [m/s].

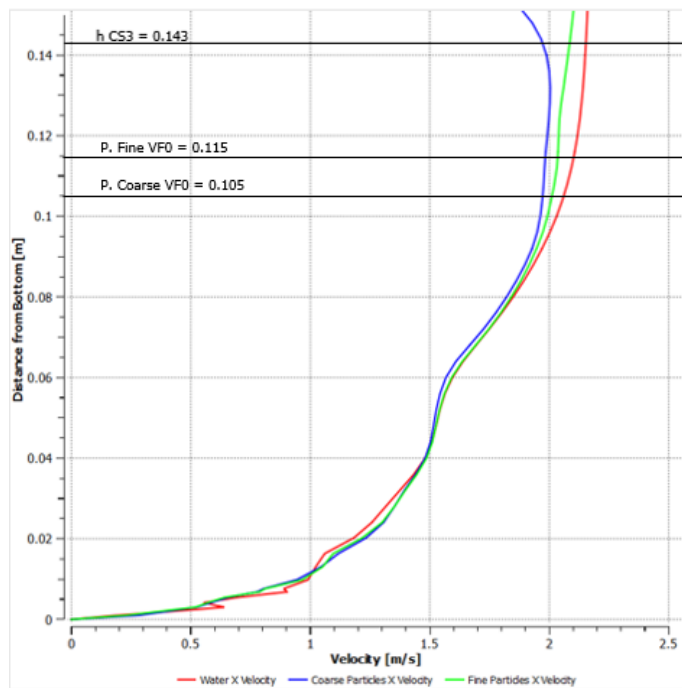


Figure 4-37. Velocities of water, coarse particles, and fine particles over CS3. Bimodal flow. Inclination:  $1^\circ$ , inlet velocity: 1 [m/s].

Continuing the analysis of Scenario 3, we now examine the velocity contour plots for both the coarse and fine particles (Figures 4-38 and 4-39). These plots offer a broader view of the velocity distribution compared to the detailed profiles analysed at CS1, CS2, and CS3. As observed in previous scenarios, the contour plots do exhibit some artifacts in the form of particle velocities appearing above the water surface. These artifacts can likely be attributed to miscalculations within the numerical solver and are not representative of real-world behaviour. However, the key takeaway from these plots lies in the overall colour distribution within the flow region. Compared to Scenario 1, the colour variations within the flow appear less pronounced in Scenario 3. This observation aligns well with the findings from the velocity profiles at specific cross-sections, which indicated a less stratified flow regime in Scenario 3 due to the steeper flume inclination.

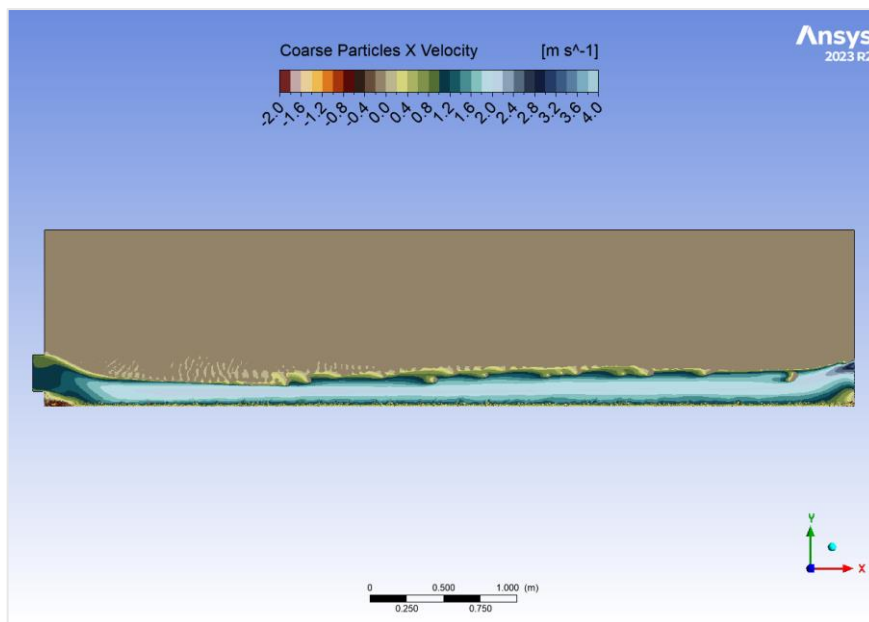


Figure 4-38. Coarse particles velocity (X direction) contour plot. Bimodal flow. Inclination:  $1^\circ$ , inlet velocity: 1 [m/s].

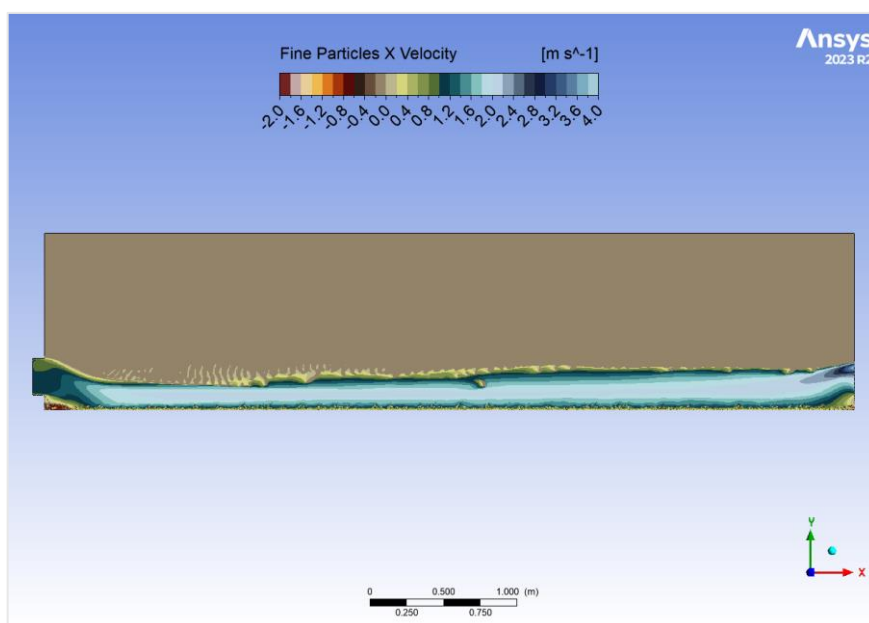


Figure 4-39. Fine particles velocity (X direction) contour plot. Bimodal flow. Inclination:  $1^\circ$ , inlet velocity: 1 [m/s].

#### D. Scenario 4

The analysis of Scenario 4, featuring a higher inlet mixture velocity of 2 [m/s] over a flume of 1 degree of inclination, translating into a discharge of 0.5 m<sup>2</sup>/s, begins with the examination of the density contour plot (Figure 4-40). This plot reveals several interesting observations regarding the distribution of the solid phases within the flume.

The initial portion of the flume bed exhibits a few spots with higher density, unlike previous scenarios where there's even what it was described as a possible swirling point. Compared to scenarios with lower inlet velocities, the development of stratification appears delayed in Scenario 4. A distinct separation between the solid and water phases doesn't become readily apparent until roughly the first half of the flume. This suggests that the increased water velocity due to the higher discharge might be hindering the initial settling of the particles, i.e. the flow has a higher flow development length.

Similar to other scenarios, the density plot reveals a clear layer of water occupying the upper portion of the flume after this first half. This distinct water layer becomes more prominent as the flow progresses downstream. As observed in previous scenarios, the density plot exhibits curvature at both the beginning and end of the flume, which reflects the presence of the inlet and outlet structures, respectively. In general, the flow also appears to have a higher flow depth, comparable to the one occurring in Scenario 2.

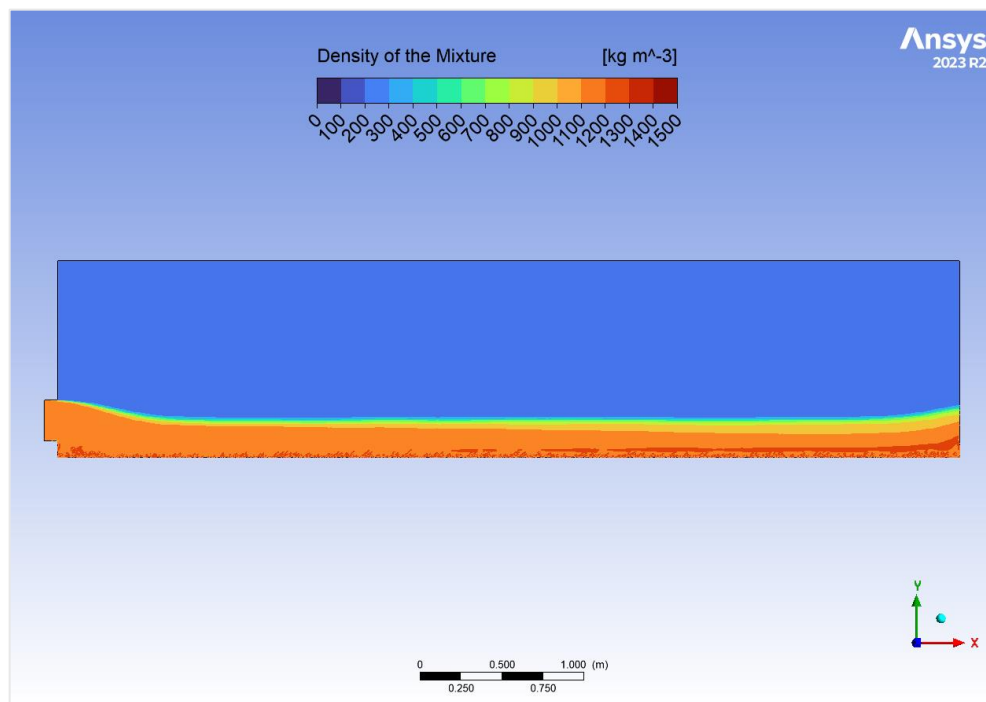


Figure 4-40. Density contour plot. Bimodal flow. Inclination: 1°, inlet velocity: 2 [m/s].

The analysis of volume fraction distribution in Scenario 4, characterized by a higher inlet velocity and discharge compared to Scenario 3, reveals interesting characteristics the flow behaviour. Here, we observe similarities to Scenario 2, but with some key distinctions.

At CS1, the closest section to the inlet, the estimated flow depth is 0.258 [m] from the bottom. Unlike previous scenarios with lower discharge, no clear stratification is observed at this stage. However, an early trend of particle accumulation near the bottom is already evident. Additionally, fluctuations in the volume fractions of both water and solid phases are present below 3 [cm] from the bottom. These fluctuations might be associated with the near-wall processes described before.

Moving downstream to CS2, the flow depth reduces to an estimated 0.230 [m]. Here, a clear pattern of stratification begins to emerge. This section exhibits coarse particles concentrated near the bottom, fine particles occupying the middle section, and a distinct water layer on top (which is also very evident in the density contour map). While fluctuations remain near the bottom, they are less intense compared to Scenario 1, 2 and 3.

At CS3, the furthest downstream section with an estimated flow depth of 0.239 [m], the stratification scheme resembles what was observed at CS2, however, the flow pattern at CS3 likely exhibits characteristics that may be associated to a better development of the flow due to its location. Similar to CS2, fluctuations near the bottom are present with comparable intensity.

The trend of higher flow depths at CS1 and CS3 compared to CS2 is consistent with Scenario 2, but not to Scenario 1 and 3. This variation can be attributed to the presence of the inlet and outlet structures, respectively, which suggest that these are more influential at higher discharges.

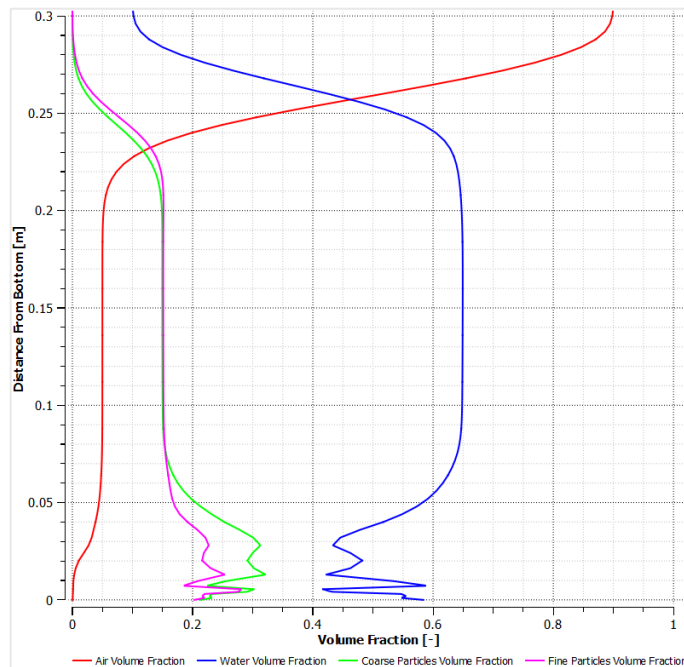


Figure 4-41. Volume fraction of air, water, coarse particles, and fine particles over CS1. Bimodal flow. Inclination: 1°, inlet velocity: 2 [m/s].

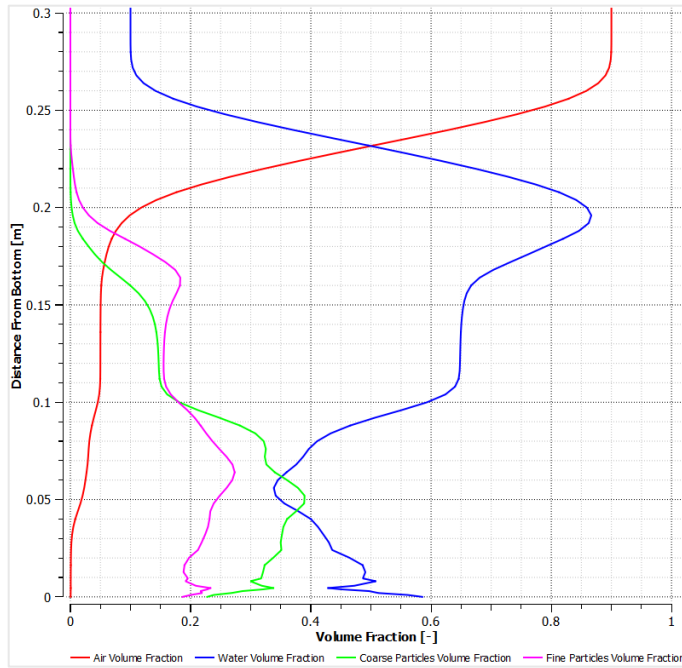


Figure 4-42. Volume fraction of air, water, coarse particles, and fine particles over CS2. Bimodal flow. Inclination: 1°, inlet velocity: 2 [m/s].

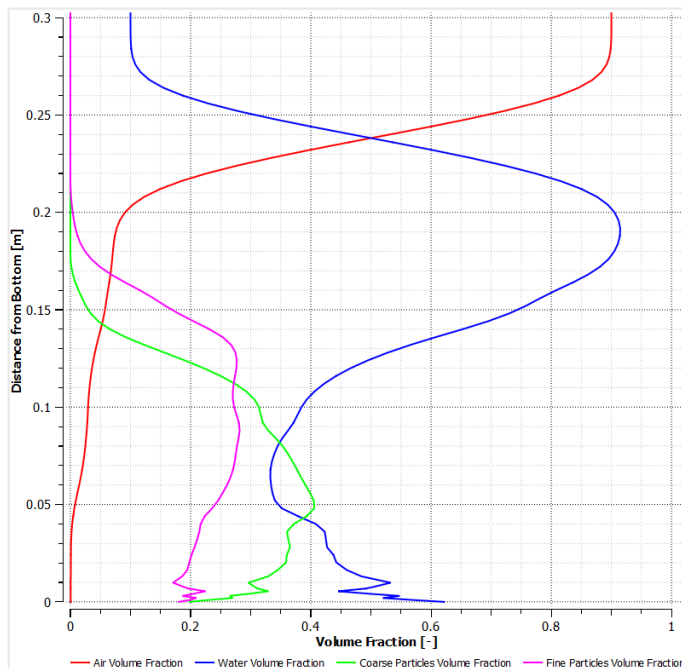


Figure 4-43. Volume fraction of air, water, coarse particles, and fine particles over CS3. Bimodal flow. Inclination: 1°, inlet velocity: 2 [m/s].

Moving to the velocity profile plots, some key information can be extracted. At CS1, the closest section to the inlet, the velocity profiles for all three phases (water, coarse particles, and fine particles) exhibit a high degree of coupling. This is expected during the initial stages of the flow, as the combined mixture is just entering the flume and the solid particles haven't had sufficient time and/or space to separate significantly from the water. The near-bottom fluctuations in velocity are also less pronounced compared to other scenarios, resembling the distribution observed in Scenario 2, but with even lower intensity. The reasons for this reduced fluctuation were discussed earlier (potentially related to the higher water velocity due to increased discharge).

Moving downstream to CS2, a significant decrease in the coarse particle velocity near the water surface becomes evident. This aligns well with the volume fraction plot at CS2, which showed a consistent reduction for coarse particles in the same zone. The fine particles also exhibit a dramatic reduction in velocity but reaching zero above the estimated location of the water surface. This behaviour is physically unrealistic and can be attributed to numerical limitations of the computational software used for the simulations, as it was mentioned in previous cases. The remaining portion of the velocity profile indicates a coupled behaviour for all three phases (water and coarse/fine particles) except for a single instability observed in the water velocity profile near the bottom.

At the furthest downstream cross section (CS3), the velocities of coarse particles again show a sharp reduction near the water surface, mirroring the observations at CS2. The fine particle velocities exhibit a similar trend but with a slight delay, even closer to the surface. This behaviour aligns perfectly with the volume fraction profiles at CS3, where the decrease of presence of particles occurs in the vicinity of the water surface. The remaining portion of the velocity profile suggests strong coupling between all phases, likely due to the combined effects of higher discharge and steeper flume inclination. However, a minor instability is still present in the water velocity profile near the bottom.

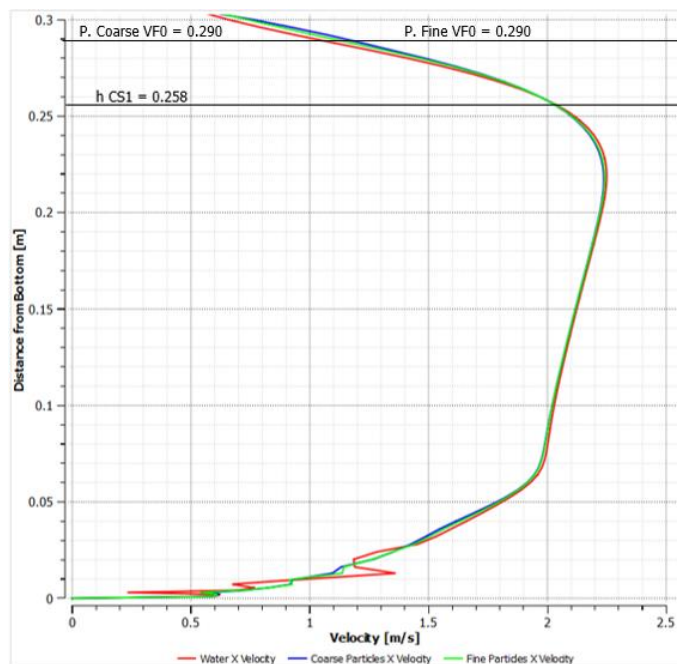


Figure 4-44. Velocities of water, coarse particles, and fine particles over CS1. Bimodal flow. Inclination:  $1^\circ$ , inlet velocity: 2 [m/s].

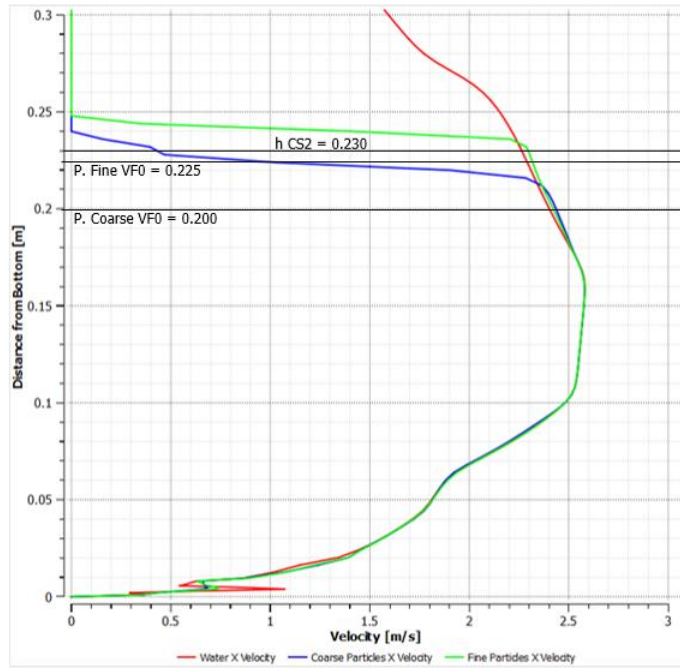


Figure 4-45. Velocities of water, coarse particles, and fine particles over CS2. Bimodal flow. Inclination: 1°, inlet velocity: 2 [m/s].

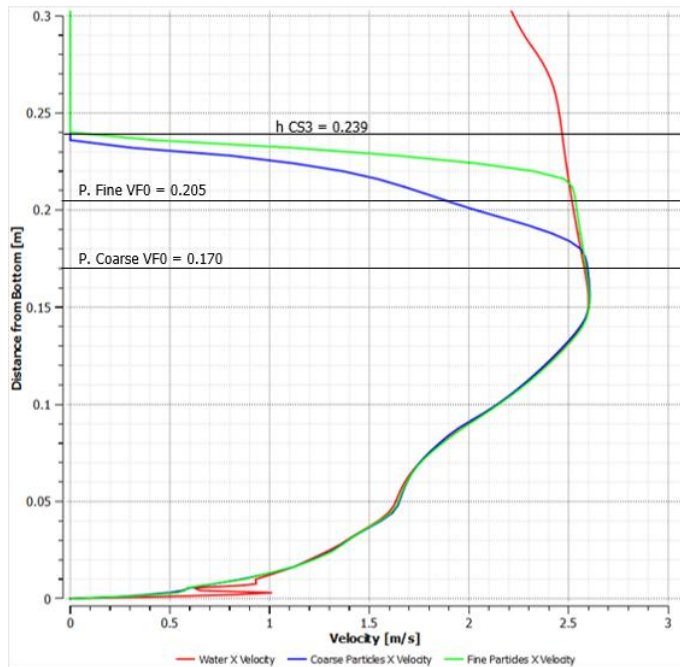


Figure 4-46. Velocities of water, coarse particles, and fine particles over CS3. Bimodal flow. Inclination: 1°, inlet velocity: 2 [m/s].



The velocity contour plots for both coarse and fine particles (Figures 4-47 and 4-48) reveal some key characteristics of the flow behaviour in Scenario 4. A particularly noteworthy feature is the zone immediately following the step created by the inlet structure. Similar to previous scenarios, this region exhibits negative velocities, suggesting the presence of a localized swirling phenomenon. However, the zone appears more extended compared to scenarios with lower inlet velocities, which can be attributed to the combined effects of the higher mixture velocity entering the flume and the steeper overall inclination. This extended swirling zone might contribute to a longer curvature of the water surface in the vicinity of the inlet, potentially explaining the higher water surface location observed at CS1 in this scenario (an effect also seen in Scenario 2).

Regarding the general velocity behaviour, the contours show a trend of acceleration along the flume length. This acceleration is likely a consequence of the steeper inclination, which promotes an increase in water velocity as the flow progresses downstream until it reaches a certain stability. This increase in water velocity also influences the perceived flow depth, which exhibits a continuous decrease until it is eventually affected by the presence of the outlet structure. Based on these observations, it's reasonable to assume that the flow in Scenario 4 requires a greater flume length to fully develop a stable and steady state.

As in previous scenarios, some artifacts appear in the form of particle velocities registered above the water surface. These can be attributed to limitations within the numerical solver and are not representative of physically realistic behaviour. Despite these limitations, the contours do provide a general indication of stratification, which aligns with the observations from the velocity profile plots.

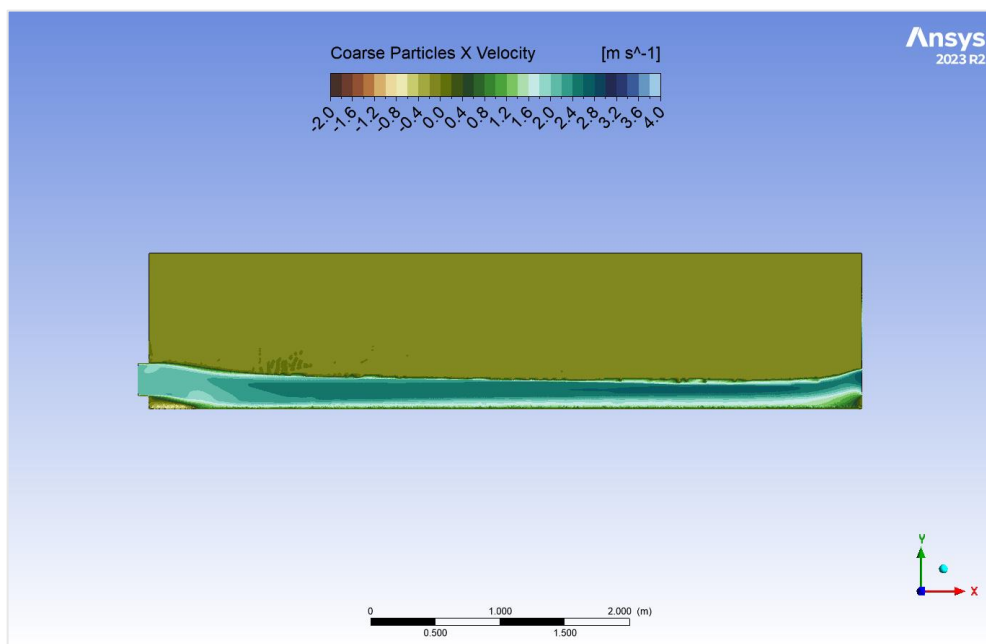


Figure 4-47. Coarse particles velocity (X direction) contour plot. Bimodal flow. Inclination:  $1^\circ$ , inlet velocity:  $2[m/s]$ .

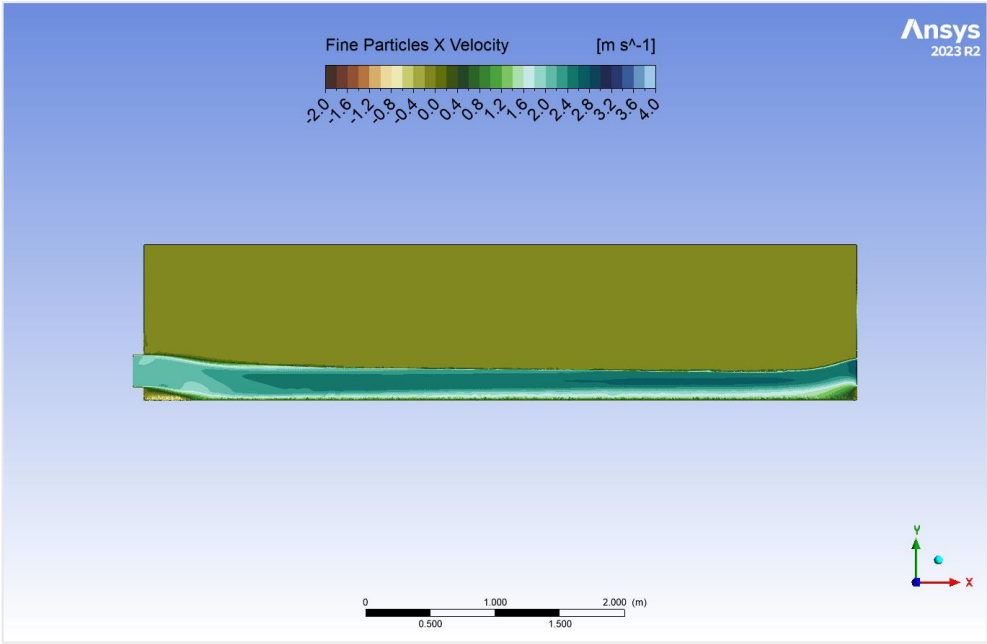


Figure 4-48. Fine particles velocity (X direction) contour plot. Bimodal flow. Inclination:  $1^\circ$ , inlet velocity:  $2[\text{m/s}]$ .

## 5. Conclusions

---

The main focus of this thesis was to assess the Eulerian-Eulerian multiphase model through Ansys Fluent simulations for understanding particle transport dynamics in open channel flows. The thesis compares different flow scenarios, examining how variations in particle size distribution—specifically unimodal versus bimodal distributions—affect flow behaviour and the transport mechanisms of particles. For these purposes, several steps were conducted, and different conclusions can be extracted.

To begin, the water-only simulation served as a foundational step in understanding the basic flow dynamics within the flume before introducing complexities such as solid particles. This initial stage used a water-air system to observe how water behaves under simplified conditions. Some key findings and conclusions can be extracted from this scenario.

Firstly, the simulation revealed two main curvatures in the water surface within the flume. These curvatures reflect adjustments in flow due to changes in the flume's geometry at the inlet and near the step structure at the outlet. The development of the flow was visually captured and quantified, showing a gradual transition to a fully developed state by the third cross-section (CS3). This flow shape is considered to be physically reasonable, as this kind of obstacles usually tend to generate curvatures in the water surface [26]. Secondly, the third cross-section shows that the flow reached a supercritical state, indicating minimal influence from downstream conditions. Thirdly, the comparison of the simulation results with empirical calculations (Manning's equation), shows that the simulation achieved a reasonable accuracy, with a percentual error around 6.23% for the estimated water depth at CS3. These conclusions not only validate the use of the SST  $k-\omega$  turbulence model in capturing the essential characteristics of the flow but also establish a solid groundwork for introducing complexities like unimodal and bimodal flows in future simulations.

Subsequently, the unimodal simulation was the next step to test the model before the executions of a bimodal configuration. Here some key observations led to the following conclusions.

Firstly, the simulation identified higher particle concentrations near the flume bottom, reflecting the settling of a solid granular phase in an open channel flow. The density contour plots highlighted a separation between a layer where water had higher presence (upper part), and a layer where particles had a higher volume fraction (lower part), with a noticeable density gradient from bottom to top. Secondly, the water surface elevations increased from the first to the third cross section, indicating a progressive deepening of the water layer as the flow developed downstream. This suggests that, under these flow conditions, the flow probably needed a longer flume to develop completely, statement that can't be empirically corroborated with the development length equation (Equation 2-79) due to the solid phase presence. Thirdly, the initial section (CS1) near the inlet showed less developed flow characteristics with a more homogeneously mixed state of particles and water. Moving downstream, the simulation revealed a clearer stratification, where particles settled closer to the bottom, and water dominated the upper half of the flume. This stratification became more pronounced by CS3, reflecting a transition towards a steadier condition. This observation was considered as the first finding related to the existence of stratification processes in this kind of granular flows, as it is observed in laboratory exercises [28]. Finally, it's worth mentioning that some discrepancies were noted in the velocity profiles at CS3, particularly the presence of non-zero particle velocities where particles were absent, indicate possible numerical limitations or errors in the CFD solver. These need careful consideration, as they could impact the accuracy of predictions about flow behaviour, especially in transition zones where particle concentrations are changing rapidly.

The stable flow regime, at least over time, and the observed stratification provide a reliable baseline for introducing additional complexities, such as bimodal particle distributions. Watching the behaviour of a unimodal flow helped in understanding the interactions and potential segregation effects that arose when two distinct particle sizes were introduced.

Regarding the bimodal simulations, several key findings were identified. Firstly, it's noteworthy that across all four scenarios, the bimodal simulations show at least some degree of stratification, usually following the same trend: Finer particles tending to hover above the coarser particles, that were always closer to the flume bed. This segregation indicates differential settling velocities and interactions between particle sizes, influencing the overall particle transport dynamics. Secondly, the volume fraction plots, and the density contour plots highlighted the bottom zones of the flume as where solid particles are more concentrated, which complemented with the velocity plots outcomes, allowed to conclude that there was scarce proof to assume that accumulation was happening, but enough to highlight the still relevant particle-particle and the particle-wall interactions even when a continuous flow occurs. The density contour plots underscore these observations, with denser regions near the bottom gradually transitioning to less dense, water-dominated regions towards the top. This gradual transition is more pronounced in scenarios with lower velocities, where particle settling is more evident. The influence of the slope is closely related to this since it affects the velocity at which the flow circulates. Noteworthy was the case of Scenario 4, which was the one with the highest discharge and slope. Here, the stratification process took place only in the second half of the flume, highlighting the ability of higher velocity flow to impact the stratification of the phases. Thirdly, the velocity profiles indicate that water generally maintains a higher velocity compared to both coarse and fine particles. In early sections like CS1, particle velocities are closely aligned with water velocities due to the initial mixing at the inlet. As the flow develops (CS2 and CS3), particles show a decrease in velocity, especially near the water surface, reflecting the influence of gravitational settling and possibly inter-particle collisions and drag forces. It's noteworthy though, that this effect was less present with higher velocities of mixture insertion, and with higher values of inclination. Finally, the solver's ability to manage complex interactions in bimodal flows, while generally considered acceptable in the cases treated in this thesis, shows limitations in areas such as resolving the upper boundary of the particle-laden flow and capturing the detailed interactions near the flume bed. This can result in numerical artifacts such as non-zero velocities in zones where particles were not present.

The outcomes derived from these simulations of unimodal and bimodal flows can enhance the ability to predict and manage particle transport in environmental engineering. By accurately modelling how solids behave under different conditions, it is possible to better design waterways that minimize erosion and manage particles effectively, reducing the risk of flooding and extending the lifespan of vital infrastructure. This improved understanding also aids in protecting aquatic ecosystems by ensuring that nutrient-rich particles support ecological health without causing pollution or harm.

Moreover, as climate change alters water patterns, the insights gained from these detailed studies equip engineers and policymakers to adapt water management practices to meet future challenges. This research not only supports more sustainable development and maintenance of water resources but also helps in crafting policies that balance human needs with environmental protection.

## 6. Bibliography

---

- [1] F. R. Menter, "Review of the SST Turbulence Model Experience from an Industrial Perspective," 2009.
- [2] M. Larcher and J. T. Jenkins, "The Influence of Granular Segregation on Gravity-driven Particle-fluid flows," *Advances in Water Resources*, vol. 129, pp. 365-372, 2019.
- [3] M.-z. Li, Y.-p. He, R.-h. Jiang, J. Zhang and H.-s. Zhang, "Effects of Large Particles on the Transport Characteristics of Slurries in Horizontal Pipes," *Particulate Science and Technology*, pp. 532-543, 2022.
- [4] M. Z. Li, Y. P. He, Y. D. Liu and C. Huang, "Effect of Interaction of Particles with Different Sizes on Particle Kinetics in Multi-Sized Slurry Transport by Pipeline," *Powder Technology*, vol. 338, pp. 915-930, 2018.
- [5] C. T. Crowe, *Multiphase Flow Handbook*, Boca Raton: Taylor & Francis, 2006.
- [6] H. Im, J. Park and J. Lee, "Prediction of Main Regime Transition with Variations of Gas and Liquid Phases in a Bubble Column," *ACS Publications*, 2019.
- [7] S. Subramaniam, *Lagrangian-Eulerian Methods for Multiphase Flows*, 2012.
- [8] C. E. Brennen, *Fundamentals of Multiphase Flow*, Pasadena: Cambridge University Press, 2005.
- [9] ANSYS Inc., *Ansys Fluent Theory Guide*, Canonsburg, 2023.
- [10] G. H. Yeoh and J. B. Joshi, *Handbook of Multiphase Flow Science and Technology*, Singapore: Springer, 2023.
- [11] J. Duncan, "Introduction to Colloid and Surface Chemistry," 1992.
- [12] M. Berry, "The Molecular Mechanism of Surface Tension," 1971.
- [13] D. Gidaspow, "Multiphase Flow and Fluidization," Boston, 1994.
- [14] F. Moraga, R. Bonetto and R. Lahey, "Lateral Forces on Spheres in Turbulent Uniform Shear Flow," *International Journal of Multiphase Flow*, vol. 25, 1999.
- [15] O. Simonin and P. Viollet, "Predictions of an Oxygen Droplet Pulverization in a Compressible Subsonic Coflowing Hydrogen Flow," *ASME FEDSM*, 2001.
- [16] S. Chapman and T. Cowling, "The Mathematical Theory of Non-Uniform Gases," 1990.
- [17] D. Gidaspow, R. Bezburuah and J. Ding, "Hydrodynamics of Circulating Fluidized Beds, Kinetic Theory Approach," in *Proceedings of the 7th Engineering Foundation Conference on Fluidization*, 1992.
- [18] D. G. Schaeffer, "Instability in the Evolution Equations Describin Incompressible Granular Flow," 1987.

- [19] J. Ding and D. Gidaspow, A Bubbling Fluidization Model Using Kinetic Theory of Granular Flows, 1990.
- [20] D. Wilcox, "Reassessment of the scale determining equation for advanced turbulence models," 1988.
- [21] F. Menter, "Two-Equation Eddy-Viscosity Turbulence Models for Engineering Applications," 1994.
- [22] H. Versteeg and W. Malalasekera, "An Introduction to Computational Fluid Dynamics," 2007.
- [23] W. P. Jones and B. E. Launder, "The Prediction of Laminarization with a Two-Equation Model of Turbulence," *International Journal of Heat and Mass Transfer*, vol. 15, 1972.
- [24] J. H. Ferziger, M. Peric and R. Street, Computational Methods for Fluid Dynamics, Springer, 2020.
- [25] ANSYS Inc, Ansys Fluent User's Guide, 2023.
- [26] V. T. Chow, Open-Channel Hydraulics, McGraw-Hill, 1959.
- [27] V. Matoušek, V. Bareš, J. Krupička, T. Pícek and S. Zrostlík, "Experimental investigation of internal structure of open-channel flow with intense transport of sediment," *Journal Hydrology and Hydromechanics*, vol. 63, pp. 318-326, 2015.
- [28] V. Matoušek, V. Krupička, J. Pícek, T. Svoboda and S. Yrostlík., "Modelling of solids distribution in sediment laden open channel flow: laboratory validation.," in *IAHR World Congress*, Granada, 2022.
- [29] D. Drew and R. Lahey, "In Particulate Two-Phase Flow," 1993.
- [30] L. Schiller and A. Naumann, A Drag Coefficient Correlation, *Zeitschrift des Vereins Deutscher Ingenieure*, 1935.
- [31] P. Johnson and R. Jackson, ""Frictional-Collisional Constitutive Relations for Granular Materials, with Application to Plane Shear," *Journal Fluid Mech.*, 1987.
- [32] F. Menter and Y. Egorov., ""Re-visiting the Turbulent Scale Equation," 2004.
- [33] F. Menter and R. L. M. Kuntz, "Ten Years of Experience with the SST Turbulence Model," 2003.
- [34] G. Yadigaroglu and G. F. Hewitt, Introduction to Multiphase Flow, Zurich: Springer, 2018.
- [35] W. G. Gray, B. A. Schrefler and F. Pesavento, The solid phase stress tensor in porous media mechanics and the Hill–Mandel condition, 2009.
- [36] P. Li, S. J. Eckels, N. Zhang and G. W. Mann, "Effects of Parallel Processing on Large Eddy Simulations in ANSYS Fluent," in *ASME 2016 Fluids Engineering Division Summer Meeting collocated with the ASME 2016 Heat Transfer Summer Conference and the ASME 2016 14th International Conference on Nanochannels, Microchannels, and Minichannels*, 2016.

- [37] L. Svoboda, T. Pícek and V. Matoušek, "Camera-measured velocity distribution in laboratory open-channel flow with intense transport of bimodal combined-load," *Journal of Hydrology and Hydromechanics*, vol. 71, pp. 331-340, 2023.

## 7. Appendix A

---

### A. Specifications of the Computers

#### Computer 1 (Water-only simulation):

Processor: Intel Core i7-7700 3.6 GHz

RAM: 32 GB DDR4

Disk Type: SSD SATA-3

#### Computer 2 (Unimodal and Bimodal Simulations):

Processor: 2x Intel Xeon Gold 6132 in Scalable Mode 2.6GHz (Turbo: 3.7 GHz)

RAM: 128 GB DDR4

Disk Type: SSD SATA-3